

Doctoral Dissertation

Study of Antenna Design Techniques for
Use in Automotive Environment

By

Hideo Iizuka

June 2007

Under supervision of

Professor Nobuyoshi Kikuma

Department of Computer Science and Engineering,
Graduate School of Engineering,
Nagoya Institute of Technology

SYNOPSIS

There have been strong requirements of safety, comfortable time & space, and convenience for the mobility by vehicles. Several systems for these requirements have been gradually installed into vehicles with the growth of wireless technologies. Automotive antenna design technique is one of the key techniques to contribute the system realization very much. Automotive antennas generally need simple architectures and low cost due to consumer products, and compactness or low profile due to limited installation spaces of vehicle. Also, inclusion of the vehicle body into the antenna design is needed, when antenna performance is strongly affected by the vehicle body. This doctoral dissertation titled “Study of Antenna Design Techniques for Use in Automotive Environment” presents analytical, numerical, and experimental investigations of automotive antenna design techniques, particularly, in the highest and nearly the lowest edges of the frequency bands assigned for automotive wireless systems. The two frequency bands are the millimeter-wave and UHF bands. The investigations of the two frequency bands would provide useful design insights of automotive antennas in wide frequency range. Considering the impact on industry, the two systems that are installed practically and work effectively in 2000s are focused. Those are millimeter-wave radar system and digital terrestrial television (TV) reception system.

Millimeter-wave radar system needs antennas having higher efficiency, low cost, low profile, and so on. In this dissertation, a new configuration of microstrip antenna with inherently low cost and low profile is proposed to achieve higher efficiency. A fan beam subarray antenna and a pencil beam array antenna are designed for electrical and mechanical scanning radars, respectively. A new transition from waveguide to microstrip line is also proposed to connect the antennas on the surface of the radar sensor and circuit inside the sensor. The transition can be etched in the same process of antennas. The optimum design methodology for the transition leads a wider bandwidth, resulting in robustness for assembly

error. A transition working as a divider is also proposed.

Digital TV reception system adopts an adaptive array using four antennas based on the maximal ratio combining (MRC) method. In this dissertation, two types of antennas are proposed in the view point for an omnidirectional pattern synthesis in a horizontal plane and a thin structure for narrow installation spaces, respectively. A further bandwidth enhancement method for the thin structured antenna is also proposed, resulting in covering digital TV band when the antenna is installed on window glass or spoiler.

This doctoral dissertation is organized as follows. The scope of study is clarified with background in Chapter 1. Chapter 2 presents conventional techniques of antennas and associate circuits. A new microstrip antenna, new transition, and the optimum design methodology are described in Chapters 3, 4, and 5 for millimeter-wave radars. Digital TV antennas are described in Chapters 6, 7, and 8, which are H shaped antenna, stub-loaded dipole, and capacitor- and stub-loaded dipole. Chapter 9 presents some conclusions. This doctoral dissertation describes key technologies of novel automotive antennas for the two systems. I believe that the investigations in this dissertation contribute to the advancements for automotive antenna design techniques in both academic and industrial points of view.

CONTENTS

Chapter 1. Introduction

1.1 Background of study	1
1.2 Scope of study	2
1.3 Dissertation organization	3
References	5

Chapter 2. Conventional techniques

2.1 Introduction	6
2.2 Conventional millimeter-wave antennas	
2.2.1 Millimeter-wave radars and their antennas	6
2.2.2 Microstrip antennas	8
2.2.3 Feed networks	11
2.3. Conventional millimeter-wave transitions	13
2.4. Conventional digital TV antennas	
2.4.1 Digital TV reception system for vehicles	15
2.4.2 Radiation pattern of mounted antennas	17
2.4.3 Wideband methods	19
2.5 Conclusions	20
References	21

Chapter 3. Millimeter-wave microstrip antennas for automotive radars

3.1 Introduction	26
3.2 Proposal of microstrip antenna	26

3.3 Design of antennas including losses	
3.3.1 Coupling coefficient of radiating element	28
3.3.2 Feed line loss of linear array antenna	33
3.4 Developed antennas	
3.4.1 Fan beam subarray for electrical scanning radars	38
3.4.2 Pencil beam antenna for mechanical scanning radars	43
3.5 Conclusions	51
References	52
3.A Appendix	53

Chapter 4. Millimeter-wave transition from waveguide to microstrip line

4.1 Introduction	56
4.2 Proposal of microstrip line to waveguide transition	56
4.3 Fundamental performance of transition	
4.3.1 Impedance matching characteristics	61
4.3.2 Transmission characteristics	63
4.3.3 Bandwidth	65
4.3.4 Effects of errors in relative position	68
4.4 Conclusions	72
References	74
4.A Appendix	74

Chapter 5. Millimeter-wave transition from waveguide to two microstrip lines

5.1 Introduction	77
5.2 Proposal of transition from waveguide to two microstrip lines	77

5.3 Wideband design using analytical model	79
5.4 Performance	
5.4.1 Bandwidth	83
5.4.2 Distance between microstrip lines	84
5.4.3 Measurement	88
5.4.4 Tolerance for manufacturing accuracy	89
5.5 Conclusions	93
References	93

Chapter 6. Digital TV antennas for omnidirectional pattern synthesis

6.1 Introduction	94
6.2 Proposal of modified H shaped antenna	94
6.3 Performance	97
6.4 Prototype antennas	
6.4.1 Single element	107
6.4.2 Mounted antennas	108
6.5 RF module	110
6.6 Conclusions	112
References	112

Chapter 7. Digital TV antenna with thin structure

7.1 Introduction	114
7.2 Proposal of stub-loaded folded dipole antenna	114
7.3 Performance	115
7.4 Conclusions	119

References	119
Chapter 8. Digital TV antenna with wider bandwidth and thinner structure	
8.1 Introduction	120
8.2 Proposal of capacitor- and stub-loaded folded dipole antenna	120
8.3 Performance	122
8.4 Prototype antenna	132
8.5 Conclusions	138
References	139
Chapter 9. Conclusions	140
Acknowledgement	142
List of publications	143

Chapter 1. Introduction

1.1 Background of study

The mobility by vehicles is indispensable for our personal lives as well as business activities. There have been strong requirements of safety, comfortable time & space, and convenience for the mobility by vehicles.

In 1950s, AM radio reception was only available in vehicles. Several systems for these requirements have been gradually installed into vehicles with the growth of wireless technologies [1-1], [1-2]. FM radio and television (TV) programs can be currently received in vehicles. Drivers can achieve information of own positions by Global Positioning Systems (GPS) and congestion information by Vehicle Information and Communication systems (VICS). Electric toll collection (ETC) allows nonstop service to pay road fees. Smart Key Systems (SKS) and Tire Pressure Monitoring Systems (TPMS) improve convenience and safety. Telephone can be used in vehicle and Bluetooth helps links between mobile terminals of driver and vehicle terminals. Laser radars and millimeter-wave radars have been installed as forward looking sensors.

Automotive antenna design technique is one of the key techniques to contribute the system realization very much. Automotive antennas generally need simple architectures and low cost due to consumer products, and compactness or low profile due to limited installation spaces of vehicle. Also, inclusion of the vehicle body into the antenna design is needed, when antenna performance is strongly affected by the vehicle body.

The frequency bands used in automotive wireless systems range widely from AM band to the millimeter-wave band. The different frequency bands result in the different problems and difficulties of the development of antennas. The establishment of automotive antenna design techniques is needed in wide frequency range.

1.2 Scope of study

This doctoral dissertation titled “Study of Antenna Design Techniques for Use in Automotive Environment” presents analytical, numerical, and experimental investigations of automotive antenna design techniques, particularly, in the highest and nearly the lowest edges of the frequency bands assigned for automotive wireless systems. The two frequency bands are the millimeter-wave and UHF bands. The investigations of the two frequency bands would provide useful design insights of automotive antennas in wide frequency range. Considering the impact on industry, the two systems that are installed practically and work effectively in 2000s are focused. Those are millimeter-wave radar system and digital terrestrial television (TV) reception system.

Millimeter-wave radar systems were first launched for Adaptive Cruise Control (ACC) system by Daimler Chrysler in June 1999 [1-3]. ACC system allows automatic control of the vehicle speed following the front vehicles. Frequency of the 77 GHz band is used since it has robustness for fog and rains. There are two important parts in the RF front end modules, that are antennas and connections between millimeter-wave components. Ease of manufacture, low profile, and high efficiency are mainly required for the antennas. Microstrip antennas have inherent advantages of ease of manufacture and low profile, but efficiency is generally low. In this dissertation, a new configuration of microstrip antenna is proposed to achieve higher efficiency. With regard to connections, microstrip line to waveguide transitions are needed to connect microstrip antennas on the surface of the radar sensor and circuits inside the sensors via waveguides. A new transition and the design methodology are also proposed. The transition has a simple structure and can be etched in the same process of antennas.

Entertainment applications are spreading as well as safety applications. Digital terrestrial TV services have been available in Europe and North America since September

1998 [1-4]. In Japan, digital terrestrial TV services were started in three large cities, Tokyo, Osaka, and Nagoya in December 2003. Digital terrestrial TV services will gradually spread over the large area in Japan since current analog television services are terminated in July 2011. In this dissertation, two types of antennas are proposed in the view point for an omnidirectional pattern synthesis in a horizontal plane and a thin structure for narrow installation spaces. A further bandwidth enhancement method for the thin structured antenna is also proposed, resulting in covering digital TV band when the antenna is installed on window glass or spoiler.

This doctoral dissertation describes key technologies of novel automotive antennas for the two systems. The new concepts and configurations are verified with analytical, numerical, and experimental investigations. I believe that the investigations in this dissertation contribute to the advancements for automotive antenna design techniques in both academic and industrial points of view.

1.3 Dissertation organization

This doctoral dissertation is organized as shown in Fig.1.1. The scope of study is clarified with background in chapter 1. Chapter 2 describes conventional techniques of antennas and associate circuits for millimeter-wave radar and digital TV reception systems. Their problems are also presented when conventional techniques are applied for the two systems. A new microstrip array antenna is proposed for automotive radars in Chapter 3. The antenna has higher efficiency comparing with conventional microstrip antennas. In Chapter 4, a new transition from waveguide to microstrip line is proposed. The transition can be composed of a single dielectric layer and be etched in the same process of microstrip antennas. An optimum design for the transition is proposed in terms of bandwidth in Chapter 5. A

transition from waveguide to two microstrip lines is also investigated. Digital terrestrial TV antennas are described in Chapters 6, 7, and 8. In Chapter 6, a modified H shaped antenna is proposed in terms of omnidirectional pattern synthesis. In terms of installation spaces, a thin antenna with a width of 20 mm is proposed in Chapter 7. The antenna covers digital terrestrial TV band from 470 MHz to 710 MHz. In Chapter 8, an antenna with thinner structure and wider bandwidth is proposed. The antenna with a width of 15 mm covers double the frequency band, which is from 470 MHz to 950 MHz. Finally, this dissertation is concluded in Chapter 9.

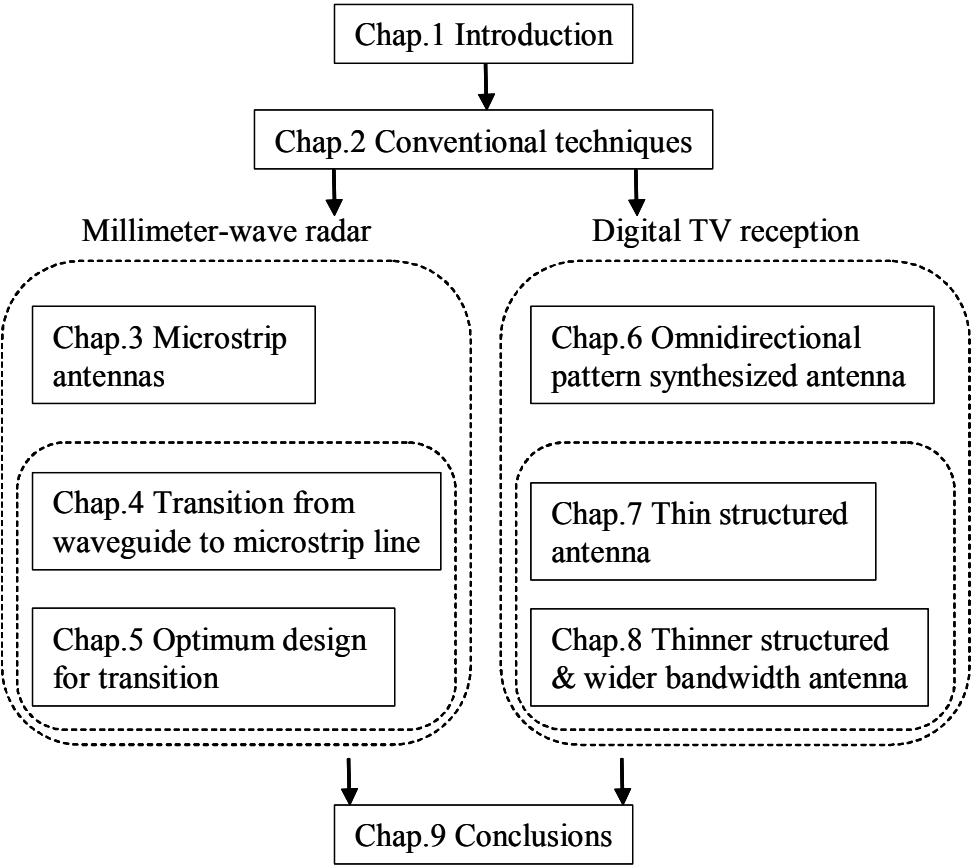


Fig. 1.1. Organization of this dissertation.

References

- [1-1] K. Fujimoto, "Overview of antenna systems for mobile communications and prospects for the future technology," *IEICE Trans. Commun.*, vol.E74-B, no.10, pp.3191-3201, Oct. 1991.
- [1-2] K. Nishikawa, "Land vehicle antennas," *IEICE Trans. Commun.*, vol.E86-B, no.3, pp.993-1004, Mar. 2003.
- [1-3] H. H. Meinel, "Automotive millimeter wave radar, status, trends and producibility," *Proc. Topical Symposium on Millimeter Waves*, pp.5-9, Yokohama, Japan, Mar. 2000.
- [1-4] Y. Wu, E. Pliszka, B. Caron, P. Bouchard and G. Chouinard, "Comparison of terrestrial DTV transmission systems: the ATSC 8-VSB, the DVB-T COFDM and the ISDB-T BST-OFDM", *IEEE Trans. Broadcast.*, vol.46, no.2, pp.101-113, Jun. 2000.

Chapter 2. Conventional techniques

2.1 Introduction

Conventional techniques of antennas and associated circuits for millimeter-wave radar system and digital TV reception system are presented in this chapter to clarify the problems that should be solved. These include millimeter-wave microstrip antennas, feed networks, transitions from waveguide to microstrip line, and digital TV antennas.

2.2 Conventional millimeter-wave antennas

2.2.1 Millimeter-wave radars and their antennas

Millimeter-wave automotive radars have been developed not only for forward looking sensors but also for rear and side looking sensors [2-1]-[2-7]. Long range radars in the 77 GHz band have been on the market since 1999 for Adaptive Cruise Control (ACC), and short range radars in the 24 GHz band came on the market in 2005. In the ACC systems, the beam is mechanically [2-4] or electrically [2-7] scanned in the azimuth angle up to ± 10 degrees to detect targets even on a curved road. Figures 2.1 (a) and (b) show arrangements of transmitting and receiving antennas for mechanical and electrical scanning radars. A pencil

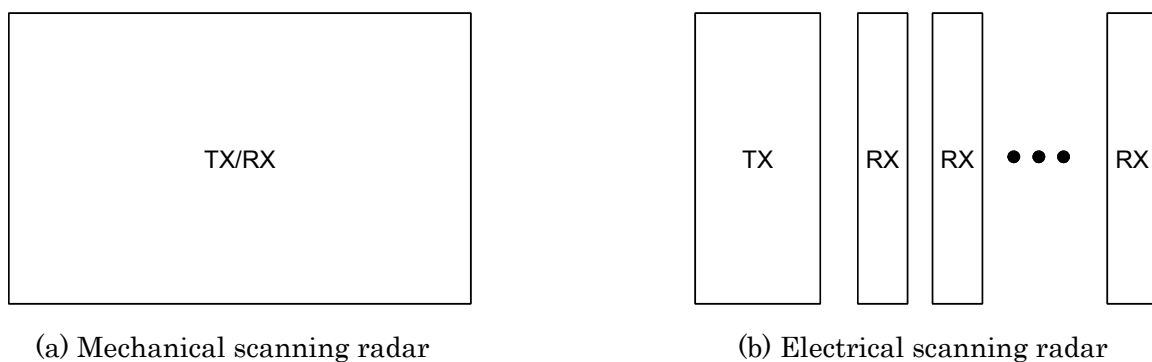


Fig. 2.1. Arrangements of transmitting and receiving antennas for mechanical and electrical scanning radars.

beam antenna is used for mechanical scanning radars, as shown in Fig. 2.1 (a). The pencil beam antenna works as transmitting and receiving antennas, and is scanned mechanically in the azimuth plane. In contrast, one transmitting antenna and plural receiving subarrays with fan beam in the azimuth plane are placed for electrical scanning radars, as shown in Fig. 2.1 (b). The transmitting antenna covers the detection angle in the azimuth plane. Received signals by the plural subarrays are combined by the beam forming technique, resulting in beam scanning in the azimuth plane. With regard to polarization, linear polarization inclined at 45 degrees is commonly utilized to provide polarization isolation between the back scattered signal and signals from on-coming traffic.

The antenna for the automotive radars is required to have high aperture efficiency, which means high gain for an aperture area determined by the dimensions of a radar sensor, in order to detect targets at a long range of 150 m. The polarization of the antenna should be 45-degree inclined linear polarization. In addition, low profile is required so as not to spoil the appearance of a vehicle. With regard to the wide spread adoption of the automotive radars, ease of manufacture is also one of the significant factors. The frequency range is from 76 GHz to 77 GHz. Gain and sidelobe level in the elevation plane of the subarray for electrical scanning radars should be higher than 22 dBi and lower than -15 dB, respectively. Beamwidth in the azimuth plane needs wider than 20 degrees. For mechanical scanning radars, gain and sidelobe levels in both the azimuth and elevation planes are required to be higher than 31 dBi and lower than -15 dB, respectively.

Several types of antennas have been developed, including the triplate antenna [2-4], dielectric lens antenna [2-8], folded reflector antenna [2-9], slot antenna [2-10], [2-11], dielectric leaky wave antenna [2-12], microstrip antenna [2-5], [2-6], [2-13]-[2-17], and others. The choice of antenna depends on the specifications required for the system, such as cost, performance, size, producibility, and so on. These antennas are compared in terms of

Table 2.1. Comparisons of antennas for Toyota CRDL radar requirements.

Antenna types	Performance (Efficiency)	Size (Thickness)	Cost
Triplate antenna	O	O	Δ
Dielectric lens antenna	O	×	O
Folded reflector antenna	O	Δ	Δ
Slot antenna	O	O	Δ
Dielectric leaky wave antenna	O	O	Δ
Microstrip antenna	Δ	O	O

(O: Good, Δ: Fair, ×: Poor, for Toyota CRDL radar requirements)

performance, size, and cost for the requirements of radars [2-7] developed by Toyota CRDL Inc. in Table 2.1.

2.2.2 Microstrip antennas

Microstrip antennas have advantages of low profile and ease of manufacture, and can be etched on common substrates such as Teflon glass fiber. Thus, a type of microstrip antenna becomes a good candidate when radar sensors are widely used in vehicles, due to its advantages. This dissertation focuses on microstrip antennas.

Figure 2.2 shows a typical microstrip array antenna [2-6]. The radiating elements and feed line are printed on the dielectric substrate with ground plane at the backside. The radiating elements are inclined at $\phi = -45$ degrees for the feed line to generate polarization inclined at -45 degrees. The amplitude distribution of the antenna is controlled by the dividers to achieve desired distribution such as Taylor distribution. The distance between the dividers is set at a nearly guided wavelength, λ_g , so that the all radiating elements may be excited in phase. The divider consists of impedance transformers with a quarter wavelength, λ_g .

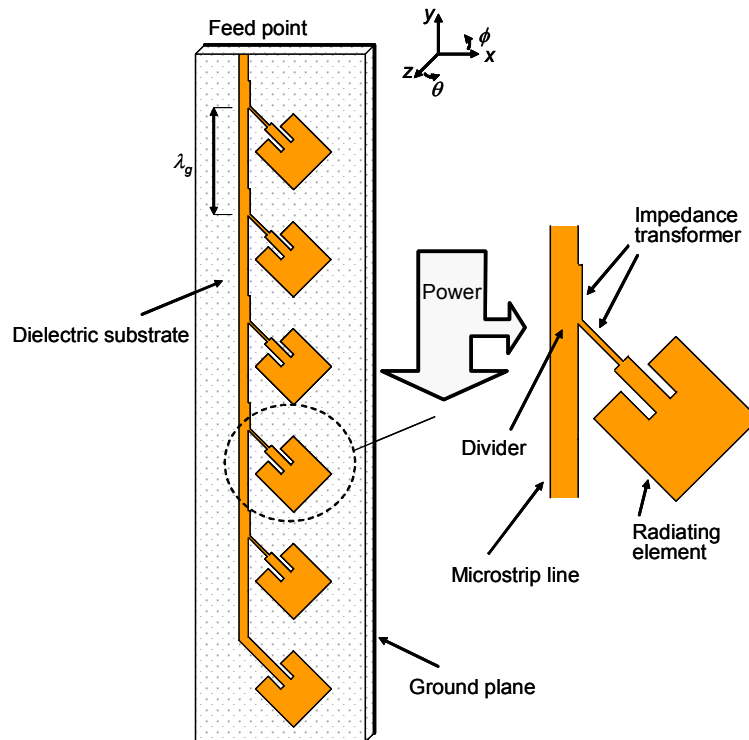


Fig. 2.2. Configuration of typical microstrip array antenna.

However, the problem is that aperture efficiency of the microstrip array antenna decreases as the aperture area becomes larger. Referring to prior work on microstrip antennas in the millimeter-wave band [2-13]-[2-15], we estimate that maximum achievable aperture efficiency of a fan beam microstrip antenna having gain of around 20 dBi in the 76 GHz band is limited to 40 %. Likewise, aperture efficiency of a pencil beam microstrip antenna of 30 dBi gain in the 76 GHz band is estimated less than 30 %. The degradation of aperture efficiency appears to be caused by two major reasons. One is the loss of the feed line, which includes discontinuities such as T-junctions and bends, and a microstrip line itself. Another is poor tolerance to set amplitude distribution. The minimum width of the microstrip line etched on Teflon glass fiber substrate is generally about 0.1 mm by the limitation of manufacturing accuracy in case that a relatively large array antenna is etched on it. The

power dividing ratio of the T-junction is limited nearly 4:1 in this condition. Thus desired amplitude distribution cannot be set and aperture efficiency goes down when the feed line of the array antenna requires the power dividing ratio larger than 4:1.

A type of combline antenna [2-16], [2-17] is a candidate of microstrip array antennas with the minimum loss of the feed line because there is neither divider nor bend and the microstrip line is straight. Figure 2.3 (a) shows a linearly polarized combline antenna. The radiating elements are connected perpendicular to the feed line, and the polarization has the x direction. Radiation conductance of each radiating element is controlled with variation of the width W . The length L has a half resonant wavelength. On the other hand, a circular polarized combline antenna is shown in Fig. 2.3 (b). The radiating elements inclined at 45 degrees and

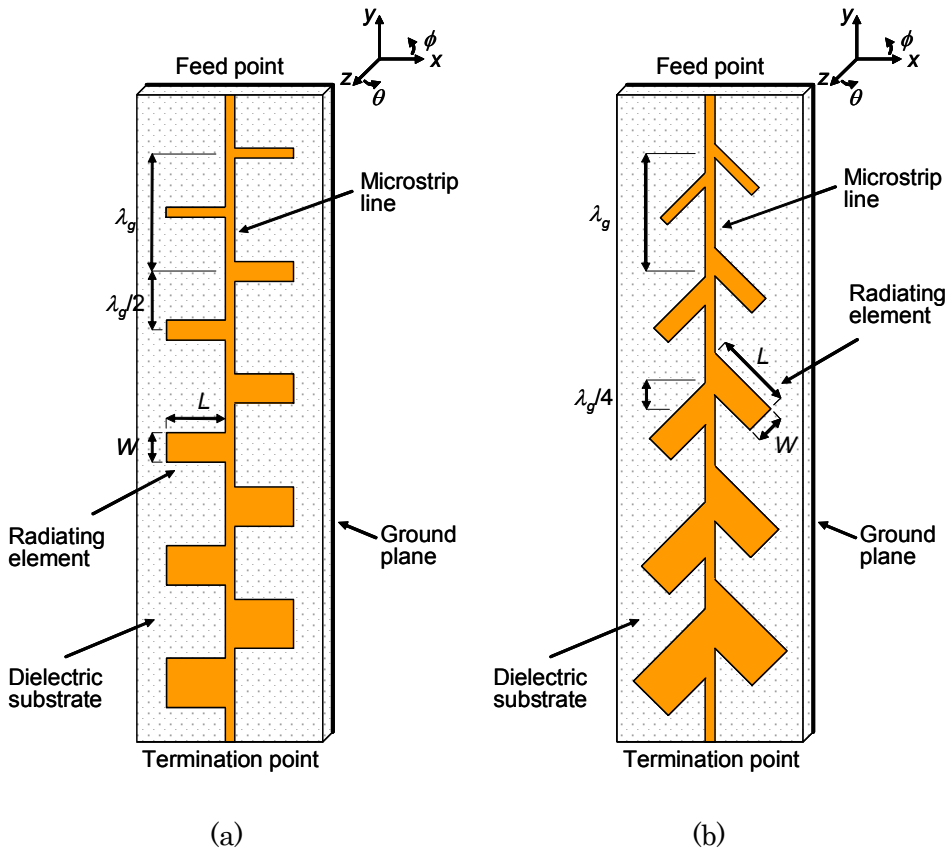


Fig. 2.3. Configurations of combline antennas. (a) Linear polarization and (b) circular polarization.

- 45 degrees are placed on both sides of the feed line in the spacing of a quarter wavelength along the feed line.

The one edge of the radiating element inclined at 45 degrees is connected to the feed line, as shown in Fig. 2.3 (b). There would be a problem that the excited mode in the radiating element degrades as the width W of the radiating element becomes wider. Thus radiation conductance for co-polarization has to be widely controlled, keeping the excited mode for cross-polarization negligibly small even when the width of the radiating element inclined at 45 degrees is wider. A new configuration of microstrip linear array antenna is proposed in Chapter 3. The antenna achieves simultaneously low feed line loss and negligibly small excitation for cross-polarization mode.

2.2.3 Feed networks

A feed network between a feed point and plural linear arrays is important in terms of high efficiency for an array antenna having a pencil beam for mechanical scanning radars. Because aperture efficiency is sensitive to feed networks, as the aperture area becomes larger. Figure 2.4 (a) shows a typical array antenna consisting of plural linear arrays. Conventional feed networks include a series circuit of Fig. 2.4 (b) and parallel circuit of Fig. 2.4 (c). The features of the circuits are summarized in Table 2.2. The series feed circuit has lower feed line loss compared with the parallel feed circuit because the total length of the feed line in the series feed circuit is shorter than that in the parallel feed circuit. But the design tolerance of setting amplitude distribution in the series feed circuit is poor due to the limited power dividing ratio of the T-junctions. Thus, desired amplitude distribution cannot be set, and the aperture area cannot fully work, resulting in the decrease of aperture efficiency in case of the series feed circuit.

A feed circuit is required to have features of both lower feed line loss and setting desired

amplitude distribution with small power dividing ratio of the T-junctions less than 4:1. A new feed circuit is proposed to achieve the both performance simultaneously in Chapter 3.

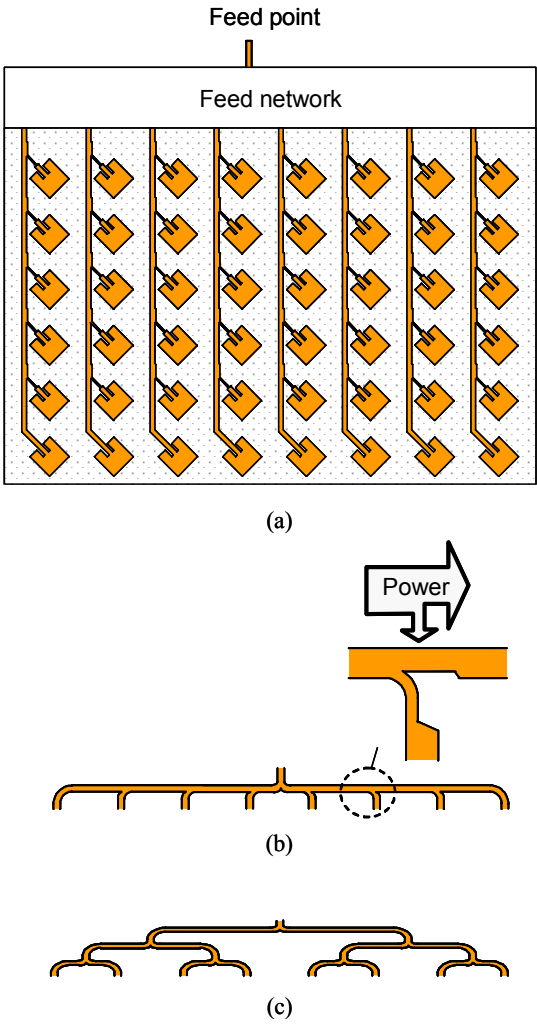




Fig. 2.4. Feed networks for array antenna. (a) Configuration of typical array antenna. (b) Series circuit and (c) parallel circuit.

Table 2.2. Features of series and parallel circuits.

Feed network	Feed loss	Design flexibility of aperture distribution
 Series	Small	Poor
 Parallel	Large	Good

2.3. Conventional millimeter-wave transitions

When microstrip antennas are selected for the radar system, microstrip antennas are placed on the surface of a radar sensor, and are connected to millimeter-wave circuits inside the sensor via waveguides. In the configurations, transitions from waveguide to microstrip line are required.

Several types of transitions from waveguide to microstrip line have been reported. The ridge waveguide type [2-18], quasi-yagi type [2-19], and planar waveguide type [2-20] have been studied as longitudinal transition from waveguide to microstrip line. With regard to vertical transitions used in the configuration described, transitions of probe feeding type have been reported [2-21], [2-22]. Figure 2.5 shows a transition of probe feeding type. The microstrip line and ground pattern are etched on the dielectric substrate. The ground plane is etched on the backside. The transition needs the waveguide short block with a quarter

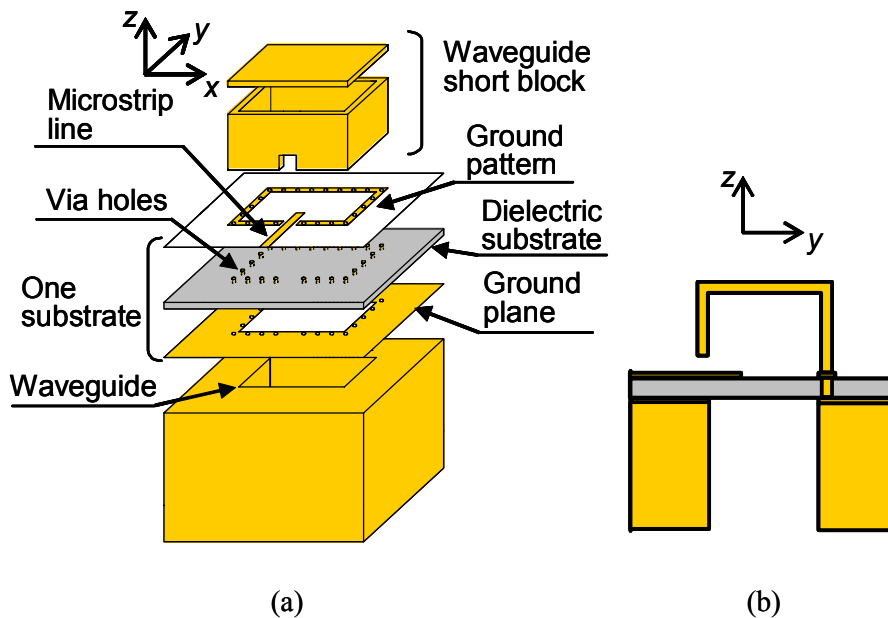


Fig. 2.5. Configurations of transition of probe feeding type. (a) Perspective view and (b) cross section.

wavelength to achieve sufficient coupling between the waveguide and the microstrip line. Although the transition has a low loss characteristic in millimeter-wave band, the structure is not suitable for mass production, due to the usage of the metal short block.

A way to replace the metal short block is to place a patch element in the waveguide to achieve sufficient coupling between the waveguide and the microstrip line. Figure 2.6 shows a transition of slot coupling type [2-23], where the microstrip line is coupled with the rectangular patch element in the waveguide by means of a slot. The transition needs an additional substrate instead of a metal short block.

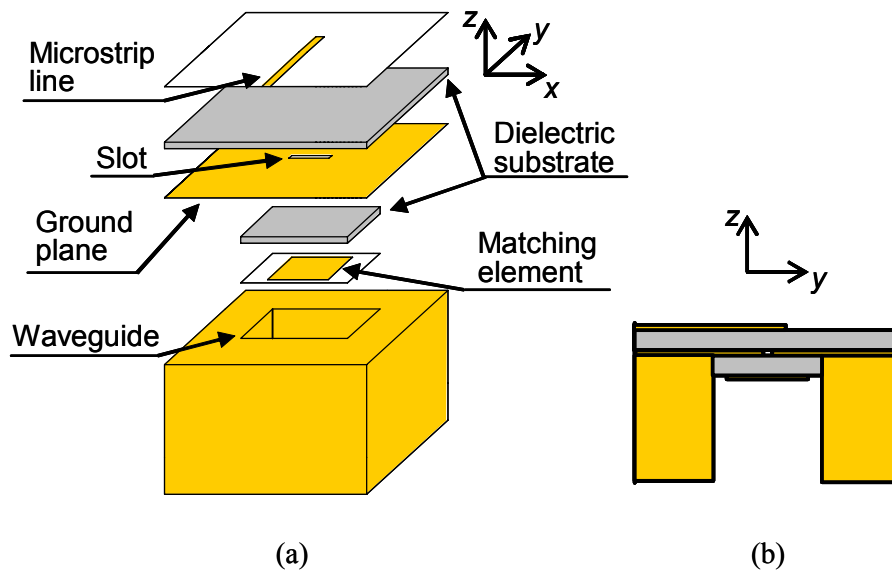


Fig. 2.6. Configurations of transition of slot coupling type. (a) Perspective view and (b) cross section.

A transition having neither a metal short block nor an additional substrate is desired to be suitable for mass production. A new type of transition is proposed in Chapter 4, which can be composed of a single dielectric substrate attached to the waveguide and is suitable for mass production.

A wideband characteristic improves the assembly tolerance, considering the shifts in the resonant frequency that are mainly caused by assembly errors. But a wideband design for a transition having a patch element in the waveguide has not been reported, to the authors' knowledge. A wideband design methodology is proposed in Chapter 5. The optimum dimensions of transitions are derived.

Where a microstrip line divider is needed between the transition and the microstrip antenna, a transition working as a divider would provide a compact feed network. With regard to the number of microstrip lines, the transitions [2-18]-[2-23] have one microstrip line. A transition working as a divider has been also reported [2-24]. Since it does not have a patch element in the waveguide, it needs a tapered waveguide. A transition from a waveguide to two microstrip lines is also proposed in Chapter 5.

2.4. Conventional digital TV antennas

2.4.1 Digital TV reception system for vehicles

Digital terrestrial services have been available in Europe and North America since September 1998, and some transmission systems have been studied [2-25], [2-26]. Digital terrestrial services were started in three large cities, Tokyo, Osaka and Nagoya, in Japan in December 2003 and are expected to have spread over a large area by the termination of current analog TV in July 2011. Terrestrial Integrated Services Digital Broadcasting (ISDB-T) system has been adopted [2-27]. Frequency bandwidth is assigned from 470 MHz to 710 MHz and horizontal polarization is utilized. ISDB-T system offers various sorts of services, which are High Definition Television (HDTV) service for fixed reception, mobile multimedia services for mobile reception and the like.

Toyota CRDL Inc. has set itself the goal of developing an automotive digital terrestrial

reception system to enable the enjoyment of HDTV service in a vehicle. In order to achieve the stable reception, the reception system has adopted an adaptive array using four antennas based on the Maximal Ratio Combining (MRC) method [2-28]. Figure 2.7 shows a digital TV reception system for a vehicle. The received signals of the four antennas are down-converted, weighted and combined in the control system. The weight vector for each signal is controlled, based on the MRC method. Performance of the reception system greatly depends on performance of the antennas, which is, particularly, radiation pattern in the horizontal plane. The combined pattern has the peak to the direction of incoming desired wave. The steered beam of the combined pattern is required to have an almost constant gain across 360 degrees in the horizontal plane. Peak plot is defined as plotted pattern of the peak of the combined pattern, and is used to evaluate performance of antennas.

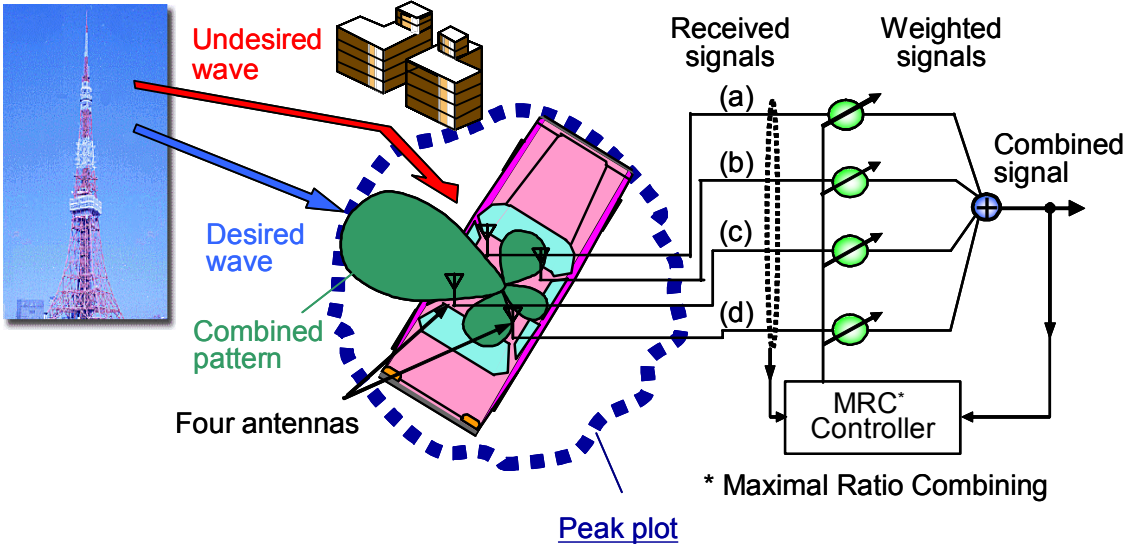


Fig. 2.7. Digital TV reception system.

2.4.2 Radiation pattern of mounted antennas

Pole antennas have been in use for AM radio reception since the 1950s and covered for VHF and UHF bands [2-29], [2-30]. Pole antennas will still be used for some types of cars due to their advantages of low cost and easy installation. On-glass antennas are generally preferred for car installation since they do not spoil the appearance of the car. On-glass antennas installed on the rear window have been developed for AM/FM radio and analog television [2-31]-[2-33].

Figure 2.8 shows typical installation positions of on-glass antennas. The installation positions are limited to the top of the front and rear windows in the point of view for antenna performance, maintaining the driver's view, and so on.

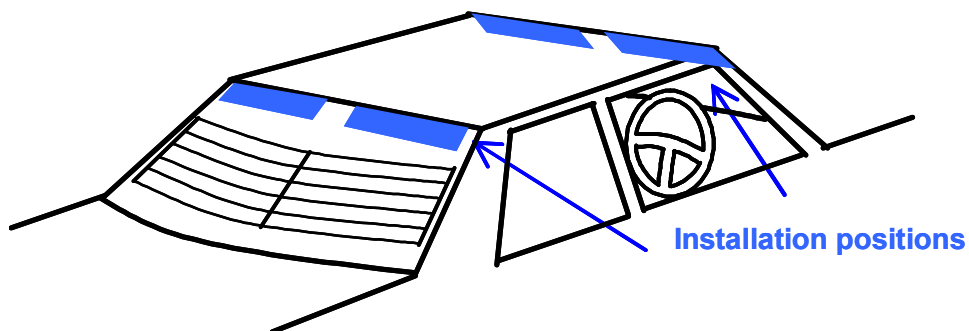


Fig. 2.8. Installation positions of antennas for car.

Directivity of mounted antennas is described. Figures 2.9 (a) and (b) show measured peak plots of conventional antennas. When loop antennas were installed at the top of front and rear windows, the peak plot has unacceptable weak gain at the sides, as shown in Fig. 2.9 (a). Because front and rear antennas had gain to the front and rear directions, respectively. On the other hand, the peak plot of pole antennas that are on the market is shown in Fig. 2.9

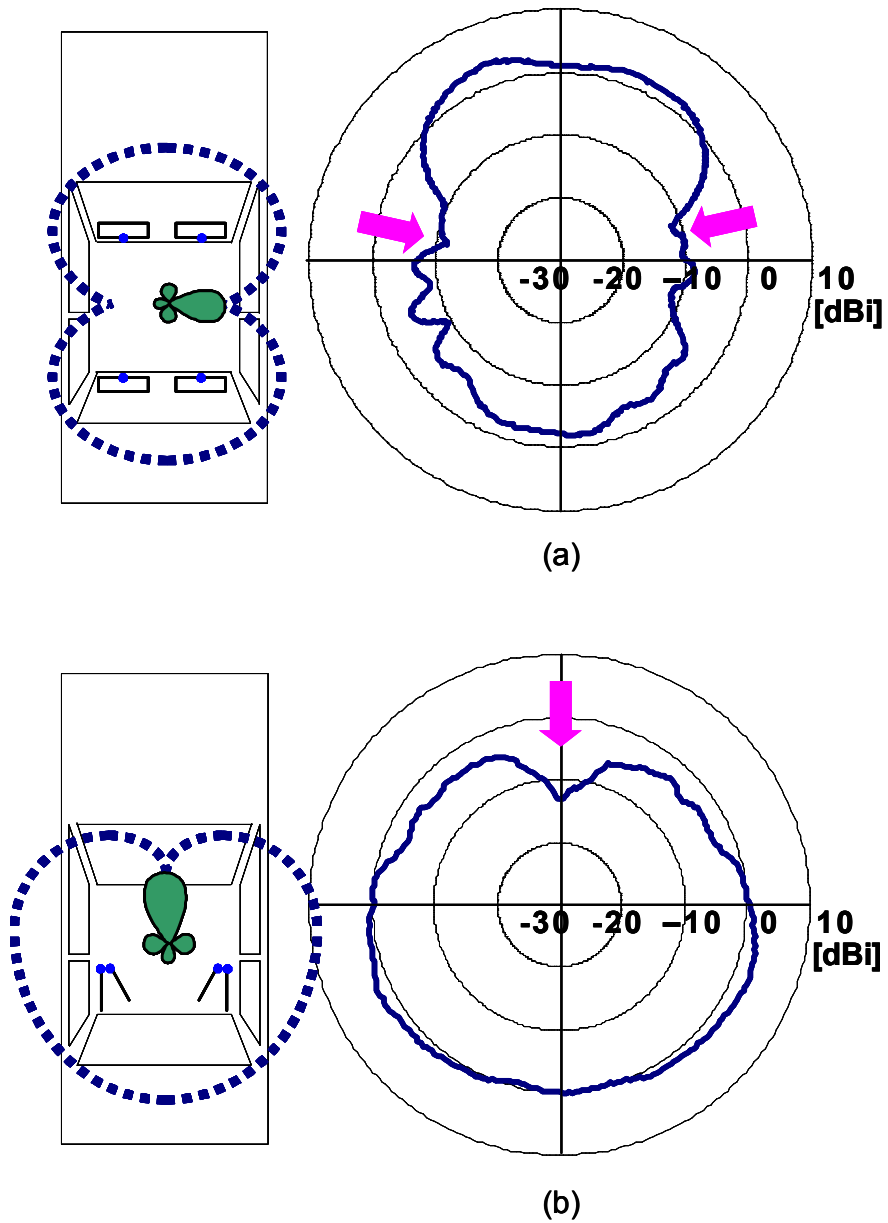


Fig. 2.9. Measured peak plot of conventional antennas. (a) Loop antenna and (b) pole antenna.

(b). The pole antennas were installed on the roof. The peak plot has unacceptably weak gain to the front.

The problem was clarified from the measurement results of Figs. 2.9 (a) and (b) that the peak plots of conventional antennas have unacceptably weak gain in the horizontal plane.

On-glass antennas with omnidirectional peak plot are desired when they are installed at the front and rear windows. A technique of omnidirectional pattern synthesis is proposed for on-glass antennas in Chapter 6.

2.4.3 Wideband methods

Since digital TV broadcasting services uses a relative bandwidth of 41 %, ranging from 470 MHz to 710 MHz, a wideband method for on-glass antennas is required to cover the bandwidth. Several bandwidth enhancement methods have been studied for dipole antennas. Types of thick dipole arms have been reported. Fig. 2.10 shows a bowtie antenna [2-34]. The antenna has two triangular arms and exhibits a wideband characteristic. The shapes of arms have been studied, including circular arms [2-35] and square arms [2-36], [2-37]. But these are not particularly suitable for installation on the windshield because of the importance of protecting the driver’s field of view. The use of parasitic elements besides a dipole in an open sleeve dipole design [2-38], [2-39] is also a useful method, but the feed line between the antenna and RF circuit cannot be printed on the glass together with the antenna due to the physical limitations of the parasitic element.

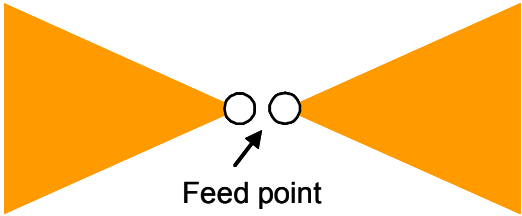


Fig. 2.10. Configuration of bowtie antenna.

Also, installation spaces are generally limited for vehicles. In case of a sedan type, installation positions have been shown in Fig. 2.8, but the development of antennas is still required for other types of vehicles. A thinner structure is suitable for narrower installation space near the edge of windows at the sides as well as the front and rear of vehicles.

Considering all types of vehicles, a thin structured antenna is required. A thin structure composed of thin wires is proposed in Chapter 7. The antenna covers the frequency range from 470 MHz to 710 MHz.

It is generally occurred that the operating frequency of antennas goes down when installed into a vehicle, which is mainly due to the individual permittivity of the materials used in automotive body parts. Thus, the dimensions of the antenna must be adjusted to compensate for shifts in operating frequency, depending on the installation position as well as the vehicle type. If the bandwidth of the operating frequency becomes much wider, then the antenna would be able to cover the digital terrestrial TV band even when operating frequency shifts occur. This would save the efforts involved in and the time required for the adjustment, thereby improving production availability. An antenna with wider bandwidth and thinner structure is proposed in Chapter 8. The antenna in free space provides double the frequency bandwidth of the antenna described in Chapter 7, ranging from 470 MHz to 950 MHz.

2.5 Conclusions

Conventional techniques for millimeter-wave antennas, transitions, and digital TV antennas were presented. The current problems were clarified. This dissertation will propose new configurations later.

References

- [2-1] M. E. Russell, C. A. Drubin, A. S. Marinilli, and W. G. Woodington, "Integrated automotive sensors," *IEEE Trans. Microwave Theory Tech.*, vol.50, no.3, pp.674-677, Mar. 2002.
- [2-2] H. H. Meinel, "Automotive millimeter wave radar, status, trends and producibility," *Proc. Topical Symposium on Millimeter Waves*, pp.5-9, Yokohama, Japan, Mar. 2000.
- [2-3] K. M. Strohm, H. L. Bloecher, R. Schneider, and J. Wenger, "Development of future short range radar technology," *Proc. 2nd Euro. Radar Conf.*, pp.165-168, Paris, Oct. 2005.
- [2-4] K. Fujimoto, "Current status and trend of millimeter-wave automotive radar," *Microwave Workshops Exhibition Dig.*, pp.225-230, Yokohama, Japan, Dec. 1995.
- [2-5] M. E. Russell, A. Crain, A. Curran, R. A. Campbell, C. A. Drubin, and W. F. Miccioli, "Millimeter-wave radar sensor for automotive intelligent cruise control (ICC)," *IEEE Trans. Microwave Theory Tech.*, vol.45, no.12, pp.2444-2453, Dec. 1997.
- [2-6] S. Ohshima, Y. Asano, T. Harada, N. Yamada, M. Usui, H. Hayashi, T. Watanabe, and H. Iizuka, "Phase-comparison monopulse radar with switched transmit beams for automotive application," *1999 IEEE MTT-S Int. Microwave Symp. Dig.*, vol.4, pp.1493-1496, Anaheim, CA, Jun. 1999.
- [2-7] Y. Asano, "Millimeter-wave holographic radar for automotive applications," *Microwave workshops and exhibition digest*, pp.157-162, Yokohama, Japan, Dec. 2000.
- [2-8] D. A. Williams, "Millimeter wave radars for automotive applications," *1992 IEEE MTT-S Int. Microwave Symp. Dig.*, vol.2, pp.721-724, Albuquerque, NM, Jun. 1992.
- [2-9] W. Menzel, D. Pilz, and R. Leberer, "A 77-GHz FM/CW radar front-end with low-profile low-loss printed antenna," *IEEE Trans. Microwave Theory Tech.*, vol.47,

- no.12, pp.2237-2241, Dec. 1999.
- [2-10] J. Hirokawa and M. Ando, "Efficiency of 76-GHz post-wall waveguide-fed parallel plate slot arrays," *IEEE Trans. Antennas Propagat.*, vol.48, no.11, pp.1742-1745, Nov. 2000.
- [2-11] K. Sakakibara, T. Watanabe, K. Sato, K. Nishikawa, and K. Seo, "Millimeter-wave slotted waveguide array antenna manufactured by metal injection molding for automotive radar systems," *IEICE Trans. Commun.*, vol.E84-B, no.9, pp.2369-2376, Sept. 2001.
- [2-12] T. Teshirogi, Y. Kawahara, A. Yamamoto, Y. Sekine, N. Baba, and M. Kobayashi, "High-efficiency, dielectric slab leaky-wave antennas," *IEICE Trans. Commun.*, vol.E84-B, no.9, Sept. 2001.
- [2-13] M. A. Weiss, "Microstrip antennas for millimeter waves," *IEEE Trans. Antennas Propag.*, vol.29, no.1, pp.171-174, Jan. 1981.
- [2-14] W. Menzel, "A 40 GHz microstrip array antenna," *IEEE MTT-S Int. Symp. Dig.*, pp.225-226, Washington, D.C., USA, May 1980.
- [2-15] K. J. Button, "*Infrared and millimeter waves, Pt.5 Millimeter components and techniques*," vol.14, Academic press, 1985.
- [2-16] J. R. James and G. J. Wilson, "Microstrip antenna arrays," *US Patent*, 4063245, 13 Dec. 1977.
- [2-17] J. R. James and P. S. Hall, "Microstrip antennas and arrays. Pt. 2 New array design technique," *IEE Journal of Microwave, Optics and Acoustics*, vol.1, No.5, pp.175-181, Sept., 1977.
- [2-18] H. W. Yao, A. Abdelmonem, J. F. Liang, and K. A. Zaki, "Analysis and design of microstrip to waveguide transitions," *IEEE Trans. Microwave Theory Tech.*, vol.42, no.12, pp.2371-2379, Dec. 1994.

- [2-19] N. Kaneda, Y. Qian, and T. Itoh, "A broad-band microstrip-to-waveguide transition using quasi-Yagi antenna," *IEEE Trans. Microwave Theory Tech.*, vol.47, no.12, pp.2562-2567, Dec. 1999.
- [2-20] D. Deslandes and K. Wu, "Integrated microstrip and rectangular waveguide in planar form," *IEEE Microwave Wireless Components Lett.*, vol.11, no.2, Feb. 2001.
- [2-21] T. Q. Ho and Y. C. Shih, "Spectral-domain analysis of E-plane waveguide to microstrip transitions," *IEEE Trans. Microwave Theory Tech.*, vol.37, no.2, pp.388-392, Feb. 1989.
- [2-22] Y. Leong and S. Weinreb, "Full band waveguide to microstrip probe transitions," *1999 IEEE MTT-S Int. Microwave Symp. Dig.*, vol.4, pp.1435-1438, Anaheim, CA, May 1999.
- [2-23] W. Grabherr, B. Hudder, and W. Menzel, "Microstrip to waveguide transition compatible with mm-wave integrated circuits," *IEEE Trans. Microwave Theory Tech.*, vol.42, no.9, pp.1842-1843, Sept. 1994.
- [2-24] M. Davidovitz, "Wide band waveguide to microstrip transition and power divider," *IEEE Microwave Guided Wave Lett.*, vol.6, no.1, pp.13-15, Jan. 1996.
- [2-25] Y. Wu, E. Pliszka, B. Caron, P. Bouchard and G. Chouinard, "Comparison of terrestrial DTV transmission systems: the ATSC 8-VSB, the DVB-T COFDM and the ISDB-T BST-OFDM", *IEEE Trans. Broadcast.*, vol.46, no.2, pp.101-113, Jun. 2000.
- [2-26] T. Kuroda and M. Sasaki, "Terrestrial ISDB system using band segmented transmission scheme", *Proc. 20th Int. television symp.*, pp.641-671, Montreux, Switzerland, Jun. 1997.
- [2-27] ARIB, *Receiver for digital broadcasting – ARIB STD-B21*, 4.2, Oct. 16, 2003.
- [2-28] J. Imai, M. Fujimoto, T. Shibata, N. Suzuki, N. Itoh and K. Mizutani, "Experimental results of diversity reception for terrestrial digital broadcasting", *IEICE Trans.*

- Commun.*, vol.E85-B, no.11, pp.2527-2530, Nov. 2002.
- [2-29] R. G. Vaughan, J. B. Andersen and M. H. Langhorn, "Circular array of outward sloping monopoles for vehicular diversity antennas", *IEEE Trans. Antennas Propag.*, vol.36, No.10, pp.1365-1374, Oct. 1988.
- [2-30] S. Egashira, T. Tanaka and A. Sakitani, "A design of AM/FM mobile telephone triband antenna", *IEEE Trans. Antennas Propag.*, vol.42, No.4, pp.538-540, Apr. 1994.
- [2-31] H. K. Lindenmeier, J. F. Hopf and L. M. Reiter, "Antenna and diversity techniques for broadcast reception in vehicles", *IEEE Int. Antennas Propagat. Symp. Dig.*, pp.1097-1100, Chicago, IL, USA, Jul. 1992.
- [2-32] K. Fujimoto and J. R. James, *Mobile antenna systems handbook*, 2nd ed., Artech house, 2001.
- [2-33] R. Abou-Jaoude and E. K. Walton, "Numerical modeling of on-glass conformal automobile antennas", *IEEE Trans. Antennas Propag.*, vol.46, No.6, pp.845-852, Jun. 1998.
- [2-34] R. C. Johnson and H. Jasik, *Antenna Engineering Handbook*, 2nd ed., Mcgraw-hill, 1984, p.29-12.
- [2-35] N. P. Agrawall, G. Kumar, and K. P. Ray, "Wide-band planar monopole antennas," *IEEE Trans. Anetnnas Propag.*, vol. 46, no. 2, pp. 294–295, Feb. 1998.
- [2-36] M. J. Ammann and Z. N. Chen, "A wide-band shorted monopole with bevel," *IEEE Trans. Anetnnas Propag.*, vol. 51, no. 4, pp. 901–903, Apr. 2003.
- [2-37] K. L. Wong, C. H. Wu, and S. W. Su, "Ultrawide-band square planar metal-plate monopole antenna with a trident-shaped feeding strip," *IEEE Trans. Anetnnas Propag.*, vol. 53, no. 4, pp. 1262–1269, Apr. 2005.
- [2-38] H. E. King and J. L. Wong, "An experimental study of a balun-fed open sleeve dipole in front of a metallic reflector," *IEEE Trans. Antennas Propag.*, vol. 20, no. 2, pp.

201–204, Mar. 1972.

- [2-39] T. G. Spence and D. H. Werner, “A novel miniature broadband/multiband antenna based on an end-loaded planar open-sleeve dipole,” *IEEE Trans. Antennas Propag.*, vol. 54, no. 12, pp. 3614–3620, Dec. 2006.

Chapter 3. Millimeter-wave microstrip antennas for automotive radars

3.1 Introduction

A new configuration of microstrip linear array antenna [3-1]-[3-4] is proposed for automotive radars in this chapter. The antenna has an advantage of high aperture efficiency as well as low profile and ease of manufacture. The configuration of the proposed microstrip linear array antenna is presented in Section 3.2. The features of the proposed antenna are also presented from the points of view for coupling coefficient of the radiating element and feed line loss in Section 3.3. The radiating element is analyzed by the cavity model to make clear the controllable range of radiation conductance for co-polarization as well as relations to radiation conductance for cross-polarization, conductor loss and dielectric loss. The design of the linear array antenna taking the feed line loss into account is presented and feed line loss is estimated. In Section 3.4, performance of two types of the developed antennas is described and discussed in terms of aperture efficiency for electrically scanning antenna and mechanically scanning antenna having a new feed circuit. This chapter is concluded in Section 3.5.

3.2 Proposal of microstrip antenna

Figure 3.1 shows the configuration of a microstrip linear array antenna for automotive radars. A straight microstrip line and rectangular radiating elements are printed on one side of a dielectric substrate with a ground plane on the other side. The rectangular radiating elements inclined at 45 degrees to the straight microstrip line are placed on both sides of the microstrip line and are directly connected to the microstrip line at their corners without dividers or impedance transformers. Radiation conductance of each rectangular radiating element is controlled by changing the width W of each rectangular radiating element and is

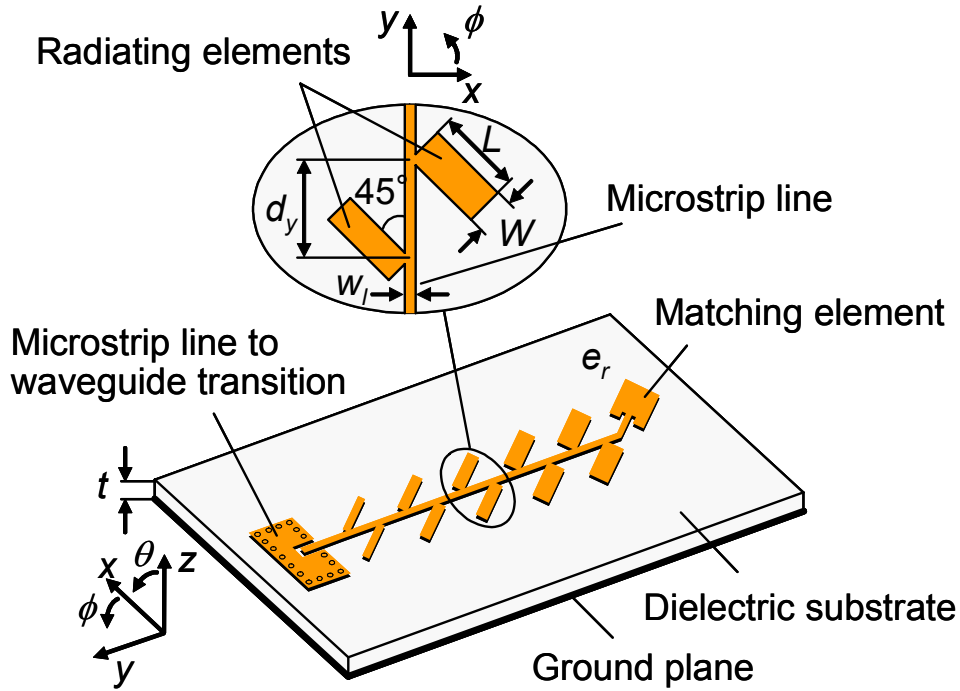


Fig. 3.1. Configuration of the proposed microstrip linear array antenna for automotive radars.

determined to satisfy aimed amplitude distribution of the microstrip linear array antenna. The length L of each rectangular radiating element is chosen to be a half resonant wavelength. The element spacing d_y in the y direction is set to approximately a half guided wavelength so that all of the rectangular radiating elements may be excited in phase. The microstrip line is terminated by a rectangular matching element to suppress the reflection of the residual power and radiate it at the end of the microstrip line. The antenna is fed by a waveguide (WR-12) through the microstrip line to waveguide transition at the opposite end of the microstrip line. The transition has a feature of low loss and is made by the same manufacturing process as the antenna. Details of the transition will be described in Chapter 4. Design frequency is 76.5 GHz, which is the center of the frequency bandwidth utilized for automotive radars. The dielectric substrate has the thickness $t = 0.0324 \lambda_0$ and relative dielectric constant $\epsilon_r = 2.2$.

λ_0 is a wavelength in free space at 76.5 GHz. The width w_l of the microstrip line is $0.0765 \lambda_0$. Characteristic impedance Z_0 is set to 60Ω so that the coupling coefficient of the radiating element may cover the appropriate range for setting aimed amplitude distribution. The number of elements is chosen 37 elements for the developed antenna due to the vertical dimension constraint. The length of the linear array antenna is approximately $15 \lambda_0$. In order to achieve sidelobe level below -15 dB including fabrication errors in mass produce, amplitude distribution of the linear array antenna is set Taylor distribution with -17 dB sidelobe level. The main beam is tilted so as to suppress the over all reflection at the input port. The tilt angle of the main beam is set to -3 degrees in the y direction since the small tilt angle is better for the installation of the radar sensor to a vehicle.

3.3 Design of linear array including losses

3.3.1 Coupling coefficient of radiating element

The design of the radiating element is first presented. To set aimed amplitude distribution accurately is important and is required together with lower feed line loss in terms of aperture efficiency because degradation of amplitude distribution causes reduction of aperture efficiency. In other words, radiation conductance for co-polarization has to be controlled widely enough to set amplitude distribution. Thus coupling coefficients for radiation power, conductor loss and dielectric loss are evaluated here by the cavity model with co- and cross-polarization modes.

The radiating element is simply modeled to a cavity excited at the feed point F in Figure 3.2 (a). Calculated dielectric substrate has the thickness $t = 0.0324 \lambda_0$, relative dielectric constant $\epsilon_r = 2.2$ and loss tangent $\tan \delta = 0.001$. The area of the feed point F is assumed to be rectangular $\Delta_u \times \Delta_v$. It is also assumed that TM mode is excited in the radiating element

since the thickness of the substrate is much thinner than a wavelength in the substrate. The equivalent circuit of the radiating element connected to a feed line is presented in Figure 3.2 (b). The equivalent circuit is given with series connection of parallel resonant circuits for TM_{mn} modes to distinguish coupling coefficient of each mode. Conductor loss and dielectric

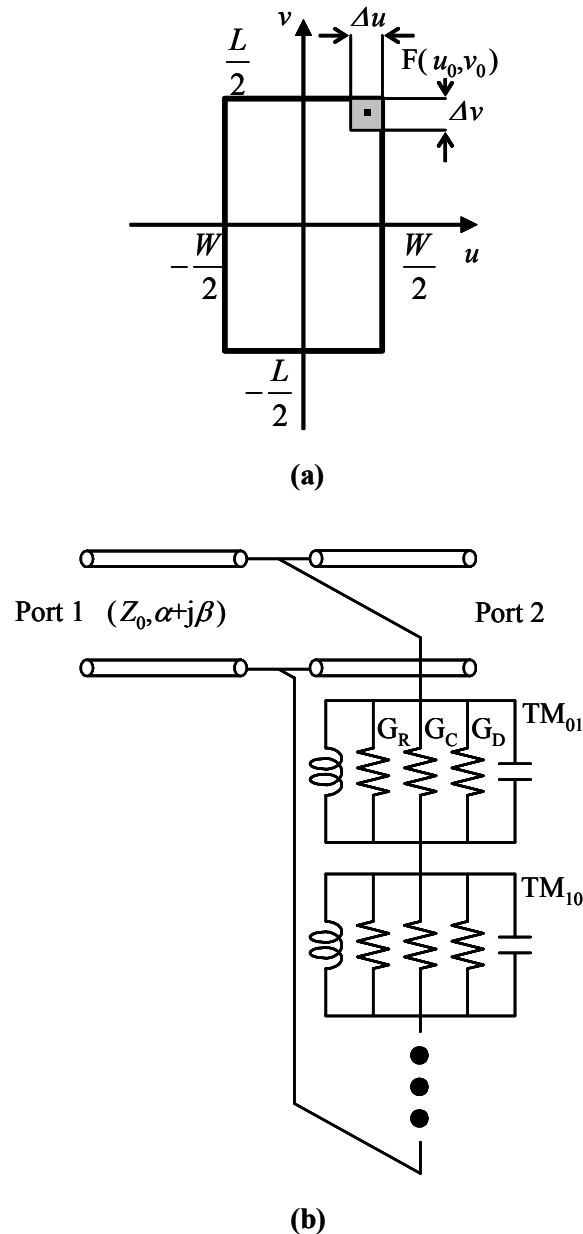


Fig. 3.2. Calculation model of a radiating element and its equivalent circuit connected to a feed line for calculation of coupling coefficients of the radiating element. (a) Calculation model of a radiating element and (b) equivalent circuit of the radiating element connected to a feed line.

loss as well as radiation power are considered by G_C , G_D , and G_R in the equivalent circuit. Impedance Z_{IN} of the cavity at the feed point F is given with the summation of impedance Z_{mn} for TM_{mn} modes.

$$Z_{IN} = \sum Z_{mn} = \frac{\frac{1}{2} V_{mn_F} V_{mn_F}^*}{P_{mn_R} + P_{mn_C} + P_{mn_D} + j2\omega(W_{mn_E} - W_{mn_M})} \quad (3.1)$$

where V_{mn_F} , P_{mn_R} , P_{mn_C} , P_{mn_D} , W_{mn_E} and W_{mn_M} denote voltage at the feed point F , radiation power, conductor loss, dielectric loss, electric energy, and magnetic energy of TM_{mn} mode. Equation (3.1) was derived, referring the literature [3-5], and the details are presented in Appendix 3.A. Conductivity 5.8×10^{-7} S/m of copper is used for calculation of conductor loss P_{mn_C} . S parameters of the equivalent circuit at the connection of the radiating element are written as

$$S_{11} = \frac{-\frac{Z_0}{Z_{IN}}}{2 + \frac{Z_0}{Z_{IN}}} \quad (3.2)$$

$$S_{21} = \frac{2}{2 + \frac{Z_0}{Z_{IN}}} \quad (3.3)$$

Thus coupling coefficient K_E of the radiating element from the feed line is given by

$$K_E = 1 - |S_{11}|^2 - |S_{21}|^2 \quad (3.4)$$

The coupling coefficient K_E includes radiation power, conductor loss and dielectric loss for all TM_{mn} modes excited in the radiating element. TM_{01} and TM_{10} modes, which correspond to co- and cross-polarizations, respectively, are focused and analyzed here since coupling coefficients of higher order modes are much smaller than that of TM_{01} mode and relative value between TM_{01} and TM_{10} is important. Figure 3.3 shows calculated coupling coefficients with variation of the width W of the radiating element. Vertical axis represents coupling coefficient and horizontal axis represents the width W normalized by the length L .

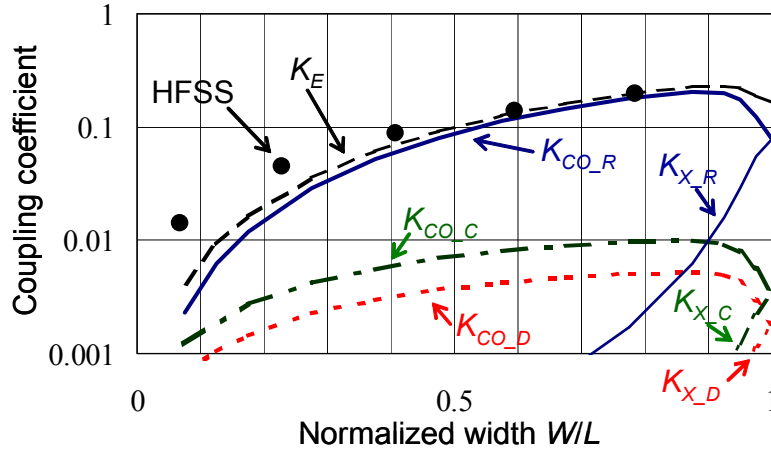


Fig. 3.3. Calculated coupling coefficients of radiation power K_{CO_R} and K_{X_R} , conductor loss K_{CO_C} and K_{X_C} , and dielectric loss K_{CO_D} , and K_{X_D} of both co- and cross-polarization modes with variation of the width W normalized by the length L . The total coupling coefficient K_E is presented as well as simulated results by HFSS.

Each coupling coefficient is separately calculated using the equivalent circuit in Figure 3.2 and the basic circuit theory. Subscripts co and x denote co- and cross-polarizations whilst subscripts R, C and D denote radiation power, conductor loss and dielectric loss, respectively. The coupling coefficient K_{CO_R} corresponding to radiation power for co-polarization increases from 0.01 to 0.20 as the width W becomes wider. The coupling coefficient K_{CO_R} becomes the maximum value of 0.20 at the width W of $0.90 L$. The coupling coefficient K_{CO_R} decreases as the width W gets further wider than $0.90 L$. On the other hand, the coupling coefficient K_{X_R} keeps small value of less than one hundredth of the coupling coefficient K_{CO_R} when the width W is narrower than $0.8 L$ and still keeps less than one twentieth at $0.9 L$. However the coupling coefficient K_{CO_R} increases steeply when the width W gets wider than $0.90 L$. The total coupling coefficient K_E is also presented for comparison with simulated results by HFSS using the finite element method. The total coupling coefficient K_E is almost

the same as the simulated results by HFSS.

In case that Taylor distribution with -17dB sidelobe level is set in the linear array antenna with 37 radiating elements, the coupling coefficient K_{CO_R} of 33 radiating elements in those of 36 radiating elements excluding the matching element becomes within available range from 0.01 to 0.20. Sidelobe level of -17 dB in the linear array antenna can be kept by compensation of each coupling coefficient of the 33 radiating elements since the effect of errors by the coupling coefficients of the other 3 radiating elements near the matching element is small when the coefficients are set to 0.20.

Another characteristic of the radiating element is also important for the design of the linear array antenna. Figure 3.4 shows the simulated transmission phase $\angle S_{21}$ of the microstrip line having the radiating element shown in Figure 3.2 (b) with variation of the width W . The transmission phase $\angle S_{21}$ is relative value to the microstrip line without the radiating element. The transmission phase $\angle S_{21}$ simulated by HFSS increases from 3 degrees to 21 degrees as the width W becomes wider from $0.07L$ to $0.90L$.

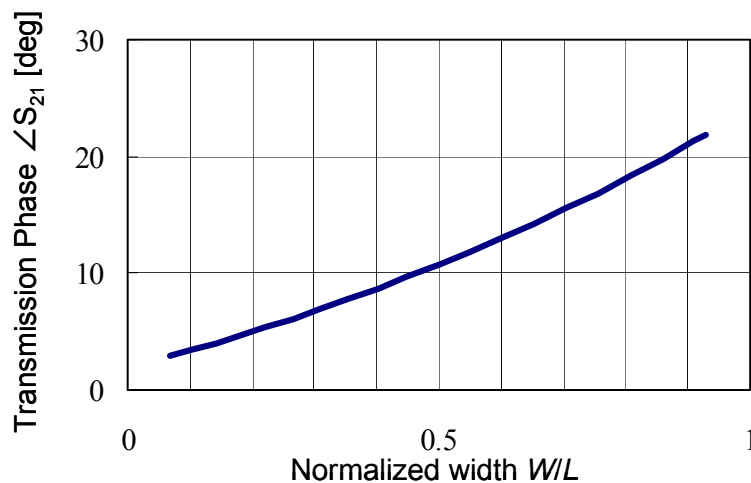


Fig. 3.4. Simulated transmission phase $\angle S_{21}$ of the microstrip line having the radiating element with variation of the width W normalized by the length L .

3.3.2 Feed line loss of linear array antenna

The design of linear array is next presented. In order to set desired amplitude distribution accurately, the feed line loss should be taken into account in the design. The design of a linear array antenna taking feed line loss into account is presented here and feed line loss is estimated.

Figure 3.5 shows the equivalent circuit of the linear array antenna for estimation of feed line loss. The radiating element which is the nearest to the source is numbered with #1 and the terminated radiating element is numbered with # N_y . The power $P_E(i)$ coupling to the i th radiating element includes radiation power, conductor loss and dielectric loss. Each spacing between the radiating elements is assumed to be the averaged value of $d_y = 0.403 \lambda_0$ although the spacing is actually adjusted because transmission phase is changed with variation of the width W . Attenuation constant of electromagnetic field for the loss of a microstrip line is expressed by α ($\alpha > 0$). The transmission power is attenuated exponentially with -2α as

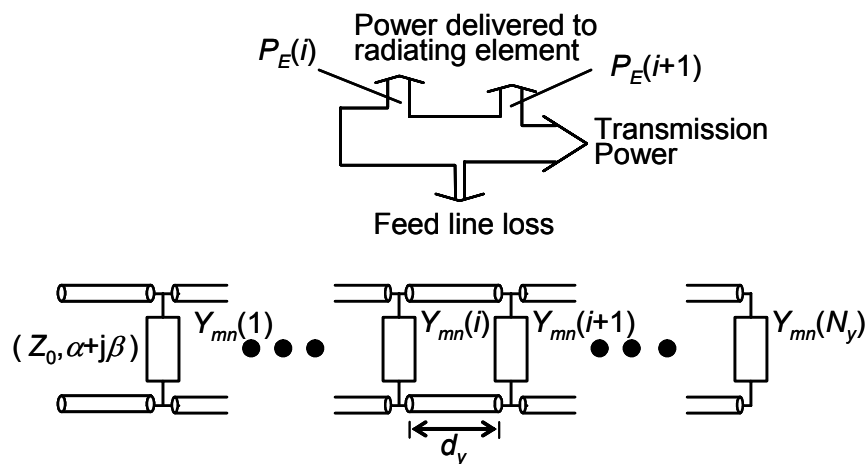


Fig. 3.5. Equivalent circuit of a linear array antenna for estimation of feed line loss.

the input power is transmitted toward the terminated element. The admittance $Y_{mn}(i)$ and the coupling coefficient $K_E(i)$ at the i th radiating element are sequentially determined from the terminated radiating element toward the source so as to set desired amplitude distribution in case that the terminated radiating element is matched to the feed line. The reflection from each radiating element is canceled out at the input port by tilting the main beam in the linear array antenna. Assuming that the over all reflection is small at the input port, the coupling coefficient $K_E(i)$ of the i th radiating element is given by

$$K_E(i) = \frac{P_E(i)}{P_E(i) + \sum_{j=i+1}^N P_E(j) e^{(2\alpha(j-i)d_y)}} \quad (3.5)$$

where the power $P_E(i)$ coupling to the i th radiating element is written with radiation power $P_{CO_R}(i)$ for co-polarization and losses $P_{EL}(i)$ including conductor loss, dielectric loss and radiation power for cross-polarization.

$$P_E(i) = P_{CO_R}(i) + P_{EL}(i) \quad (3.6)$$

The total loss P_{TL} of the feed line is derived from the total input power P_{TIN} at the source and the total power P_{TE} delivered to all radiating elements.

$$\begin{aligned} P_{TL} &= P_{TIN} - P_{TE} \\ &= \sum_{i=1}^N P_E(i) e^{(2\alpha(i-1)d_y)} - \sum_{i=1}^N P_E(i) \\ &= \sum_{i=1}^N P_E(i) (e^{(2\alpha(i-1)d_y)} - 1) \end{aligned} \quad (3.7)$$

Figure 3.6 shows transmission coefficient of the microstrip line measured by LRL calibration method. Vertical axis represents transmission coefficient per unit length and horizontal axis represents frequency from 66.5 GHz to 86.5 GHz. The measured loss was 0.03 dB/mm at 76.5 GHz. Time gate function was adopted to remove the unwanted reflection wave for high accuracy in the measurement.

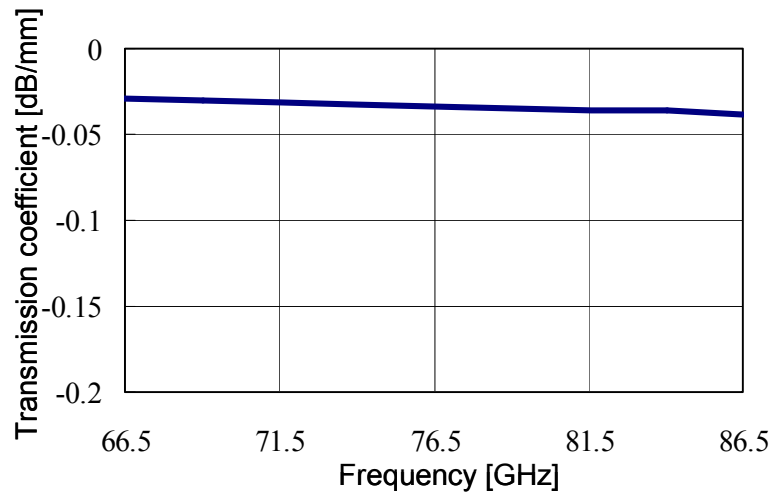


Fig. 3.6. Measured transmission coefficient of the microstrip line.

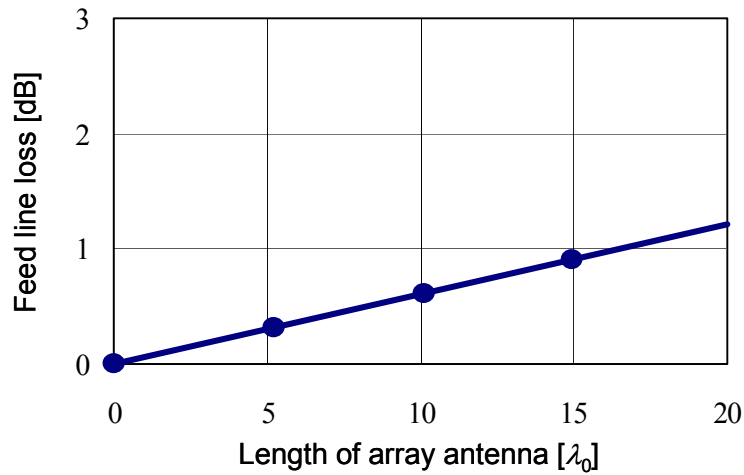


Fig. 3.7. Estimated feed line loss with variation of the length of the linear array antenna.

Feed line loss with variation of the length of the linear microstrip array antenna is estimated in Figure 3.7. The length of the array antenna is defined by the product of element number N_y and element spacing d_y . Amplitude distribution of each length of the array

antenna is set Taylor distribution with -17dB sidelobe level. Vertical axis represents feed line loss and horizontal axis represents the length of the array antenna. Feed line loss increases as the length of the array antenna becomes longer. The feed line loss of the array antenna is smaller than that of the microstrip line itself having the same length because the transmitted power is gradually radiated by radiating elements as well as is attenuated due to the loss of the microstrip line. The estimated feed line loss becomes 0.9 dB when the length of the array antenna is $15\lambda_0$.

The excited power distribution of the linear array antenna is shown in Figure 3.8. Vertical axis represents the excited power P_{CO_R} for co-polarization and horizontal axis represents the radiating element number. The summation of the excited power P_{CO_R} of all radiating elements is the ratio of the total radiation power to the total input power. In case that the feed line loss is taken into account in the design, the excited power distribution expressed by a circle is set nearly as Taylor distribution with -17 dB sidelobe level expressed

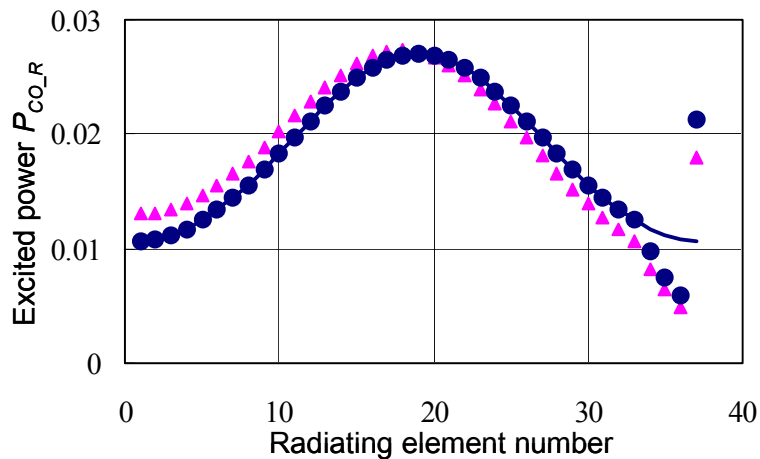


Fig. 3.8. Excited power distribution of the linear array antenna in cases that the feed line loss is considered and that it is not considered. (—: Taylor, ●: Feed line loss is considered, ▲: Feed line loss is not considered)

by a solid line. The effect of errors from Taylor distribution is small and sidelobe level of -17dB is kept as mentioned at the description of Figure 3.3. On the other hand, the coupling coefficients are specified to different values in case that the feed line loss is not considered in the design. The excited power distribution calculated by the specified coupling coefficients is also presented by a triangular for comparison. The excited power distribution is asymmetrical since the feed line loss actually exists.

Dimensions of radiating elements and their spacing in the linear array antenna are presented in Figure 3.9. The width W of the radiating element controlling the coupling coefficient K_{CO_R} becomes wider as the radiating element number increases. The length L of the radiating element adjusting a resonant length gets slightly shorter and the spacing d_y between $\#i\text{th}$ and $\#(i+1)$ adjusting the transmission phase gets slightly longer with the increase of the radiating element number.

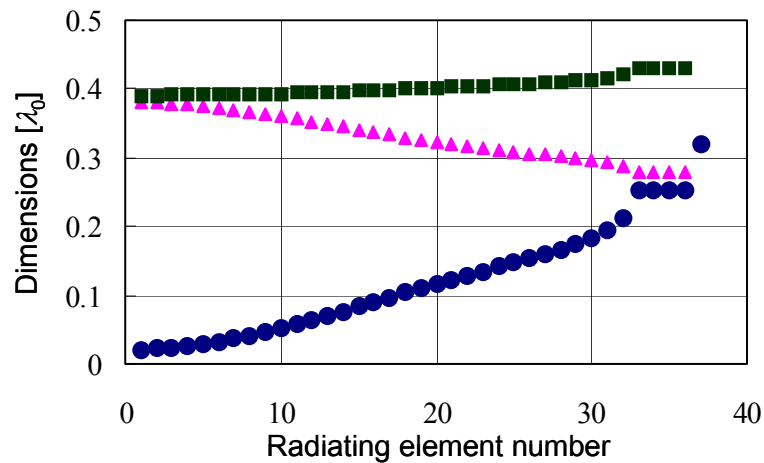


Fig. 3.9. Dimensions of radiating elements and their spacing in the linear array antenna. (●: Width W , ▲: Length L , ■: Spacing d_y)

3.4. Developed antennas

Performance of two types of developed antennas is described. One is a fan beam subarray antenna for electrical scanning radars, which is presented in Part 3.4.1. The other is a pencil beam array antenna for mechanical scanning radars, which is presented in Part 3.4.2.

3.4.1. Fan beam subarray for electrical scanning radars

Figure 3.10 shows a photograph of the fan beam subarray antenna, which is one of subarrays arranged in the azimuth plane for electrical scanning radars [3-6]. The antenna is composed of 2 linear arrays having 37 radiating elements.

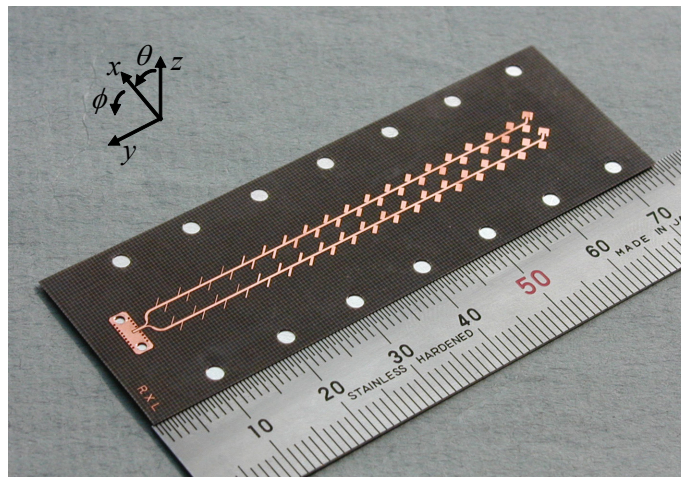
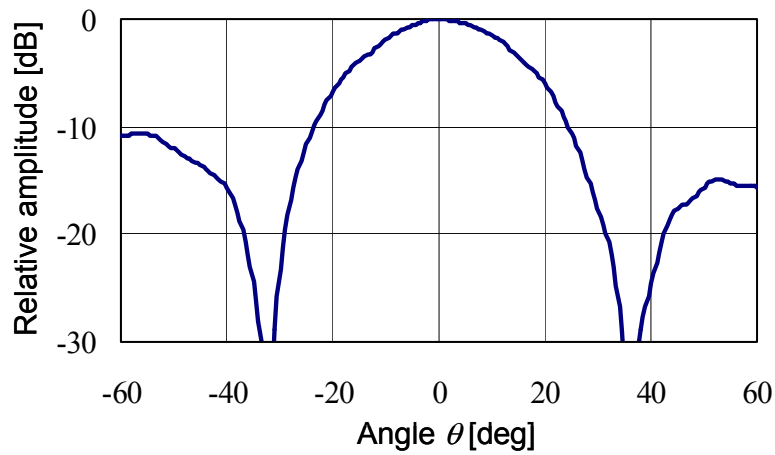


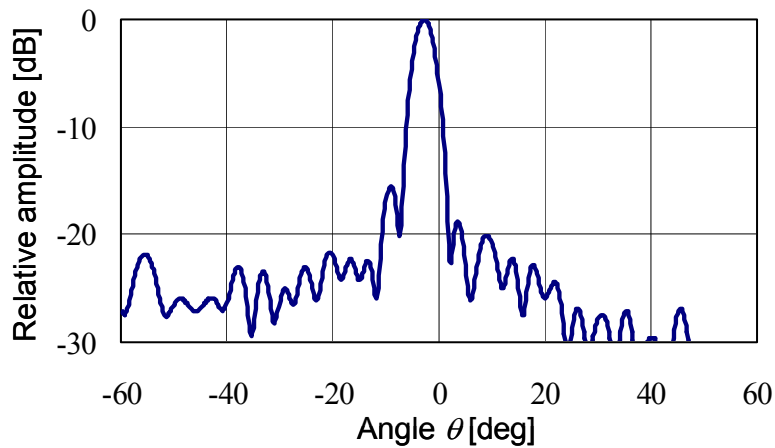
Fig. 3.10. Photograph of the fan beam microstrip subarray antenna for electrical scanning radars.

Measured radiation patterns in both the xz plane and the yz plane of the fan beam subarray antenna at 76.5 GHz are shown in Figure 3.11 (a) and (b), respectively. As shown in Figure 3.11 (a), the radiation pattern is almost symmetrical in the xz plane. Half power beam width and sidelobe level are 26.3 degrees and -10.7 dB, respectively. On the other hand, half

power beam width is 4.0 degrees and sidelobe level is suppressed to less than -15.4 dB in the yz plane in Figure 3.11 (b). Main beam is tilted to -2.8 degrees in the y direction to suppress the over all reflection at the input port. The main beam is scanned about 1.6 degrees when frequency is varied within 1 GHz. Since frequency bandwidth utilized for automotive radars



(a)



(b)

Fig. 3.11. Measured radiation patterns of the fan beam subarray antenna for electrical scanning radars at 76.5 GHz. (a) zx -plane and (b) yz -plane.

is 1 GHz, the main beam is scanned within ± 0.8 degrees. In this case, gain reduction at the direction of 2.8 degrees in the yz plane is 0.5 dB, which is small effect for performance of automotive radar systems.

Figure 3.12 shows measured gain and aperture efficiency of the fan beam subarray antenna. Vertical axis represents measured gain and horizontal axis represents frequency from 74.5 GHz to 78.5 GHz. Peak gain at each frequency and aperture efficiency are represented by a solid line and a dotted line, respectively. The gain reduction caused by beam scanning is not considered in Figure 3.12. Aperture efficiency η is defined as the ratio of the measured gain G_M to the aperture gain G_A and written as

$$\eta = \frac{G_M}{G_A} = \frac{G_M}{\frac{4\pi A}{\lambda_0^2}} = \frac{G_M}{\frac{4\pi N_x d_x N_y d_y}{\lambda_0^2}} \quad (3.8)$$

where A is an aperture area having radiating elements and is expressed by the product of numbers N_x and N_y of radiating elements, and spacing d_x and d_y of radiating elements in the x and the y directions, respectively. The aperture area A of the fan beam subarray antenna is

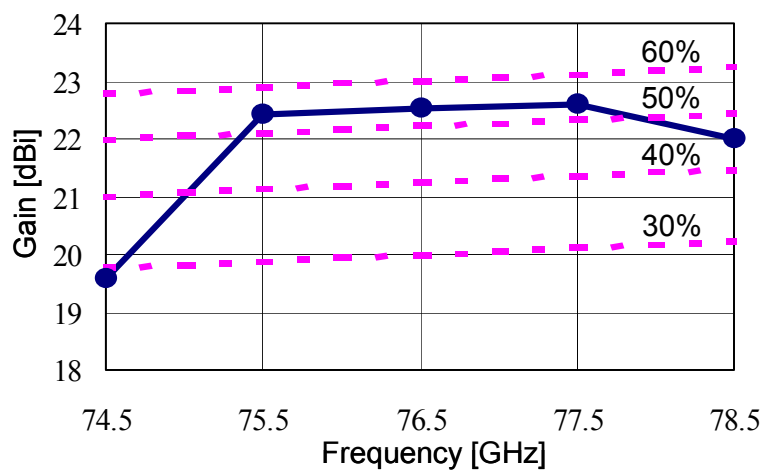


Fig. 3.12. Measured gain and aperture efficiency of the fan beam subarray antenna for electrical scanning radars.

$1.78 \lambda_0 \times 14.91 \lambda_0$. It can be seen from Figure 3.12 that aperture efficiency and gain are higher than 53 % and 22.4 dBi, respectively, in the frequency band from 75.5 GHz to 77.5 GHz, which are high enough for the frequency band for automotive radars. Aperture efficiency and gain at 76.5 GHz are 53 % and 22.5 dBi, respectively. Loss of the microstrip line to waveguide transition is not included in the measured gain.

Measured reflection of the fan beam subarray antenna at the input port is shown in Figure 3.13. The reflection at the input port is -18.7 dB at 76.5 GHz and bandwidth of reflection below -10 dB is 2.98 GHz.

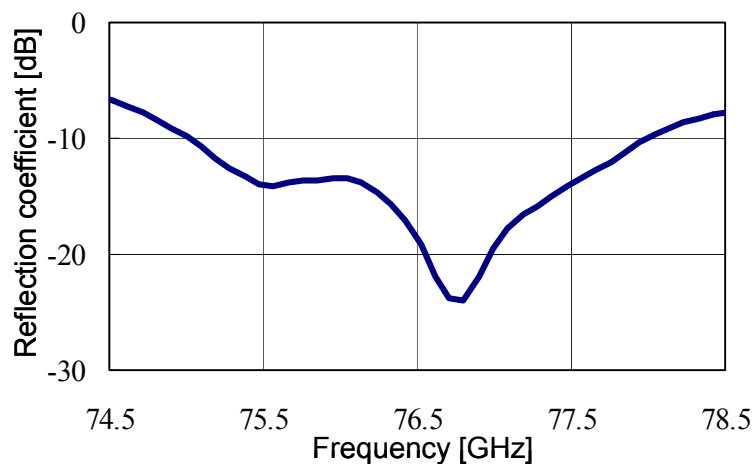


Fig. 3.13. Measured reflection coefficient of the fan beam subarray antenna for electrical scanning radars.

Losses of the fan beam subarray antenna are analyzed in Table 3.1. The losses estimated in the design include feed line losses, losses in the radiating element and losses of directive gain. Losses of a straight feed line and a T-junction for dividing power to the two linear arrays are estimated 0.9 dB shown in Figure 3.7 and 0.3 dB by HFSS, respectively.

Table 3.1. Analysis of losses of the fan beam subarray antenna for electrical scanning radars. Measured aperture efficiency is presented in () as well as estimates.

Loss factors	Feed line losses	Straight feed line	0.9dB
		Divider, Bend	0.3dB
	Losses in radiating element	Conductor loss	0.5dB
		Dielectric loss	0.3dB
	Losses of directive gain	Directive gain G_{D_U} /Aperture gain G_A	0.4dB
		Taylor distribution G_{D_T}/G_{D_U}	0.1dB
Aperture efficiency			56% (53%)

Conductor loss and dielectric loss in the radiating elements are estimated 0.5 dB and 0.3 dB, respectively, which are averaged values of conductor losses and dielectric losses of the all radiating elements. Conductor loss and dielectric loss of each radiating element are estimated from Figure 3.3. As losses of the directive gain, the ratio of the directive gain G_{D_U} in case of uniform amplitude distribution to the aperture gain G_A is estimated 0.4 dB. The ratio of the directive gain G_{D_T} in case of Taylor amplitude distribution with -17 dB sidelobe level to the directive gain G_{D_U} in case of the uniform amplitude distribution is also estimated 0.1 dB. The estimation of directive gain was carried out with the cavity model and array factors. The dimensions L and W of each radiating element and the spacing d_y between radiating elements in the y direction are assumed to be the same values and are set the average values of the developed subarray antenna such as $L = 0.321 \lambda_0$, $W = 0.11 \lambda_0$ and $d_y = 0.403 \lambda_0$, respectively. The spacing d_x in the x direction is set to $0.89 \lambda_0$. Mutual coupling between

radiating elements is not taken into account. The aperture efficiency is estimated to 56 % from the analysis of the loss factors. On the other hand, measured aperture efficiency is 53 %, which is close to the estimated value. The reduction of aperture efficiency due to the reflection loss at the input port is 1 % since the measured reflection is -18.7 dB shown in Figure 3.13. The validity of the analysis is confirmed by the estimated and measured values.

3.4.2 Pencil beam array antenna for mechanical scanning radars

A feed circuit between a feed point and some linear arrays becomes important in terms of aperture efficiency, as an aperture area gets larger. We propose the two-stage series feed

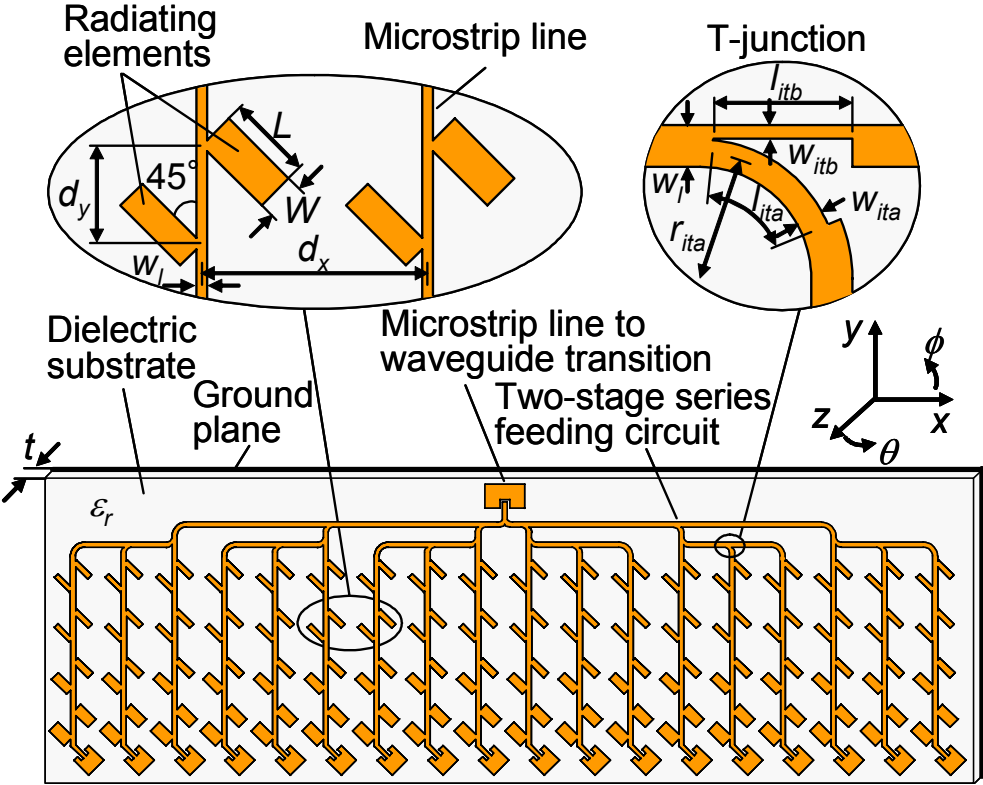


Fig. 3.14. Configuration of the pencil beam microstrip array antenna having the proposed two-stage series feed circuit for mechanical scanning radars.

circuit as well as the microstrip linear array antenna shown in Figure 3.14. The proposed two-stage series feed circuit is the series feed circuit consisting of some further series feed circuits. Thus the proposed feed circuit has both advantages of lower feed line loss in the series feed circuit and setting aperture distribution with small power dividing ratio of T-junction in the parallel feed circuit. The one output port is rounded and the other output port is straight at the T-junction. The radius r_{ita} is selected to a relatively large value of $0.17 \lambda_0$ to minimize the degradation caused by the discontinuity. The widths w_{ita} and w_{itb} control characteristic impedance of impedance transformers whilst the lengths of l_{ita} and l_{itb} are a quarter guided wavelength. The width of the microstrip line is varied from $0.026 \lambda_0$ to $0.0765 \lambda_0$ in the proposed circuit.

Figure 3.15 shows estimated feed line loss of the proposed feed circuit as well as conventional series and parallel feed circuits with variation of the length of the feed circuits, which are represented by a circle, a triangular and a rectangular, respectively. The length of

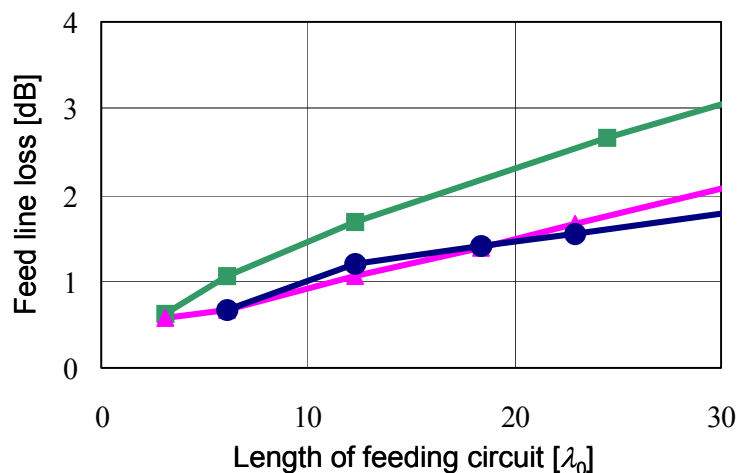


Fig. 3.15. Feed line loss of the feed circuit with variation of its length. (—●—: Proposed, —▲—: Series, —■—: Parallel)

the feed circuit is defined by the product of the number N_X of linear arrays and their spacing d_X in the x direction. Loss of the microstrip line is taken into account using attenuation constant α ($\alpha > 0$) as the same concept as presented in section 3.3. Since the two-stage series feed circuit has discontinuities of T-junctions and bends, the following equation is introduced in the estimation.

$$P_{IN} = \sum P_{OUT} + P_L \quad (3.9)$$

where P_{IN} , P_{OUT} and P_L are input power to the discontinuity, output power from the discontinuity and loss caused by radiation and surface wave at the discontinuity. Output from the discontinuity has one port for the bend or two ports for the T-junction. In this estimation, P_L is set to 0.1 dB at the T-junction and the bend referring to the simulated results by HFSS. Amplitude distribution of each length of the feed circuit is set Taylor distribution with -17 dB sidelobe level. It can be seen from Figure 3.15 that loss of the proposed feed circuit is less than that of the parallel feed circuit and has almost the same value as the series feed circuit. Feed line loss of the proposed feed circuit is estimated 1.6 dB when the length of the feed circuit is $23 \lambda_0$, which corresponds to the horizontal length of the pencil beam array antenna.

In the above estimation, power dividing ratio of each T-junction is also determined. The power dividing ratio of the T-junction is defined as $n:1$ in case that the input power is divided into $n/(n+1)$ at the one output port and $1/(n+1)$ at the other output port. Figure 3.16 shows the maximum power dividing ratio of the T-junction with variation of the length of the feed circuit. A circle, a triangular and a rectangular denote the maximum power dividing ratio of the T-junctions used in the proposed, the series and the parallel feed circuits. The number of linear arrays connected to a subgroup of the proposed circuit does not exceed 4 in Figure 3.16. The series feed circuit needs large power dividing ratio, as the feed circuit gets longer. In case of the length of $23 \lambda_0$, the maximum power dividing ratio needs 12:1, thus it cannot be

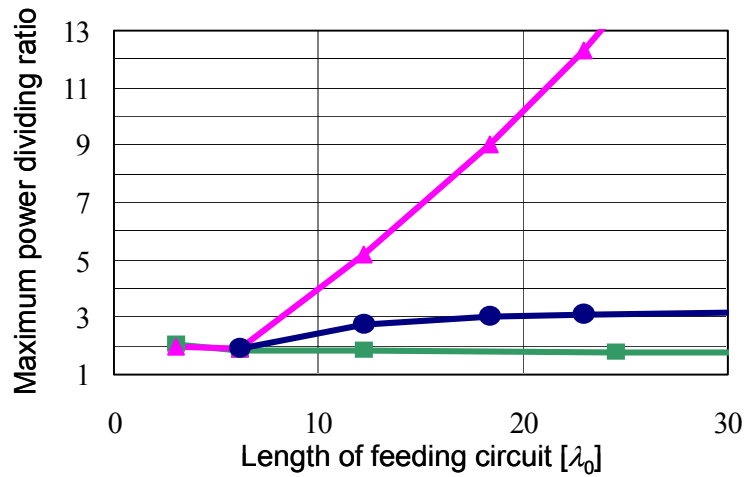


Fig. 3.16. Required maximum power dividing ratio of T-junctions in the feed circuit with variation of the length of the feed circuit. (—●—: Proposed, —▲—: Series, —■—: Parallel)

fabricated due to the manufacturing limitation. On the other hand, the proposed and the parallel feed circuits do not need large power dividing ratio. The proposed feed circuit needs just 3:1 and can be etched even when the length of the feed circuit is relatively long of $23 \lambda_0$.

Figure 3.17 shows a photograph of the pencil beam array antenna having the proposed two-stage series feed circuit for mechanical scanning radars. The antenna is composed of 30 linear arrays having 37 radiating elements. The amplitude distributions in both the x and y directions are set Taylor distribution with -17 dB sidelobe level.

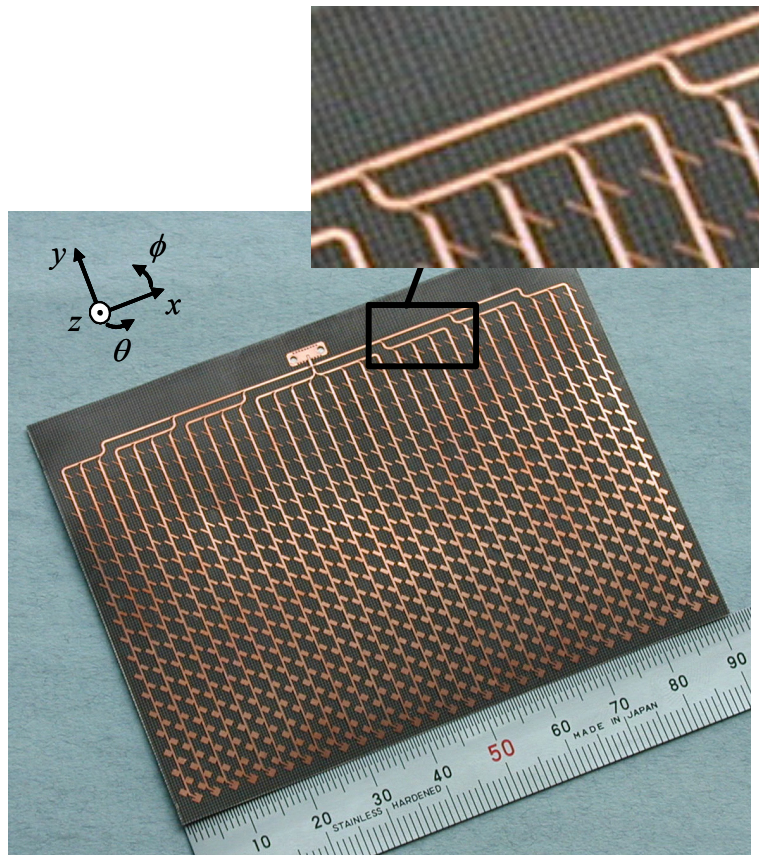
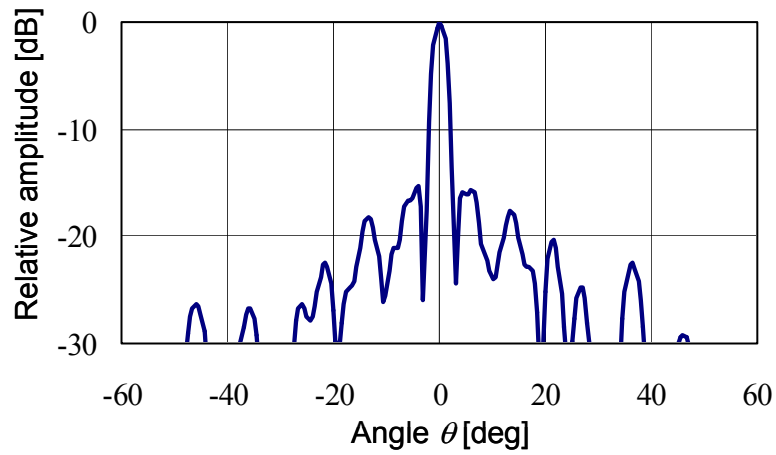


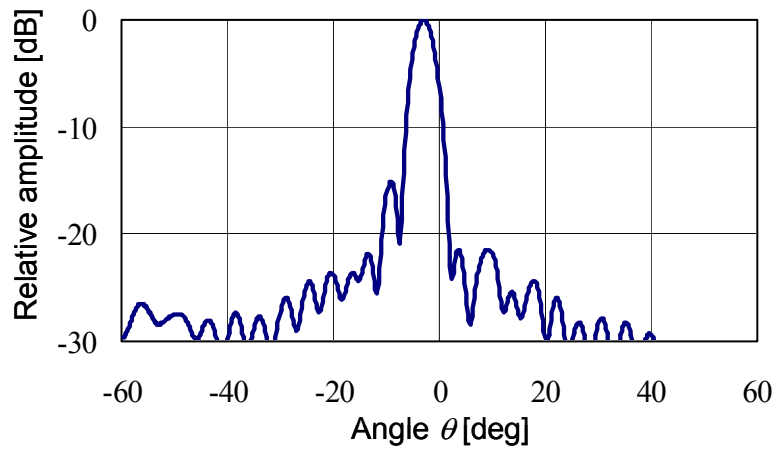
Fig. 3.17. Photograph of the pencil beam microstrip array antenna having the proposed two-stage series feeding circuit for mechanical scanning radars.

Measured radiation patterns in the zx and yz planes of the pencil beam array antenna at 76.5 GHz are shown in Figure 3.18 (a), (b), respectively. Main beam is tilted to -3.0 degrees in the yz plane to suppress the over all reflection at the input port. Beamwidth is 2.5 degrees in the zx plane and 4.1 degrees in the yz planes, respectively. Sidelobe levels in both planes are below -15 dB, which are -15.3 dB in the zx plane and -15.0 dB in the yz plane, respectively. During the change of frequency from 76 GHz to 77 GHz, the gain reduction at

the direction of 3.0 degrees in the yz plane is 0.5 dB due to beam scanning, as discussed in Part 3.4.1.



(a)



(b)

Fig. 3.18. Measured radiation patterns of the pencil beam array antenna for mechanical scanning radars at 76.5GHz. (a) zx -plane and (b) yz -plane.

Measured reflection of the pencil beam array antenna at the input port is shown in Figure 3.19. The reflection at the input port is -17.3 dB at 76.5 GHz and bandwidth of reflection below -10 dB is 1.44 GHz.

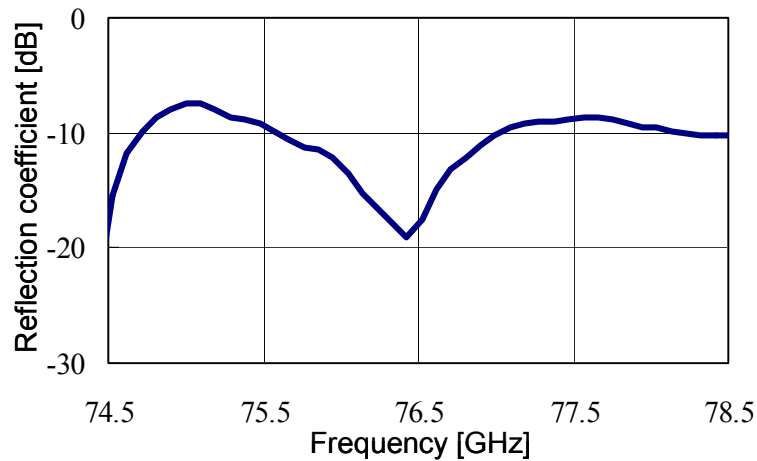


Fig. 3.19. Measured reflection coefficient of the pencil beam array antenna for mechanical scanning radars.

Figure 3.20 shows the measured aperture efficiency with variation of the measured gain. Vertical axis represents the measured aperture efficiency and horizontal one represents the measured gain. A circle denotes the measured aperture efficiency of the developed antennas, which are 2, 3, 4, 6 and 30 linear arrays having 37 radiating elements. An aperture efficiency of 39 % with gain of 32.2 dBi is obtained at 76.5 GHz for the pencil beam antenna composed of 30 linear arrays. The aperture area A of the pencil beam array antenna is $22.96 \lambda_0 \times 14.91 \lambda_0$. The measured aperture efficiency is higher than 50 % when the measured gain is 20 dBi. The measured aperture efficiency still keeps about 40 % at the measured gain of 30 dBi although the measured aperture efficiency gradually decreases as the number of linear

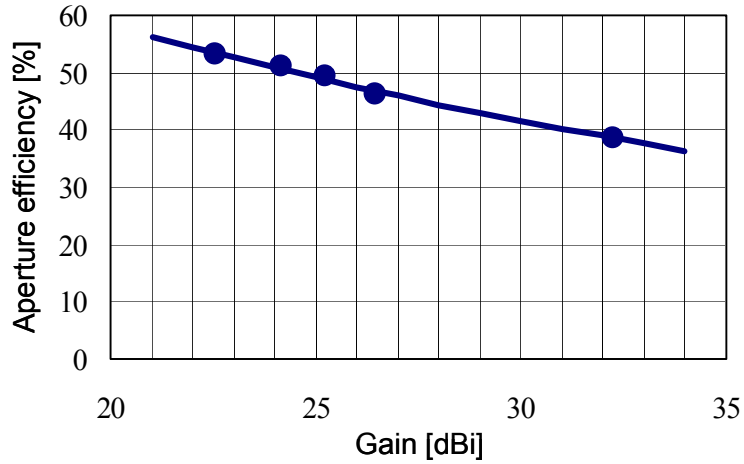


Fig. 3.20. Measured aperture efficiency versus gain of microstrip array antennas for automotive radars at 76.5GHz.

arrays increases.

Losses of the pencil beam array antenna are also analyzed in Table 3.2. The losses estimated in the design include feed line losses, losses in the radiating element and losses of directive gain. Losses of the proposed 2-stage series feed circuit for dividing power in the x direction and a straight feed line in the y direction are estimated to be 1.6 dB shown in Figure 3.15 and 0.9 dB shown in Figure 3.7, respectively. Conductor loss and dielectric loss in the radiating elements are the same values of 0.5 dB and 0.3 dB in Table 3.1, respectively. As losses of the directive gain, the ratios of the directive gain G_{D_U} in case of uniform amplitude distribution to the aperture gain G_A , and the directive gain G_{D_T} in case of Taylor amplitude distribution with -17 dB sidelobe level to the directive gain G_{D_U} in case of the uniform amplitude distribution are estimated 0.1dB and 0.2dB, respectively. The estimated and measured values of aperture efficiency are 44 %, and 39 %, respectively. The reduction of aperture efficiency caused by the reflection loss at the input port is 1 % since the measured reflection is -17.3 dB shown in Figure 3.19. The analysis in Table 3.2 is also validated in

comparison with the estimated and measured values.

Table 3.2. Analysis of losses of the pencil beam array antenna for mechanical scanning radars. Measured aperture efficiency is presented in () as well as estimates.

Loss factors	Feed line losses	Straight feed line	0.9dB
		Two-stage series feeding circuit	1.6dB
	Losses in radiating element	Conductor loss	0.5dB
		Dielectric loss	0.3dB
	Losses of directive gain	Directive gain G_{D_U} /Aperture gain G_A	0.1dB
		Taylor distribution G_{D_T}/G_{D_U}	0.2dB
Aperture efficiency			44% (39%)

3.5. Conclusions

A high efficient microstrip array antenna having 45-degree inclined linear polarization has been proposed for automotive radars. The rectangular radiating elements inclined at 45 degrees to the straight microstrip line are directly connected to it at their corners in the proposed array antenna. The radiating element was shown to have a feature that the radiation conductance for 45-degree inclined linear polarization is controlled widely enough to set Taylor amplitude distribution keeping excited mode for cross-polarization negligibly small. Feed line loss of the linear array antenna having $15 \lambda_0$ was estimated 0.9 dB in the design taking the loss of the microstrip line into account. Two types of array antennas, for

electrical and mechanical scanning radars, were developed. The fan beam subarray antenna having 2×37 elements for electrical scanning radars showed an aperture efficiency of 53 % with gain of 22.5 dBi at 76.5 GHz. For mechanical scanning radars, the two-stage series feed circuit has been also proposed for lower feed line loss and setting desired amplitude distribution. Loss of the proposed feed circuit was estimated 1.6 dB. The pencil beam array antenna with 30×37 radiating elements showed an aperture efficiency of 39 % with gain of 32.2 dBi. Aperture efficiency still keeps 40% in the proposed antenna when gain is 30 dBi.

A millimeter-wave antenna should be chosen to meet requirements of performance, cost, size and reliability for the systems. These results are very useful for engineers to choose a suitable antenna for millimeter-wave automotive radar systems. We believe from these results that the proposed microstrip array antenna having a feature of high aperture efficiency as well as low profile and ease of manufacture will be used not only for ACC system but also advanced radar systems such as Stop & Go ACC system and a collision avoidance system.

References

- [3-1] H. Iizuka, T. Watanabe, K. Sato, and K. Nishikawa, "Millimeter-wave microstrip array antenna for automotive radars," *IEICE Trans. Commun.*, vol.E86-B, no.9, pp.2728-2738, Sept. 2003.
- [3-2] H. Iizuka, T. Watanabe, K. Sato and K. Nishikawa, "Millimeter-wave microstrip array antenna for automotive radar systems", *ISAP2000*, pp.465-468. Fukuoka, Japan, Aug. 2000.
- [3-3] H. Iizuka, K. Sakakibara, T. Watanabe, K. Sato and K. Nishikawa, "Antennas for automotive millimeter-wave radar systems" *Proc. IEICE Gen. Conf. '01*, SB-1-7,

Kusatsu, Mar., 2001.

- [3-4] H. Iizuka, T. Watanabe, K. Sato and K. Nishikawa, “76GHz-band microstrip array antenna for automotive radar systems” *Proc. IEICE Soci. Conf. '00*, B-1-156, Nagoya, Sept., 2000.
- [3-5] K. Hirasawa and M. Haneishi, “*Analysis, design, and measurement of small and low-profile antennas*”, Artech house, 1992.
- [3-6] Y. Asano, “Millimeter-wave holographic radar for automotive applications,” *Microwave workshops and exhibition digest*, pp.157-162, Yokohama, Japan, Dec. 2000.

3.A Appendix

The process of derivation for voltage V_{mn_F} at the feed point F , electric energy W_{mn_E} , magnetic energy W_{mn_M} , conductor loss P_{mn_C} , dielectric loss P_{mn_D} and radiation power P_{mn_R} , which are used in the equation (1), is presented. Eigen-function for TM_{mn} mode is given by

$$\phi_{mn}(u, v) = \sqrt{\frac{\epsilon_m \epsilon_n}{WL}} \cos\left(\frac{m\pi}{W}u + \frac{m\pi}{2}\right) \cos\left(\frac{n\pi}{L}v + \frac{n\pi}{2}\right), \quad (3A-1)$$

$$\epsilon_m = \begin{cases} 1(m=0) \\ 2(m=1,2,\dots), \end{cases} \quad \epsilon_n = \begin{cases} 1(n=0) \\ 2(n=1,2,\dots). \end{cases}$$

Green's function is also given by

$$G(u, v|u_0, v_0) = j\omega\mu_0 \frac{\phi^*(u_0, v_0)\phi(u, v)}{k_{mn}^2 - k^2} \quad (3A-2)$$

where ω is angular frequency and μ_0 is permeability in free space. The values of k and k_{mn} are wave number in the cavity and eigen-value for TM_{mn} mode, respectively. Assuming that

current distribution $i(u_0, v_0)$ is constant I_0 in the area S_F of the feed point F , z component E_{mn_z} of electric field is manipulated to the equation (3A-3).

$$\begin{aligned}
E_{mn_z}(u, v) &= \iint_{S_F} G(u, v | u_0, v_0) i(u_0, v_0) dS \\
&= j\omega\mu_0 I_0 \frac{\phi^*(u_0, v_0)\phi(u, v)}{k_{mn}^2 - k^2} \frac{\sin\left(\frac{m\pi\Delta u}{2W}\right)}{\left(\frac{m\pi\Delta u}{2W}\right)} \frac{\sin\left(\frac{n\pi\Delta v}{2L}\right)}{\left(\frac{n\pi\Delta v}{2L}\right)}
\end{aligned} \tag{3A-3}$$

The dimensions $\Delta u \times \Delta v$ of the area S_F are set $w_l / \sqrt{2} \times w_l / \sqrt{2}$ in this calculation. The voltage V_{mn_F} of the feed point F is written as

$$\begin{aligned}
V_{mn_F}(u_0, v_0) &= \frac{1}{\Delta u \Delta v} \iint_{S_F} t E_{mn_z}(u, v) dS \\
&= j\omega\mu_0 t I_0 \frac{\phi^*(u_0, v_0)\phi(u_0, v_0)}{k_{mn}^2 - k^2} \left(\frac{\sin\left(\frac{m\pi\Delta u}{2W}\right)}{\left(\frac{m\pi\Delta u}{2W}\right)} \right)^2 \left(\frac{\sin\left(\frac{n\pi\Delta v}{2L}\right)}{\left(\frac{n\pi\Delta v}{2L}\right)} \right)^2
\end{aligned} \tag{3A-4}$$

Electric energy W_{mn_E} is given by integration of electric field E_{mn_z} in the volume v_0 of the cavity.

$$W_{mn_E} = \frac{\epsilon_0 \epsilon_r}{4} \iiint_{v_0} |E_{mn_z}|^2 dv \tag{3A-5}$$

where ϵ_0 is permittivity in free space. On the other hand, magnetic energy W_{mn_M} is given by integration of magnetic field H_{mn_u} and H_{mn_v} in the volume v_0 of the cavity.

$$\begin{aligned}
W_{mn_M} &= \frac{\mu_0}{4} \iiint_{v_0} \left(|H_{mn_u}|^2 + |H_{mn_v}|^2 \right) dv \\
&= \frac{\mu_0}{4} \iiint_{v_0} \left(\left| -\frac{1}{j\omega\mu_0} \frac{\partial E_{mn_z}}{\partial v} \right|^2 + \left| \frac{1}{j\omega\mu_0} \frac{\partial E_{mn_z}}{\partial u} \right|^2 \right) dv
\end{aligned} \tag{3A-6}$$

both u component H_{mn_u} and v component H_{mn_v} of magnetic field are expressed by z component E_{mn_z} of electric field in the equation (3A-6). Conductor loss P_{mn_C} is written

with magnetic energy W_{mn_M} .

$$P_{mn_C} = \frac{2W_{mn_M}}{t} \sqrt{\frac{2\omega}{\mu_0\sigma}} \quad (3A-7)$$

where σ is conductivity of copper 5.8×10^{-7} S/m. Dielectric loss P_{mn_D} is written with magnetic energy W_{mn_E} .

$$P_{mn_D} = 2W_{mn_E} \tan \delta \quad (3A-8)$$

Radiation power P_{mn_R} is given by integration in half spherical surface S_{HS} .

$$P_{mn_R} = \frac{1}{2\eta_0} \iint_{S_{HS}} \vec{E} \times \vec{H} \bullet \vec{n}_{S_{HS}} dS \quad (3A-9)$$

where η_0 is characteristic impedance in free space and $\vec{n}_{S_{HS}}$ is a normal unit vector to half spherical surface S_{HS} . \vec{E} and \vec{H} are electric and magnetic fields in far field region and are given with vector magnetic potential \vec{A}_M .

$$\vec{E} = -j\omega\eta_0 \vec{A}_M \times \vec{n}_{S_{HS}} \quad (3A-10)$$

$$\vec{H} = -j\omega \vec{A}_M \quad (3A-11)$$

The vector magnetic potential \vec{A}_M is given by integration of magnetic current \vec{M} on the surface S_M of magnetic wall of the cavity.

$$\vec{A}_M = \epsilon_0 \iint_{S_M} \vec{M} \frac{e^{-jkr}}{4\pi r} dS \quad (3A-12)$$

where r is distance from the magnetic current source to the view point. The magnetic current \vec{M} on the surface S_M is given by

$$\vec{M} = E_{mn_Z} \vec{i}_z \times \vec{n}_{S_M} \quad (3A-13)$$

where \vec{i}_z is z component of a unit vector and \vec{n}_{S_M} is a normal unit vector to the surface S_M .

Chapter 4. Millimeter-wave transition from waveguide to microstrip line

4.1 Introduction

A new type of microstrip line to waveguide transition [4-1], [4-2] is proposed in this chapter. The transition can be fabricated on a single layer dielectric substrate. The proposed transition has features of low loss characteristic, a simple structure and robustness for assembling errors. Impedance matching of the transition is achieved with ease and the method is presented. As a result of experiments, low transmission loss of 0.4 dB is realized at the design frequency of 76.5 GHz. Bandwidth of the transition is investigated by the finite element method and discussed. Quality factor Q is introduced in order to recognize the relation between the bandwidth and some parameters such as the dimensions of the waveguide, thickness of the dielectric substrate and relative dielectric constant. In addition, the effect of errors in relative position between the dielectric substrate and the waveguide is also investigated and assembling tolerance is discussed. In Section 4.2, a configuration of the proposed microstrip line to waveguide transition is described. Performance of the transition is presented and discussed in Section 4.3. This chapter is concluded in Section 4.4.

4.2. Proposal of microstrip line to waveguide transition

Figure 4.1 shows a configuration of the proposed microstrip line to waveguide transition. Conductor patterns on both surfaces of a dielectric substrate are separately illustrated in the Fig. 4.1. The conductor pattern with a notch (it is named a waveguide short pattern because of its function.) and the microstrip line located at the notch are printed on one side of the dielectric substrate. In addition that, a rectangular conductor pattern (it is named a matching element because of its function.) and a ground plane fixed to the waveguide cross section are

printed on another side of it. Some via holes are arranged around the waveguide short pattern to connect electrically to the ground plane. The proposed microstrip line to waveguide transition can be easily fabricated on a single layer dielectric substrate.

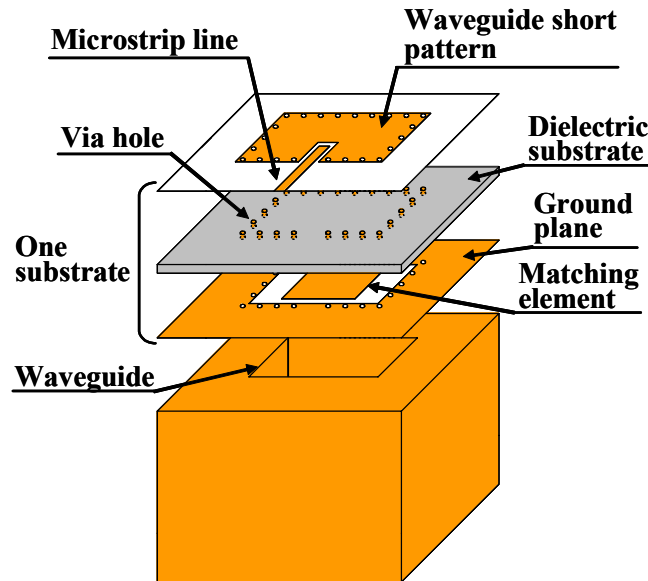


Fig. 4.1. Configuration of microstrip line to waveguide transition.

Parameters and coordinate systems of the transition are shown in Fig. 4.2. Parameters are defined as length L of the matching element, width W of the matching element, width w_l of the microstrip line, width g of the gap between the waveguide short pattern and the microstrip line, length ρ of the inserted microstrip line across the waveguide, thickness t of the dielectric substrate, relative dielectric constant ϵ_r , diameter ϕ of the via hole, spacing d between via holes, broad wall length a of the waveguide and narrow wall length b of the waveguide. Parameters of a calculation model are presented in Table 4.1. Numerical investigation is carried out by using the finite element method.

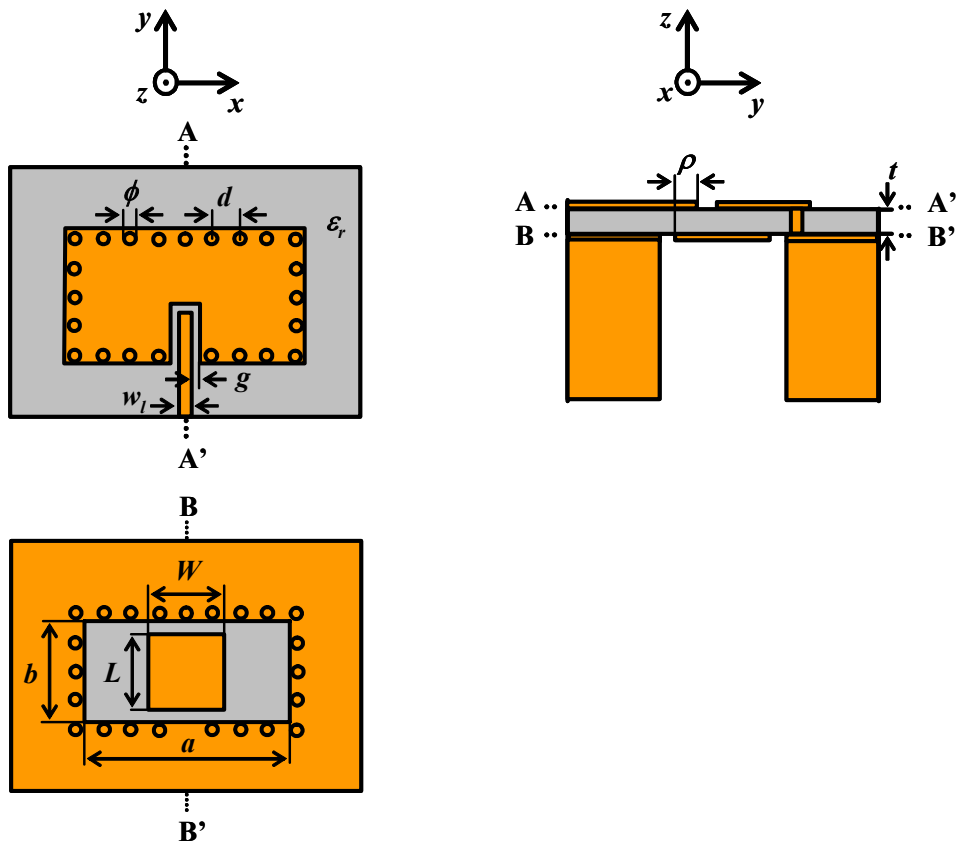


Fig. 4.2. Parameters and coordinate systems.

Table 4.1. Parameters of calculation model. (Parameters of fabricated transition are represented in ().)

Length L of matching element	1.085mm (1.12mm)
Width W of matching element	1.085mm (1.12mm)
Length ρ of inserted microstrip line	0.195mm (0.28mm)
Width w_l of microstrip line	0.27mm
Width g of gap	0.1mm
Thickness t of dielectric substrate	0.127mm
Relative dielectric constant ϵ_r	2.2
Broad wall length a of waveguide	3.1mm
Narrow wall length b of waveguide	1.55mm
Diameter ϕ of via hole	0.2mm
Spacing d between via holes	0.5mm

Figure 4.3 shows electric field distribution of each mode in yz plane. The modes of the microstrip line, the matching element and the waveguide are quasi TEM transmission mode, TM_{01} fundamental resonant mode and TE_{10} fundamental transmission mode, respectively. In the proposed transition, low transmission loss is realized by exchanging quasi TEM transmission mode and TE_{10} fundamental transmission mode with high efficiency utilizing TM_{01} fundamental resonant mode.

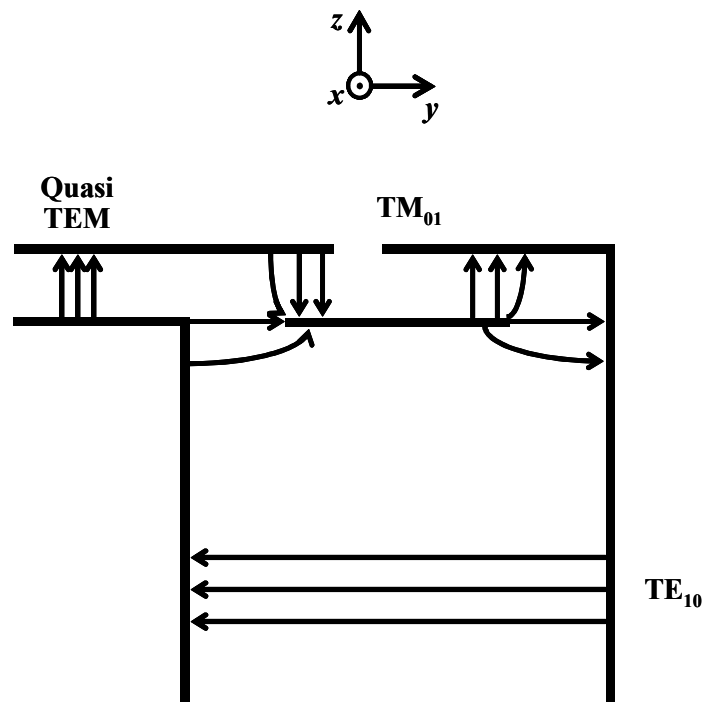


Fig. 4.3. Electric field distribution of each mode in yz plane.

Figure 4.4 shows calculated electric field intensity distribution in xy plane including BB'-line. The electric field intensity E is written as the equation (4.1) with E_x , E_y and E_z .

$$E = \sqrt{E_x^2 + E_y^2 + E_z^2} \quad (4.1)$$

where E_x , E_y and E_z are x , y and z components of electric field. The electric field intensity E

is normalized by its maximum value in the Fig. 4.4. It is observed that the matching element is resonated TM_{01} mode in which the length L of the matching element is a half resonant wavelength. In case of $z \rightarrow -\infty$, electric field intensity in the center of H plane of the waveguide becomes 0.1 of the scale in the Fig. 4.4. Shape of via holes is modified to be rectangular in order to save calculation time. In this configuration, impedance matching at the desired frequency can be achieved by controlling the length L of the matching element and the length ρ of the inserted microstrip line.

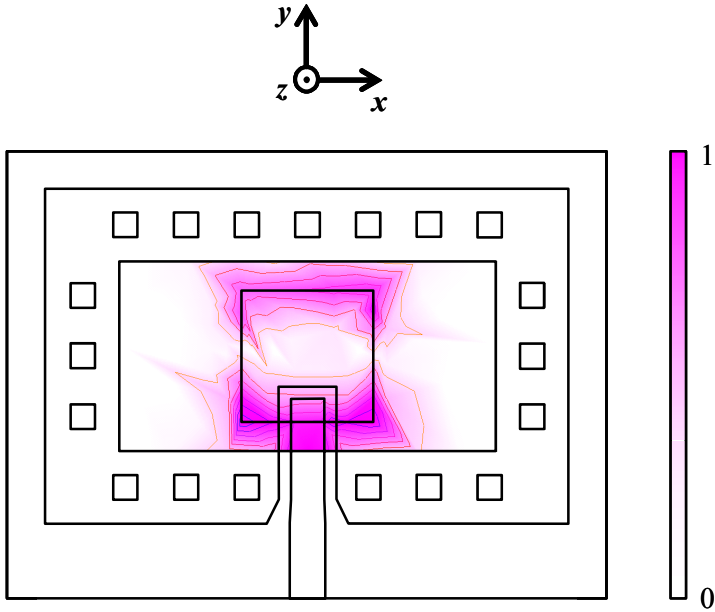


Fig. 4.4. Electric field intensity distribution in xy plane.

4.3. Performance

In this Section, performance of the microstrip line to waveguide transition is presented. Characteristics of the transition are numerically analyzed by using the finite element method at the design frequency of 76.5 GHz, which is the frequency for automotive radars.

Measured transmission characteristics of the fabricated transition are also presented with calculated ones and validity of the design is confirmed.

4.3.1 Impedance matching characteristics

Resonant frequency versus the length L of the matching element is shown in Fig. 4.5. Calculated result is represented by a solid line. Calculation is carried out in case that the length L of the matching element equals the width W of the matching element and that other parameters of the calculation model listed in the Table 4.1 except for the dimensions L and W of the matching element are used. As shown in the Fig. 4.5, the resonant frequency is controlled by the length L of the matching element and obtained to be 76.5 GHz when the length L of the matching element is 1.085 mm.

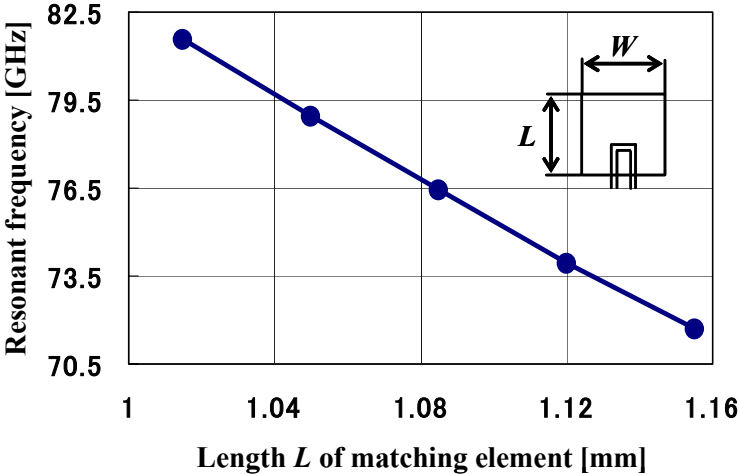


Fig. 4.5. Resonant frequency versus length L of matching element in case of $L = W$.

Figure 4.6 shows $VSWR$ versus the length ρ of the inserted microstrip line normalized by the length L of the matching element. Calculated result is represented by a solid line. Calculation is carried out in case that other parameters of the calculation model described in

the Table 4.1 except for the length ρ of the inserted microstrip line are used. It can be seen from the Fig. 4.6 that $VSWR$ is controlled by the length ρ of the inserted microstrip line and that impedance matching is obtained at two points where the length ρ of the inserted microstrip line is $0.18 L$ or $0.65 L$. Shorter length of $0.18 L$ is chosen as the length ρ of the inserted microstrip line in order to reduce degradation of resonant mode of the matching element and unwanted radiation in the backward direction (in $+z$ direction).

Existence of impedance matching in two conditions as a function of the inserted microstrip line length ρ indicates that coupling state between the microstrip line and the matching element varies in order of under-coupling, over-coupling and under-coupling as the length ρ of the inserted microstrip line becomes longer. Coupling state and coupling coefficient between them become over-coupling and maximum, respectively, when the end of the microstrip line is located near the center of the matching element. Therefore, the microstrip line and the matching element are coupled between the magnetic field excited at the end of the microstrip and the magnetic field of TM_{01} mode excited in the matching element.

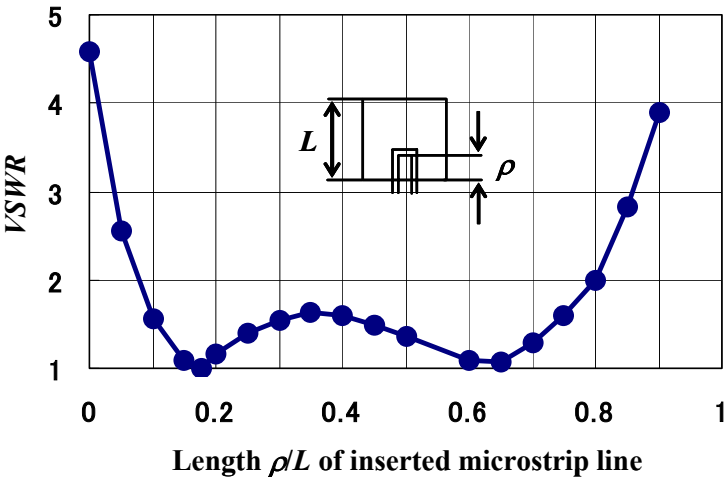
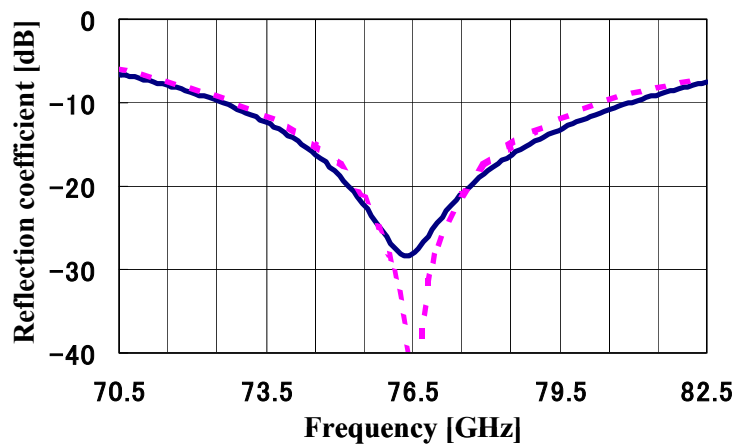


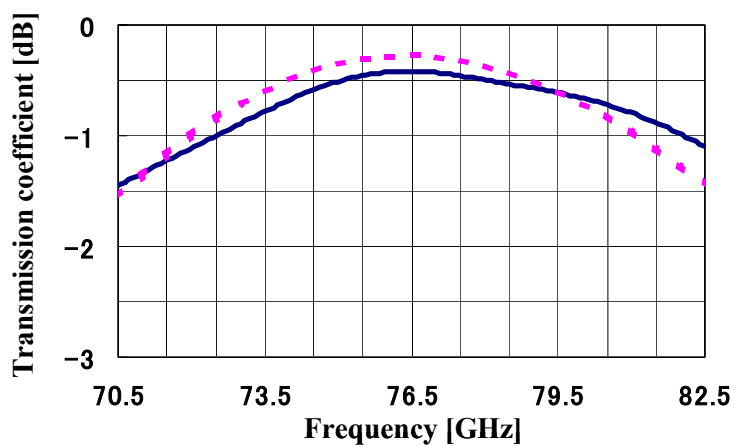
Fig. 4.6. $VSWR$ versus length ρ of inserted microstrip line normalized by length L of matching element.

4.3.2 Transmission characteristics

Reflection and transmission characteristics of the transition are shown in Fig. 4.7 (a) and (b), respectively. The vertical axis represents reflection or transmission coefficient, respectively, while the horizontal axis represents frequency from 70.5 GHz to 82.5 GHz. Calculated and measured results are represented by a dotted line and a solid line, respectively. Parameters of the calculation model listed in the Table 4.1 are used. The calculated results demonstrate



(a)



(b)

Fig. 4.7. Reflection and transmission characteristics. (a) Reflection characteristic and (b) transmission characteristic. (—: Cal., - - -: Mea.)

good performance with low loss that reflection coefficient and transmission loss at 76.5 GHz are below -40 dB and 0.3 dB, respectively. Furthermore, wideband characteristic is achieved such that bandwidth below -14 dB ($VSWR < 1.5$) is 4.53 GHz (5.9%). In this calculation, loss tangent $\tan \delta = 0.001$ and conductivity $\sigma = 5.8 \times 10^7$ S/m are used as loss factors. Transmission loss of 0.3 dB is separated to three kinds of losses such as conductivity loss of 0.2 dB, dielectric loss of 0.05 dB and radiation loss of 0.05 dB, respectively.

As a result of experiments shown in the Fig. 4.7 (a) and (b), low transmission loss characteristics are realized such that measured reflection coefficient and transmission loss at 76.5 GHz are -28.0 dB and 0.4 dB, respectively. Moreover, wideband characteristic is obtained such that bandwidth below -14 dB ($VSWR < 1.5$) is 5.22 GHz (6.8%). When transmission characteristics are measured, DUT (Device Under Test) is composed of a pair of transitions and the microstrip line connected between them. After the measured values excluding the microstrip line loss are divided by two, measured characteristics of one transition are shown in the Fig. 4.7 (a) and (b). Distance between centers of the waveguides is set to the length of 50 mm, which is long enough to distinguish a desired wave and an unwanted reflection wave in time domain. Microstrip line loss is measured to be 0.03 dB/mm at 76.5 GHz by LRL calibration method. In this measurement, time gate function is adopted to remove the unwanted reflection wave and high accuracy of measurement is realized. The dielectric substrate and the waveguide are contacted so that an air-gap does not exist. Even if the air-gap existed and leaky wave was excited, a choke structure around the waveguide could suppress the leaky wave.

In the fabricated transition, three parameters such as the length L of the matching element, the width W of it and the length ρ of the inserted microstrip line are compensated to be 1.12 mm, 1.12 mm and $0.25 L$ listed in () of the Table 4.1, which are 3% , 3% and 7% longer

than those of the calculation model. The compensation for the three parameters of the fabricated transition is needed and led experimentally because numerical analysis is carried out assuming that the conductor thickness of the calculation model is zero and that the shape of corners of the matching element in the model is a right angle although the shape of corners of actual matching element in the fabricated transition is rounded. Since the aim of this paper is mainly to clarify the relations between the parameters and the characteristics, details of the compensation are not discussed here, and the assumptions are also used in Chapter 4.3 in order to reduce calculation time.

4.3.3 Bandwidth

It is noticed from the Fig. 4.7 (a) that the bandwidth of the transition is wider than that of a conventional microstrip patch antenna element fabricated on a dielectric substrate with the same parameters. Therefore, relation between the bandwidth of the transition and the dimensions of the waveguide is investigated. Figure 4.8 shows the bandwidth ($VSWR < 1.5$) with variation of the dimensions of the waveguide. Calculation is carried out in case that the ratio of the broad wall to the narrow wall of the waveguide is constant as $a = 2b$ and that impedance matching at 76.5 GHz is obtained by adjusting the sizes of L and W of the matching element and the length ρ of the inserted microstrip line following to the dimensions of the waveguide. The vertical axis represents the bandwidth ($VSWR < 1.5$) while the horizontal axis represents the broad wall length a of the waveguide. Bandwidth of the transition is represented by a solid line and that of the conventional microstrip patch antenna element fabricated on a dielectric substrate with the same parameters is represented by a dotted line as a reference. The conventional microstrip patch antenna element has a structure subtracting the waveguide from the structure of the transition shown in the Fig. 4.1. As shown in the Fig. 4.8, the bandwidth of the transition becomes wider as the dimensions a and

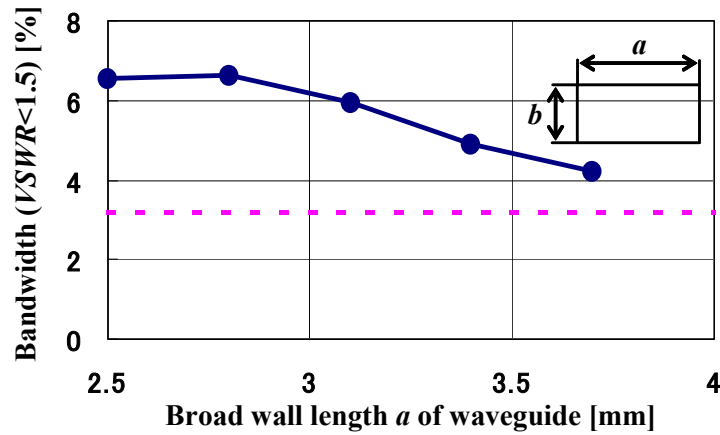


Fig. 4.8. Bandwidth ($VSWR < 1.5$) versus broad wall length a of waveguide in case of $a = 2b$. (—●—: Transition, - - - : Antenna)

b of the waveguide become smaller and maximum value of 6.5 %, which is twice as wide as that of the conventional microstrip patch antenna element, in case that the broad wall length a of the waveguide is set from 2.5 mm to 2.8 mm. Calculated transmission loss keeps constant value of 0.3 dB at 76.5 GHz, which is independent on the dimensions a and b of the waveguide.

Since not only numerical analysis but also fabrication and evaluation of the transition are aimed in this paper, the dimensions of the waveguide are chosen to be the same dimensions as a network analyzer interface (WR-12) which are 3.1 mm and 1.55 mm listed in the Table 4.1 in order to make actual measurement.

Since wider bandwidth is corresponded to lower quality factor Q , the quality factor Q is investigated to recognize the wide bandwidth characteristic. Bandwidth BW ($VSWR < S$) is written with quality factor Q as follows.

$$BW = \frac{100(S-1)}{Q \sqrt{S}} [\%] \quad (4.2)$$

The quality factor Q is defined as the energy stored in the matching element divided by the energy lost per radian. The energy lost per radian includes transmission power in a waveguide, conductor loss in the matching element, dielectric loss in the matching element and radiation loss in backward direction (in $+z$ direction). Consequently, the quality factor Q is written with quality factors relative to them such as Q_{WG} , Q_C , Q_D and Q_R .

$$\frac{1}{Q} = \frac{1}{Q_{WG}} + \frac{1}{Q_C} + \frac{1}{Q_D} + \frac{1}{Q_R} \quad (4.3)$$

Since conductor loss of 0.2 dB, dielectric loss of 0.05 dB and radiation loss of 0.05 dB are much smaller than transmission power in a waveguide described in Part 4.3.2, assumptions such as $Q_{WG} \ll Q_C$, Q_D and Q_R are introduced. In this case, the quality factor Q becomes to be mainly controlled by Q_{WG} . Consequently, relation between the bandwidth and parameters of the transition becomes clear by formulating Q_{WG} with parameters of the transition. Derivation of Q_{WG} is carried out with cavity model [4-3] and Dyadic Green's function in a waveguide [4-4]. The detailed derivation is presented in Appendix 4.A. Q_{WG} is formulated by

$$Q_{WG} = \frac{\omega \eta \epsilon_0 \epsilon_r L a b}{16 W t} \frac{1}{\left[\frac{\sin\left(\frac{W\pi}{2a}\right)}{\left(\frac{W\pi}{2a}\right)} \right]^2} \quad (4.4)$$

where ϵ_0 and η represent dielectric constant in free space and characteristic impedance in a waveguide, respectively, and other parameters were presented in Section 4.2. It is recognized from the equation (4.4) that Q_{WG} becomes smaller, which means the bandwidth of the transition becomes wider, as the dimensions a and b of the waveguide become smaller. It

is also recognized that the relation among the bandwidth, dielectric substrate thickness t and relative dielectric constant ϵ_r of the transition is the same as that of a conventional microstrip patch antenna element, that is, Q_{WG} becomes smaller, which means the bandwidth of the transition becomes wider, with increase of the dielectric substrate thickness t and decrease of the relative dielectric constant ϵ_r .

Although the relation between the bandwidth and the parameters as mentioned above is recognized from the equation (4.4) and is helpful for designers, estimated bandwidth based on the equation (4.4) is smaller than measured one and estimated one by using the finite element method. As the dimension of a of the waveguide becomes smaller from 3.7 mm to 2.5 mm, estimated bandwidth based on the equation (4.4) with parameters of Table 4.1 becomes wider from 2.7 % to 4.0 %. This is because coupling effect between the microstrip line and the matching element is not incorporated in this approximate analysis. Analysis taking the effect into account will be able to estimate bandwidth exactly.

4.3.4 Effects of errors in relative position

Degradation of transmission characteristics that may be caused by some errors in manufacturing is discussed in this part. Here, errors in manufacturing are etching errors in patterning on a dielectric substrate, errors in manufacturing a waveguide and errors in relative position between the dielectric substrate and the waveguide. Since probability of occurring the errors in relative position is higher than that of occurring the etching errors and the errors of manufacturing a waveguide in actual manufacturing, degradation of transmission characteristics caused by the errors in relative position is focused and discussed here.

Variation of transmission loss against the errors in relative position between the dielectric substrate and the waveguide is shown in Fig. 4.9. The errors in relative position is defined as difference between the center of the matching element patterned on the dielectric substrate

and the center of the waveguide cross section. The vertical axis represents the relative transmission loss normalized by transmission loss in case that there is no errors in relative position, while the horizontal axis represents positional error Δx in x direction and Δy in y direction, respectively. Calculated results are shown by a circle in Fig. 4.9 (a) for positional

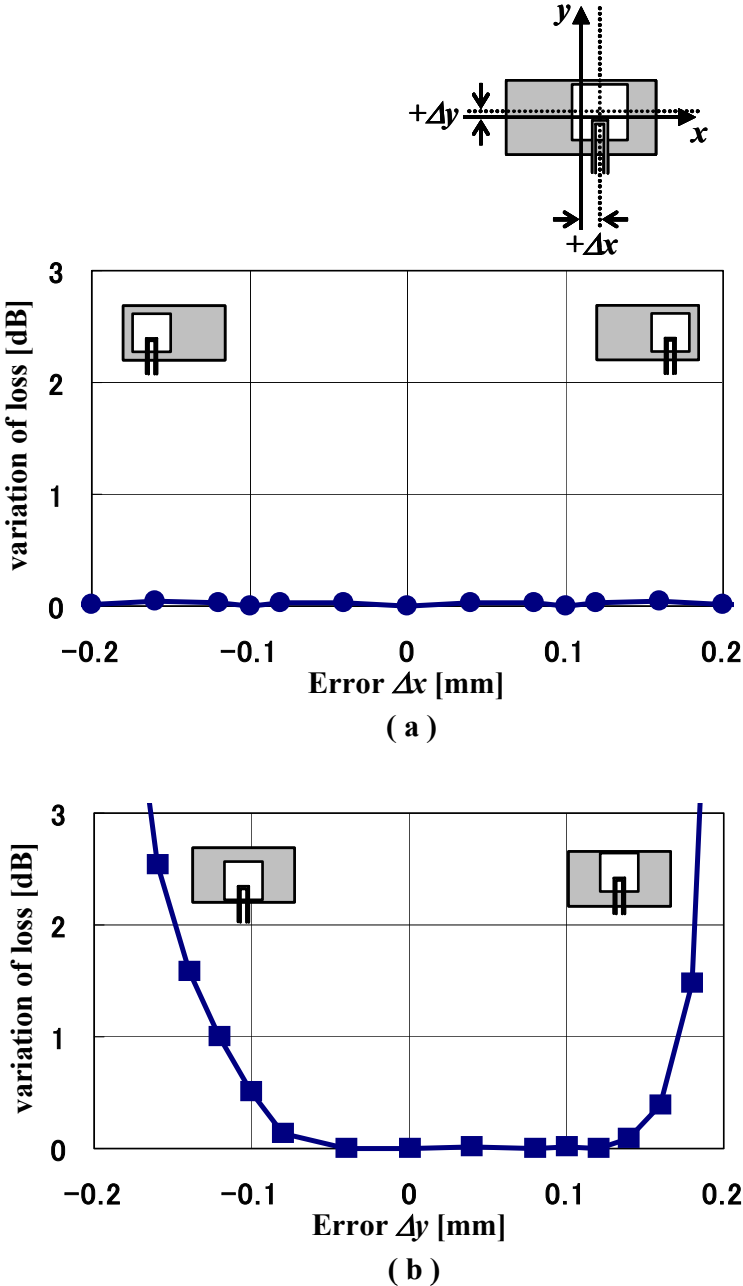


Fig. 4.9. Variation of loss versus errors in relative position between dielectric substrate and waveguide. (a) x direction and (b) y direction.

error Δx and a rectangular in Fig. 4.9 (b) for positional error Δy . Parameters of the calculation model listed in the Table 4.1 are used. As shown in Fig. 4.9 (a), there is no increase of transmission loss and its value keeps almost constant in case that positional error Δx in x direction varied within ± 0.2 mm. On the other hand, it can be seen from Fig. 4.9 (b) that transmission loss is remarkably degraded in case that positional error Δy in y direction is out of the range from -0.08 mm to 0.14 mm. Since quantity of positional error Δx in x direction is usually the same as that of positional error Δy in y direction in actual manufacturing, transmission characteristics are degraded firstly when positional error occurs in $-y$ direction, that is, the edge of the matching element where the microstrip line is inserted becomes close to the broad wall of the waveguide.

As a result of this investigation, it is clarified that minimum effect of positional errors to degradation of transmission characteristics is realized when the center of the matching element is designed as 0.03 mm offset in $+y$ direction against the center of the waveguide cross section and that manufacturing accuracy has to be within ± 0.1 mm in order to keep transmission loss less than 0.1 dB.

Figure 4.10 shows the resonant frequency varied with the errors in relative position between the dielectric substrate and the waveguide. The vertical axis represents the resonant frequency while the horizontal axis represents positional errors Δx and Δy , respectively. Calculated results are represented by a circle in Fig. 4.10 (a) for positional error Δx and a rectangular in Fig. 4.10 (b) for positional error Δy . Parameters of the calculation model described in the Table 4.1 are used. As shown in Fig. 4.10 (a), the resonant frequency keeps almost constant in case that positional error Δx varies within ± 0.2 mm. On the other hand, it can be seen from Fig. 4.10 (b) that the resonant frequency is remarkably decreased in case that positional error Δy is out of the range from -0.08 mm to 0.14 mm. It is clarified from the Fig. 4.9 and the Fig. 4.10 that increase of transmission loss is caused by decrease of the

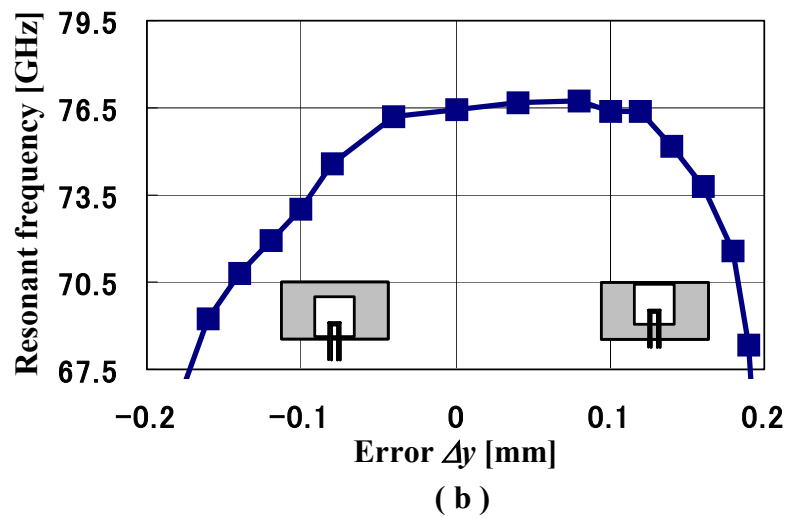
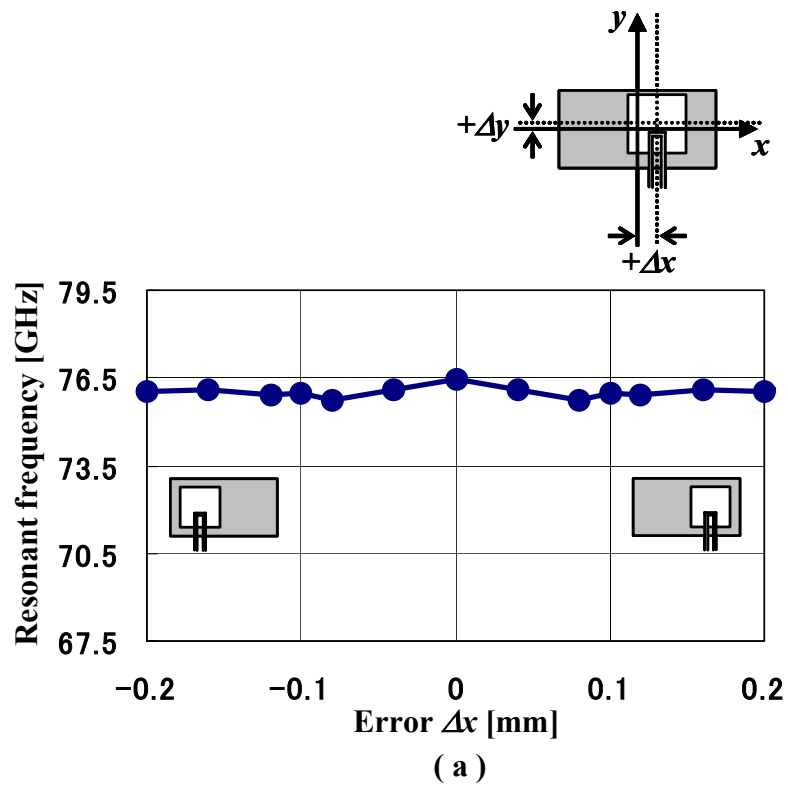


Fig. 4.10. Resonant frequency versus errors in relative position between dielectric substrate and waveguide. (a) x direction and (b) y direction.

resonant frequency.

Figure 4.11 shows electric field intensity distribution in xy plane including BB' -line in case that positional error Δy equals -0.14 mm. The electric field intensity E is given by the

equation (1) and normalized by its maximum value. There was a strong electric field between the matching element resonated TM_{01} mode and the broad wall of the waveguide. Since resonance phenomenon was caused by not only the matching element itself but also interaction between the broad wall of the waveguide and the matching element, the resonant length becomes longer than the resonant length L of the matching element itself, that is, resonant frequency becomes lower.

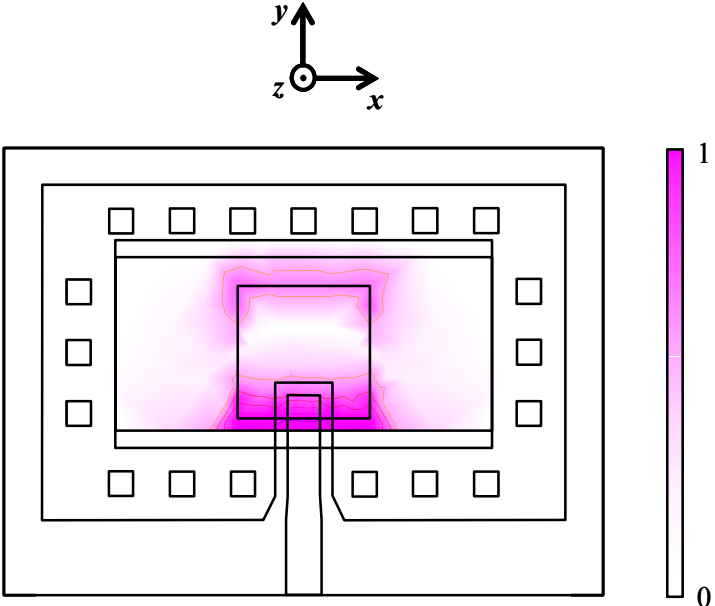


Fig. 4.11. Electric field intensity distribution in xy plane in case of $\Delta y = -0.14$ mm.

4.4. Conclusions

A new type of microstrip line to waveguide transition in the millimeter-wave band has been proposed. The proposed transition has the features of a structure fabricated on a single layer dielectric substrate. Impedance matching of the transition is achieved by controlling the

length L of the matching element and the length ρ of the inserted microstrip line. As a result of experiments, low transmission loss of 0.4 dB was realized at the design frequency of 76.5 GHz. Bandwidth of the transition was numerically investigated by the finite element method. This bandwidth also becomes twice as wide as that of a conventional microstrip patch antenna element fabricated on a dielectric substrate with the same parameters. Quality factor Q was introduced in order to recognize wide bandwidth characteristic and the relation between the bandwidth and other parameters such as the thickness t of the dielectric substrate and the relative dielectric constant ϵ_r . Moreover, the effect of errors in relative position between the dielectric substrate and the waveguide was also investigated since degradation of transmission characteristics may be caused by errors in manufacturing. Our results clearly show that degradation of transmission characteristics is caused by the shift of resonant frequency and keeps less than 0.1 dB for a manufacturing accuracy within ± 0.1 mm.

The proposed transition with a simple structure, low loss characteristic and robustness for assembling errors is suitable for connection between millimeter-wave components such as an antenna, an amplifier and a switch having an interface of a microstrip line or a waveguide. The millimeter-wave front-end module must have components that are suitable in cost, performance, size and reliability for the systems. The proposed transition with the above advantages is very useful to realize the low cost, low profile and high SNR millimeter-wave front-end module for the advanced sensor. Furthermore, the proposed transition will be used not only for the advanced sensor such as the automotive radar systems for a collision avoidance system and a stop & go system but also for wireless communication systems.

References

- [4-1] H. Iizuka, T. Watanabe, K. Sato, and K. Nishikawa, "Millimeter-wave microstrip line to waveguide transition fabricated on a single layer dielectric substrate," *IEICE Trans. Commun.*, vol.E85-B, no.6, pp.1169-1177, Jun. 2002.
- [4-2] H. Iizuka, T. Watanabe, S. Sato and K. Nishikawa, "Microstrip line to waveguide transition in millimeter-wave band," *IEICE Gen. Conf.*, B-1-136, Hiroshima, Japan, Mar. 2000.
- [4-3] J. R. James, P. S. Hall and C. Wood, "*Microstrip antenna theory and design*," Peter Peregrinus LTD., 1981.
- [4-4] R. E. Collin, "*Field theory of guided waves*," McGraw-Hill, New York, 1960.

4.A Appendix

Derivation of Q_{WG} is carried out with cavity model [4-3] and Dyadic Green's function in a waveguide [4-4]. Assuming that the thickness t of a dielectric substrate is much smaller than a wavelength in the dielectric substrate, TM_{01} mode is only resonated in the matching element having the length L and the width W . Electric field of TM_{01} mode has only z component E_{mez} at the coordinate system shown in the Fig. 4.2, and E_{mez} is given by

$$E_{mez} = E_0 \sin\left(\frac{\pi}{L}y\right) \quad \left(-\frac{W}{2} \leq x \leq \frac{W}{2}, -\frac{L}{2} \leq y \leq \frac{L}{2}\right) \quad (4A-1)$$

where E_0 is a maximum amplitude of electric field. Total energy W_T stored in the matching element is twice of electrical energy which is integration of z component of electric field E_{mez} in volume of the matching element since electrical energy equals magnetic energy at resonance. The total energy W_T is written as

$$W_T = 2 \left(\frac{\epsilon_0 \epsilon_r}{4} \right) \iiint_{v_0} |E_{mez}|^2 dv = \frac{E_0^2 \epsilon_0 \epsilon_r W L t}{4} \quad (4A-2)$$

On the other hand, Dyadic Green's function \vec{G}_e in terms of electric field of TE₁₀ mode as fundamental transmission mode of a waveguide is given by the equation (4A-3) with unit vectors $\vec{i}_x, \vec{i}_y, \vec{i}_z$, electric fields E_x, E_y, E_z and magnetic fields H_x, H_y, H_z .

$$\vec{G}_e = \frac{1}{2} E_y \vec{i}_y \left(H_{x0} \vec{i}_{x0} + H_{z0} \vec{i}_{z0} \right) \quad (4A-3)$$

where unit vectors, electric fields and magnetic fields with zero represent those of the source area located on the surface around the matching element and those without zero represent those of the view area located at the cross section of the waveguide. Components of electromagnetic fields $E_y, H_x,$ and H_z in the equation (4A-3) are given by

$$E_y = j \sqrt{\frac{2\eta}{ab}} \cos\left(\frac{\pi}{a} x\right) e^{-j\beta z} \quad (4A-4)$$

$$H_x = -j \sqrt{\frac{2}{ab\eta}} \cos\left(\frac{\pi}{a} x\right) e^{-j\beta z} \quad (4A-5)$$

$$H_z = \frac{\pi}{a Z_0 k} \sqrt{\frac{2\eta}{ab}} \sin\left(\frac{\pi}{a} x\right) e^{-j\beta z} \quad (4A-6)$$

where Z_0 is characteristic impedance in free space, and k and β are wavenumber in free space and wavenumber in a waveguide, respectively. Magnetic current \vec{M} on the surface around the matching element is written as the equation (4A-7) with z component E_{mez} of electric field and normal unit vector \vec{n} .

$$\vec{M} = E_{mez} \vec{i}_z \times \vec{n} \quad (4A-7)$$

Electric field \vec{E} of the view area located at the cross section of the waveguide is written as the equation (4A-8) by integration of the magnetic current \vec{M} on the surface S_0 around the matching element.

$$\vec{E} = \iint_{S_0} \vec{G}_e \bullet \vec{M} dS \quad (4A-8)$$

After simplification of the equation (4A-8), x component E_x and z component E_z of electric field \vec{E} of the view area become zero, and y component E_y of electric field \vec{E} is written as

$$E_y = \frac{8E_0 t \sin\left(\frac{W\pi}{2a}\right)}{\pi b} \cos\left(\frac{\pi}{a}x\right) e^{-j\beta z} \quad (4A-9)$$

Power P_{wg} transmitting through the waveguide cross section S where the view point is located is given by

$$P_{wg} = Re \left[\frac{1}{2} \iint_S \vec{E} \times \vec{H}^* \bullet \vec{n} dS \right] = \frac{1}{2\eta} \iint_S E_y^2 dS = \frac{16E_0^2 t^2 a \sin^2\left(\frac{W\pi}{2a}\right)}{\pi^2 b \eta} \quad (4A-10)$$

where an asterisk * represents complex conjugate. Finally, Q_{wg} is deviated and written as

$$Q_{wg} = \omega \frac{W_T}{P_{wg}} = \frac{\omega \eta \epsilon_0 \epsilon_r Lab}{16Wt} \frac{1}{\left[\frac{\sin\left(\frac{W\pi}{2a}\right)}{\left(\frac{W\pi}{2a}\right)} \right]^2} \quad (4A-11)$$

Chapter 5. Millimeter-wave transition from waveguide to two microstrip line

5.1 Introduction

A millimeter-wave transition from a waveguide to a microstrip line was proposed in previous chapter. A millimeter-wave transition from a waveguide to two microstrip lines and the design methodology are proposed [5-1] in this chapter. The transition can be composed of a single dielectric substrate attached to the waveguide. The configuration of the proposed transition is presented in Section 5.2. The design methodology includes two important aspects. These are the maximum bandwidth and the suppression of higher order modes. The design of the maximum bandwidth is described in Section 5.3, based on an analysis of the quality factor derived in previous chapter. In Section 5.4, the suppression of higher order modes is numerically investigated. The numerical investigation is validated by measurement results, and the assembly tolerance is also mentioned. This chapter is concluded in Section 5.5.

5.2 Proposal of transition from waveguide to two microstrip lines

A new transition from a waveguide to two microstrip lines is proposed in Fig. 5.1. The two microstrip lines and the waveguide short with two notches for them are etched on the dielectric substrate. The rectangular patch element and ground are etched on the backside. Via holes are placed along the circumference of the waveguide short to connect the waveguide short electrically to the ground. Port numbers are defined as #1 for the waveguide, and #2 and #3 for the microstrip lines. The parameters of the transition are presented in Table 5.1. The design frequency ranges from 76 GHz to 77 GHz. The transition can be composed of a single substrate attached to the waveguide, which is an

advantage for mass production.

The mode conversion from the waveguide to the two microstrip lines is achieved using the resonance of the rectangular patch element. The dominant TE_{10} mode of the waveguide is converted to the quasi-TEM mode of the microstrip lines, using the dominant TM_{01} mode of the rectangular patch element. The bandwidth of the transition is limited by the resonance. Thus, the wideband design is led by the analysis of the resonance of the rectangular patch element in the waveguide.

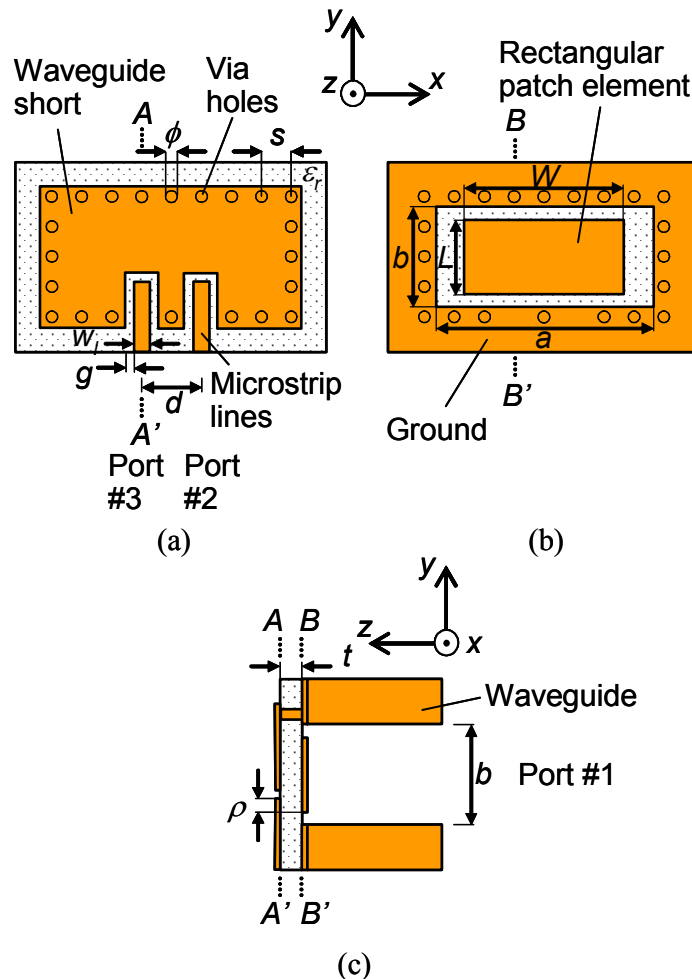


Fig. 5.1. Configuration of transition from waveguide to two microstrip lines. (a) Top view in AA' plane, (b) backside of dielectric substrate in BB' plane, and (c) cross section in yz plane.

Table 5.1. Parameters of transition from waveguide to two microstrip lines.

Parameters	Values
Width W of patch element	2.05 mm
Length L of patch element	1.07 mm
Length ρ of inserted microstrip lines	0.29 mm (0.32mm)
Width w_l of microstrip lines	0.27 mm
Width g of gaps	0.1 mm
Distance d between microstrip lines	1.03 mm
Thickness t of substrate	0.127 mm
Relative permittivity ϵ_e	2.2
Broad wall length a of waveguide	3.1 mm
Narrow wall length b of waveguide	1.55 mm
Diameter ϕ of via holes	0.2 mm
Space s between via holes	0.5 mm

The value in parentheses is for the prototype.

5.3 Wideband design using analytical model

The relationships between the parameters and the bandwidth are analyzed to specify the optimum parameters for wideband. Figure 5.2 shows an analytical model that uses a cavity model, which is used for the design of microstrip patch antennas, and the dyadic Green's function of the waveguide. The rectangular patch element on the dielectric substrate is placed in the short-terminated waveguide. L_e and W_e are the effective length and width of the rectangular patch element, including the fringing effect. t and ϵ_e are the thickness and effective relative permittivity of the dielectric substrate. The waveguide dimensions are a by b . The quality factor Q_E of the rectangular patch element is given by

$$\frac{1}{Q_E} = \frac{1}{Q_{WG}} + \frac{1}{Q_C} + \frac{1}{Q_D} \quad (5.1)$$

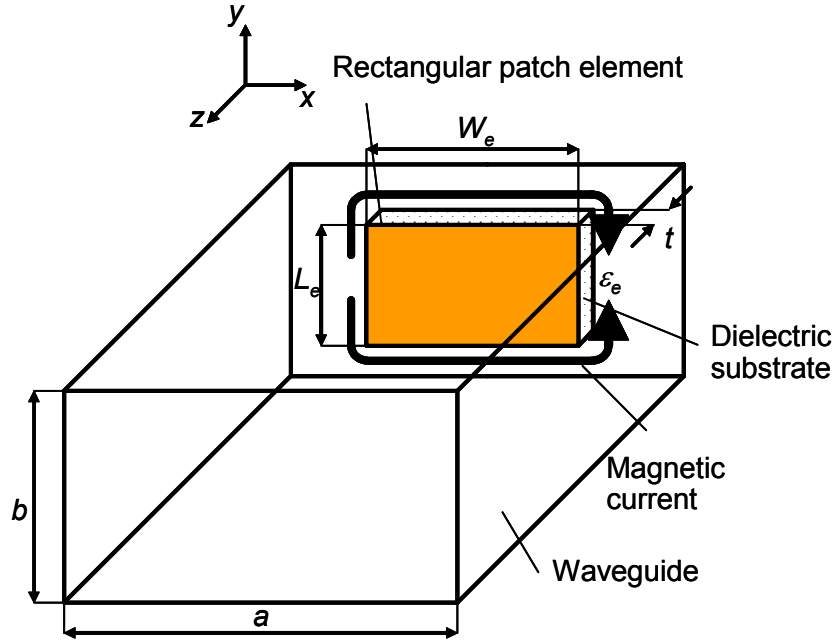


Fig. 5.2. Analytical model using cavity model and dyadic Green's function of waveguide. Rectangular patch element on dielectric substrate is placed in short-terminated waveguide.

where Q_{WG} , Q_C , and Q_D are quality factors of the power transmitted into the waveguide, the conductor loss, and the dielectric loss. Assuming that the thickness t of the dielectric substrate is much smaller than a free space wavelength, TM modes are excited in the rectangular patch element. When the dominant TE_{10} mode is excited in the waveguide, the rectangular patch element has a dominant TM_{01} mode, and its equivalent magnetic currents are depicted in Fig. 5.2. The quality factor Q_{WG} has been deviated with the cavity model and the dyadic Green's function of the waveguide.

$$Q_{WG} = \frac{15\omega\pi\epsilon_0\epsilon_e L_e ab}{2W_e t} \frac{1}{\sqrt{1 - \left(\frac{\lambda_g}{2a}\right)^2}} \frac{1}{\left(\frac{\sin\left(\frac{W_e\pi}{2a}\right)}{\left(\frac{W_e\pi}{2a}\right)}\right)^2} \quad (5.2)$$

where ω , ϵ_0 , and λ_g are angular frequency, permittivity in free space, and guided wavelength of waveguide. The quality factors Q_C and Q_D are the same as those for a rectangular patch element without the waveguide, which is a patch antenna [5-2].

$$Q_C = \frac{t}{\delta_s} \quad (5.3)$$

$$Q_D = \frac{1}{\tan \delta} \quad (5.4)$$

Where δ_s and $\tan \delta$ are the skin depth of the conductor and the loss tangent of the dielectric. The relationships between the parameters and the quality factors are analyzed in this paper starting with Equations (5.1) to (5.4). Equation (5.5) is considered to clarify the relationship between the quality factor Q_E and the effective width W_e .

$$\frac{\partial Q_E}{\partial W_e} = \frac{\partial Q_{WG}}{\partial W_e} = \frac{15\omega\pi^3 \epsilon_0 \epsilon_e L_e b}{8t} \frac{1}{a \sqrt{1 - \left(\frac{\lambda_g}{2a}\right)^2}} \frac{1}{\sin^2\left(\frac{\pi W_e}{2a}\right)} \left(1 - \frac{2}{\tan\left(\frac{\pi W_e}{2a}\right)} \frac{\left(\frac{\pi W_e}{2a}\right)}{\left(\frac{\pi W_e}{2a}\right)} \right) = 0 \quad (5.5)$$

Solving Equation (5.5) for the case of $W_e < a$, the effective width W_e is expressed in Equation (5.6).

$$W_e = \frac{2aC}{\pi} \quad (5.6)$$

Where C is a constant value of 1.166. Equation (5.6) gives the minimum Q factor. This indicates the existence of an optimum dimension of the effective width W_e for the wideband characteristic. Then, Q_{WG} is given by

$$Q_{WG} \Big|_{W_e = \frac{2aC}{\pi}} = \frac{15\omega\pi^2 \epsilon_0 \epsilon_e L_e b}{4t} \frac{1}{\sqrt{1 - \left(\frac{\lambda_g}{2a}\right)^2}} \frac{C}{\sin^2(C)} \quad (5.7)$$

On the other hand, Q_E with variation of broad wall length a of waveguide is described by

Equation (5.8), while satisfying Equation (5.6).

$$\left. \frac{\partial Q_E}{\partial a} \right|_{W_e = \frac{2aC}{\pi}} = - \frac{15 \omega \pi^2 \epsilon_0 \epsilon_e L_e b \lambda_g^2}{16t} \frac{C}{\sin^2(C)} \frac{1}{a^3 \left(1 - \left(\frac{\lambda_g}{2a} \right)^2 \right)^{\frac{3}{2}}} \quad (5.8)$$

Equation (5.8) is negative. It can be led that Q_E decreases as a increases. In other words, the bandwidth increases with increasing a , while the effective width W_e is set to the optimum width for wideband. The relationships between the other parameters and the bandwidth can be understood from Equation (5.2). The relationships between the parameters and the bandwidth are summarized in Table 5.2. These relationships are very useful for practical design, which includes choices not only for the dimensions of the rectangular patch element, but also for the dielectric substrate and the waveguide.

The existence of the maximum bandwidth with an optimum effective width of W_e is not affected by the number of feed lines and excitation methods, such as proximity coupling, slot coupling, direct feeding, and the like. Thus, this analysis can be applied to all transitions that have a rectangular patch element.

Table 5.2. Relationships between parameters and bandwidth.

Parameters		Bandwidth
Effective width W_e of patch element	$W_e = 2aC/\pi$	Max.
Broad wall length a of waveguide	\nearrow	\nearrow at $W_e = 2aC/\pi$
Narrow wall length b of waveguide	\searrow	\nearrow
Effective relative permittivity ϵ_e	\searrow	\nearrow
Thickness t of substrate	\nearrow	\nearrow
Effective length L_e of patch element	$\lambda_g/2$	-

C is constant value of 1.166.

5.4 Performance

In this section, the transition in Fig. 5.1 is investigated numerically, using the commercial package HFSS [5-3], which is based on the finite element method. The numerical investigation validates the analysis in Section 5.3 in terms of the bandwidth of the transition with variation of the width W of the rectangular patch element in Part 5.4.1, and clarifies the appropriate distance d between the microstrip lines to avoid higher order modes in Part 5.4.2. The numerical investigation is validated by the measurement results in Part 5.4.3. Assembling tolerance is discussed in Part 5.4.4.

5.4.1 Bandwidth

Figure 5.3 shows the simulated bandwidth for $|S_{11}| < -15$ dB with variation of the width W . The bandwidth in the vertical axis is normalized to a bandwidth BW_r of 4.03 GHz for a transition having a 1.11 mm by 1.11 mm square patch element with a single microstrip line. It can be seen that the bandwidth reaches a maximum of $1.2 BW_r$ at $W = 2.05$ mm. An

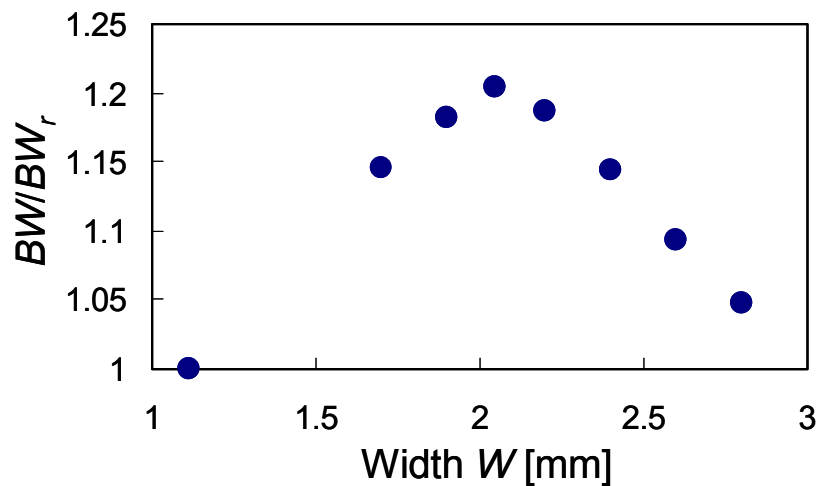


Fig. 5.3. Simulated bandwidth for $|S_{11}| < -15$ dB vs. width W of rectangular patch element. Bandwidth is normalized to $BW_r = 4.03$ GHz, the bandwidth for a square patch element having $W = L = 1.11$ mm.

effective width W_e of 2.3 mm was calculated, using Equation (5.6), for an E-band waveguide having $a = 3.1$ mm. The comparison of $W_e = 2.3$ mm in Fig. 5.2 with $W = 2.05$ mm in Fig. 5.1 validates the analysis described in Section 5.3, considering the fringing effect.

5.4.2 Distance between microstrip lines

The distance d between microstrip lines and its effect on the transmission characteristic is next analyzed. Figure 5.4 shows transmission characteristic $|S_{21}|$ with different values for the width W and distance d . The solid line represents $|S_{21}|$ when $W = 2.05$ mm and $d = 1.03$ mm, as shown in Table 5.1. There is no dip in the $|S_{21}|$ curve in the frequency range from 66.5 GHz to 86.5 GHz. $|S_{21}|$ is -3.3 dB from 76 GHz to 77 GHz, which corresponds to the insertion loss of 0.3 dB. At the same width $W = 2.05$ mm, but a different distance $d = 0.9$ mm, the transmission characteristic dips at 85.4 GHz, as represented by the dotted line. When $W = 2.35$ mm and $d = 1.62$ mm, there is a dip in the design frequency range from 76 GHz to 77 GHz, as represented by the dot-dashed line. This suggests that the occurrence of

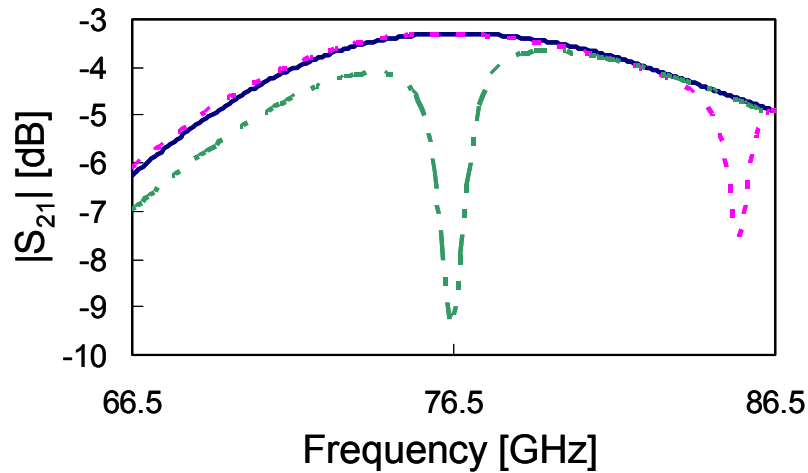
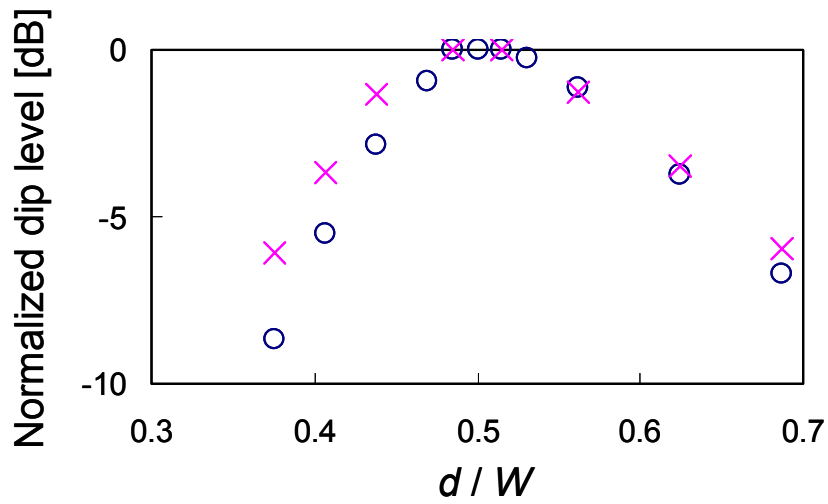
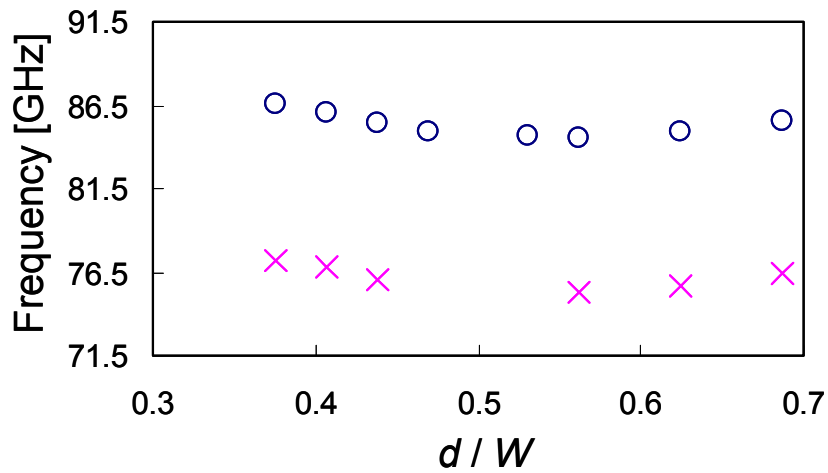


Fig. 5.4. Simulated transmission coefficient from waveguide to microstrip line.
 (—: $W = 2.05$ mm, $d = 1.03$ mm, - - - : $W = 2.05$ mm, $d = 0.9$ mm, ·····: $W = 2.35$ mm, $d = 1.62$ mm)



(a)



(b)

Fig. 5.5. Relationship between dip in transmission coefficient and distance between microstrip lines. (\circ : $W = 2.05$ mm, \times : $W = 2.35$ mm) (a) Dip level vs. normalized distance d/W . (b) Frequency of dip vs. normalized distance d/W .

the dip and its frequency depend on the parameters W and d .

Figures 5.5 (a) and (b) show the dip level and frequency with variation of distance d , with circles for $W = 2.05$ mm and crosses for $W = 2.35$ mm. The vertical axis in Fig. 5.5 (a) is the dip level, which is the magnitude compared to that without a dip. The horizontal axis is the distance d normalized to the width W . It can be seen in Fig. 5.5 (a) that the dip can be

avoided at both $W = 2.05$ mm and $W = 2.35$ mm when d is set to around $0.5 W$. The dip level increases as d/W increases or decreases from 0.5. As shown in Fig. 5.5 (b), the dip frequency is strongly dependent on the width W , differing significantly when $W = 2.05$ mm and $W = 2.35$ mm. However the frequency varies little for different values of d .

The near field distributions of the rectangular patch elements at 76.5 GHz are shown in

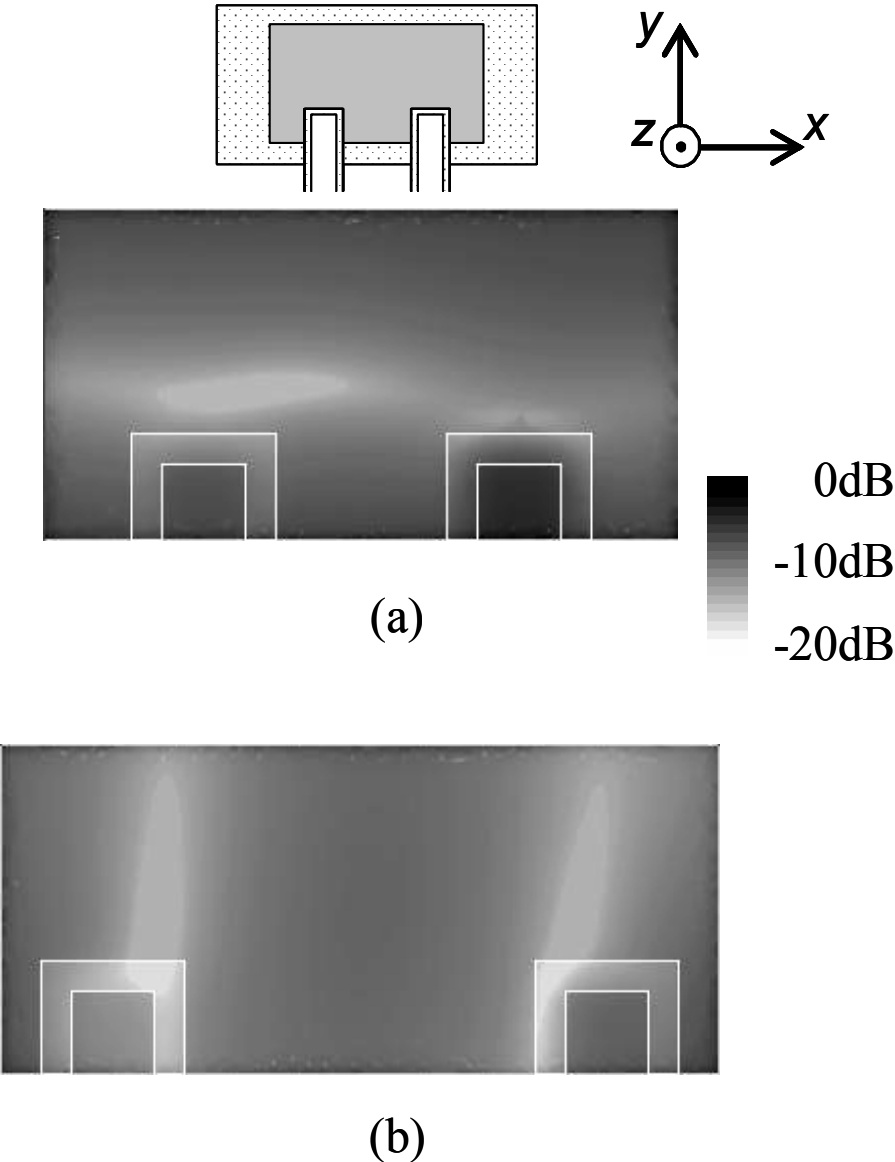


Fig. 5.6. Field distributions of rectangular patch elements at 76.5GHz. (a) $W = 2.05$ mm, $d = 1.03$ mm, (b) $W = 2.35$ mm, $d = 1.62$ mm.

Fig. 5.6 (a) for $W = 2.05$ mm and $d = 1.03$ mm ($d/W = 0.5$), and in Fig. 5.6 (b) for $W = 2.35$ mm and $d = 1.62$ mm ($d/W = 0.69$), which correspond to the solid line and the dot-dashed line in Fig. 5.4, respectively. The field intensity is normalized to the maximum value in each case, and ranges from - 20 dB to 0 dB. It is observed in Fig. 5.6 (a) that the fundamental mode of TM_{01} is excited. On the other hand, a higher order mode of TM_{20} is observed, as shown in Fig. 5.6 (b).

Based on the investigation so far, the dip in the transmission characteristic can be explained as follows. The voltage distributions in the TM_{2n} and TM_{m1} modes are depicted in Fig. 5.7, where m and n are zero or positive integers. When the two microstrip lines are inserted at zero voltage for TM_{2n} mode in the y -axis, represented by the dotted lines, TM_{2n} is not excited. An appropriate length ρ for the inserted microstrip lines results in low loss

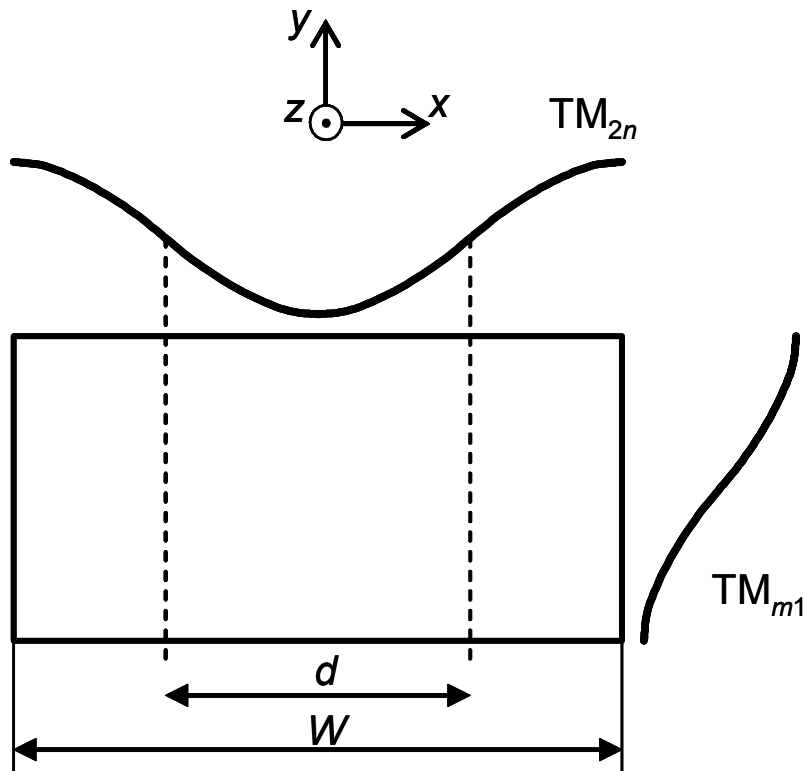


Fig. 5.7. Schematic diagram of voltage distributions in TM_{2n} and TM_{m1} modes.

transmission. In this case, d/W is 0.5. If the microstrip lines were inserted at non-zero voltage, the TM_{2n} mode would be excited, and a dip would occur in the transmission characteristic.

5.4.3 Measurement

Reflection and transmission coefficients are presented in Figs. 5.8 (a) and (b). The measurement and simulation results are represented by the solid and dotted lines, respectively.

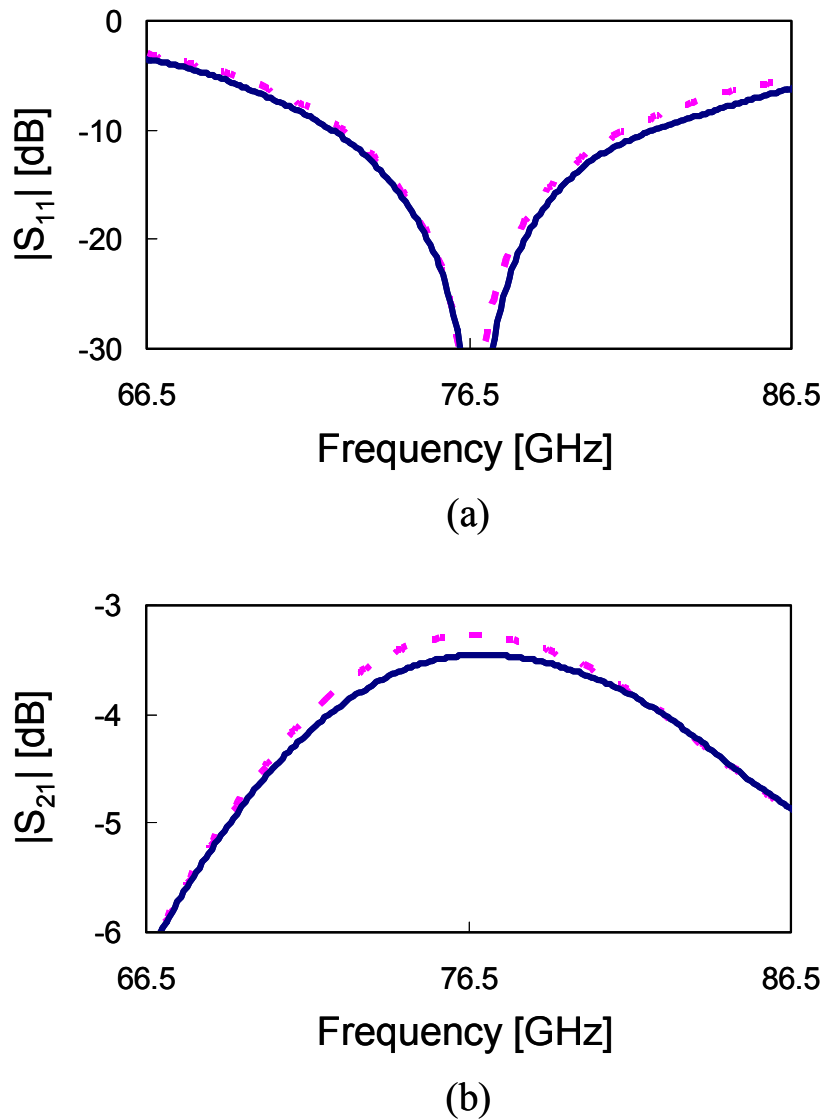


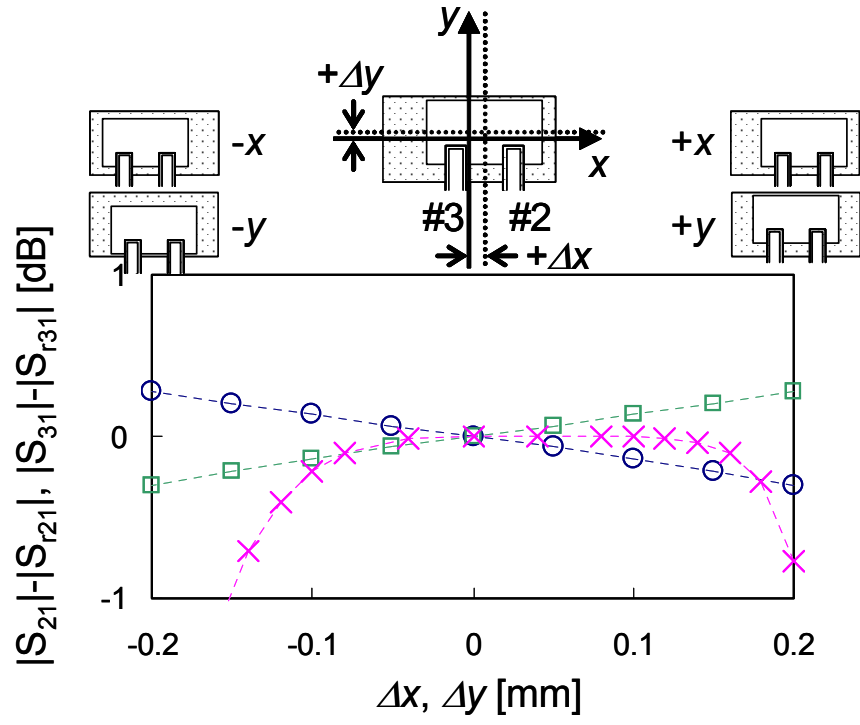
Fig. 5.8. Reflection and transmission characteristics when $W = 2.05$ mm and $d = 1.03$ mm. (—: measurement, - - - : Simulation) (a) Reflection coefficient of waveguide. (b) Transmission coefficient from waveguide to microstrip line.

The measurement results agree with simulation results. It can be seen from the simulation results that the bandwidth for $|S_{11}| < -15$ dB is 4.84 GHz, and $|S_{21}|$ is -3.3 dB in the frequency range from 76 GHz to 77 GHz. On the other hand, the measured bandwidth for $|S_{11}| < -15$ dB and $|S_{21}|$ are 5.29 GHz and -3.5 dB from 76 GHz to 77 GHz, respectively. The measured insertion loss is 0.5 dB. In this measurement, the DUT (device under test) was composed of a pair of transitions with a microstrip line between them. The measured $|S_{21}|$ in Fig. 5.8 (b) was given by taking the transmission coefficient of the DUT, subtracting the loss of the microstrip line, and dividing by two. The loss of microstrip line was measured by LRL calibration method as 0.03 dB/mm from 76 GHz to 77 GHz. The distance between the centers of the waveguides was set 50 mm, which was long enough to distinguish between desired and undesired waves in the time domain. A time gate function was used to exclude undesired waves, and high accuracy was achieved in this measurement.

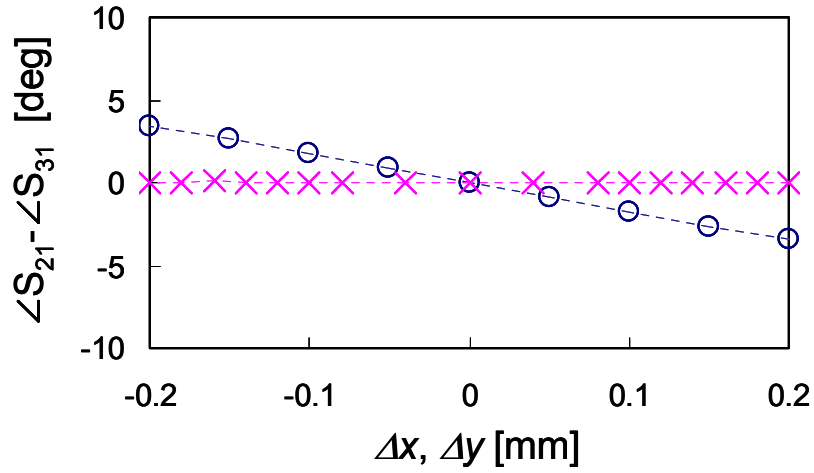
5.4.4 Tolerance for manufacturing accuracy

The effect of manufacturing accuracy on the performance of the transition is described here. Manufacturing accuracy includes the assembly accuracy between the substrate and waveguide and roundness accuracy of the corners of the waveguide. Since the simulation results were validated by the measurement results, the effect is numerically investigated.

Figure 5.9 shows the transmission coefficient at 76.5 GHz with variation of the relative positions of the dielectric substrate and the waveguide. Δx and Δy are defined as distances in the x -axis and y -axis from the center of the waveguide cross section to the center of the rectangular patch element etched on the dielectric substrate. The vertical axis in Fig. 5.9 (a) represents the relative transmission coefficients $|S_{21}|$ and $|S_{31}|$, where $|S_{r21}|$ and $|S_{r31}|$ in Fig. 5.9 (a) are the transmission coefficients when $\Delta x = \Delta y = 0$. Circles and squares represent the relative transmission coefficients $|S_{21}|$ and $|S_{31}|$ for Δx , while crosses represent $|S_{21}|$ and $|S_{31}|$



(a)



(b)

Fig. 5.9. Transmission characteristics at 76.5GHz with variation of the positions of substrate and waveguide. (a) Relative amplitudes of ports #2 and #3 to those when $\Delta x = \Delta y = 0$. (\circ : Port #2 for Δx , \square : port #3 for Δx , \times : ports #2 & #3 for Δy) (b) Phase difference between ports #2 and #3. (\circ : \square_x , \times : \square_y)

for Δy , due to the symmetry of the structure. $|S_{21}|$ decreases from + 0.3 dB to - 0.3 dB, and $|S_{31}|$ increases from - 0.3 dB to + 0.3 dB as Δx increases from - 0.2 mm to + 0.2 mm. In

other words, the transmission coefficient decreases as the microstrip line moves farther from the center of the waveguide cross section. The amplitude difference between ports #2 and #3 remains ± 0.3 dB when the assembly tolerance in the x -axis is within ± 0.1 mm. The degradation of $|S_{21}|$ and $|S_{31}|$ is less than 0.1 dB when Δy varies from - 0.08 mm to + 1.6 mm, and rapidly increases with any further increase in $|\Delta y|$. It can be said that the transmission loss is less than 0.1 dB when the assembly tolerance within ± 0.1 mm in the y -axis, when the transition is designed with $\Delta y = + 0.04$ mm. With regard to the phase characteristic shown in Fig. 5.9 (b), the phase difference between ports #2 and #3 varies from + 3.5 degrees to - 3.5 degrees as Δx increases from - 0.2 mm to + 0.2 mm. The phase difference is less than 1.8 degrees when the assembly tolerance is within ± 0.1 mm in the x -axis. On the other hand, the phases of both ports are the same for Δy , due to the symmetry of the structure. The assembly tolerance of the transition would be acceptable, but the amplitude and phase differences may be a concern, depending on the manufacturing accuracy of the mass production facilities and the system requirements. When the antenna in a radar system needs a very low side lobe level, the assembly tolerance and its effect on side lobe degradation should be given careful consideration.

Figure 5.10 shows the resonant frequency with variation of relative positions of the dielectric substrate and the waveguide. The resonant frequency is almost constant within ± 0.2 mm for Δx , while the resonant frequency decreases rapidly when Δy is outside the range of - 0.08 mm to + 0.16 mm. This indicates that the degradation of the transmission coefficient for Δy in Fig. 5.9 (a) is caused by the shift in the resonant frequency.

The effect of the roundness of the corners of the waveguide on transmission loss is presented in Fig. 5.11. The vertical axis represents the relative transmission coefficient at 76.5 GHz, where $|S_{r21}|$ is the transmission coefficient when $\Delta x = \Delta y = 0$. The horizontal axis represents the radius r of the corners of waveguide. It can be seen that the roundness of the

corners does not affect the transmission loss when r varies from 0 mm to 0.7 mm.

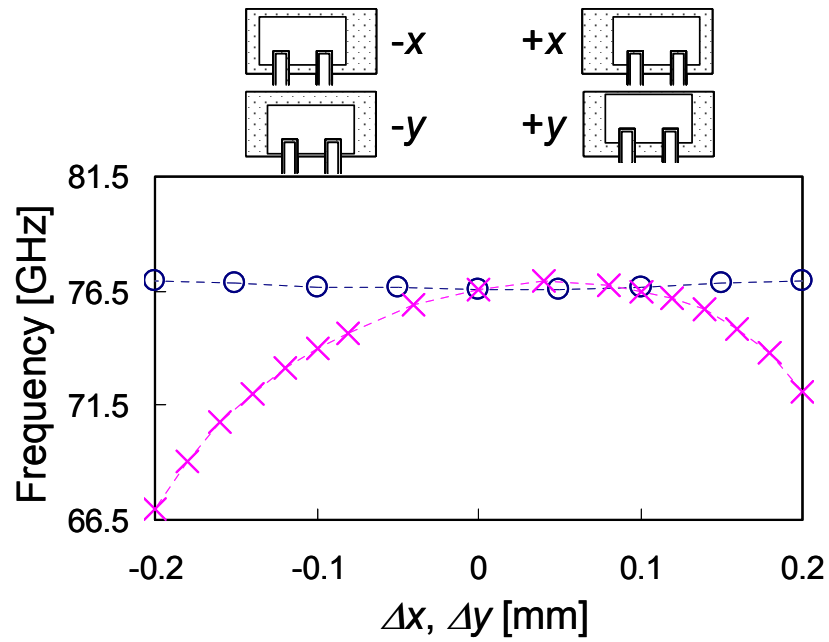


Fig. 5.10. Resonant frequency with variation of the positions of substrate and waveguide. (\circ : Δx , \times : Δy)

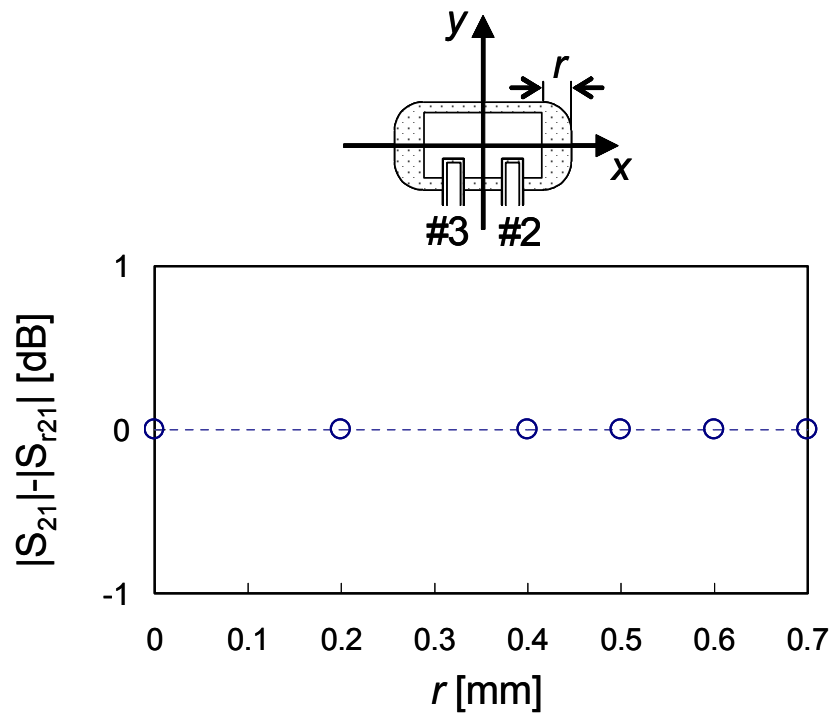


Fig. 5.11. Transmission characteristic at 76.5 GHz with variation of radius r of waveguide corners. $|S_{r21}|$ is amplitude when $\Delta x = \Delta y = 0$.

5.5 Conclusions

A transition from a waveguide to two microstrip lines and the design methodology have been proposed. The existence of an optimum width of the rectangular patch element for wideband was confirmed both analytically and numerically. The suppression of higher order modes was confirmed in a transition with two microstrip lines, when the distance between microstrip lines was set to half the width of the rectangular patch element. The measurement results showed an insertion loss of 0.5 dB, and both the wideband and the suppression were confirmed.

The wideband design method using the cavity model and the dyadic Green's function of the waveguide is independent of the number of microstrip lines and the excitation methods. The wideband design method will be widely used for transitions having rectangular patch element in waveguide.

References

- [5-1] H. Iizuka, K. Sakakibara, and N. Kikuma, "Millimeter-wave transition from waveguide to two microstrip lines using rectangular patch element," *IEEE Trans. Microwave Theory Tech.*, vol.55, no.5, pp. 899-905, May. 2007.
- [5-2] K. Hirasawa and M. Haneishi, *Analysis, design, and measurement of small and low-profile antennas*, Artech house, 1992, pp. 57–58.
- [5-3] *Ansoft HFSS ver.10.1*, Ansoft Corp., Pittsburgh, PA

Chapter 6. Digital TV antennas for omnidirectional pattern synthesis

6.1 Introduction

Modified H shaped antennas and their arrangement are proposed for automotive digital TV reception [6-1]-[6-3] in this chapter. The antennas are installed at the top of the front and rear windows. The antenna has the feature that a figure-8 radiation pattern is rotated with increasing frequency. Four symmetrically mounted antennas have gain to the sides of the car as well as to the front and rear directions. The configuration of the antenna is described in Section 6.2 and calculation results obtained by the method of moment are presented in Section 6.3. The control method for resonant frequencies and the combined pattern of the four antennas are also discussed. Measured radiation properties of a single antenna and mounted antennas on a car are presented in Section 6.4. The coverage of the combined pattern of four prototype antennas is discussed. An antenna module including balun, filter, and amplifier, is briefly mentioned in Section 6.5. This chapter is concluded in Section 6.6.

6.2 Proposal of modified H shaped antenna

Figure 6.1 (a) shows a modified H shaped antenna. Two wires $a-b-c-d-e$ and $f-g-h-i-j$ are symmetrically placed around the center m of the antenna and connected by the wire $c-m-h$. The parts $a-b-c$ and $f-g-h$ of the two wires are longer than the parts $c-d-e$ and $h-i-j$. The antenna is placed in the xy plane. A control system for combining received signals is shown in Figure 6.1 (b). The received signals of the four antennas are down-converted, weighted and combined. The weight vector for each signal is controlled, based on the MRC method. The four antennas mounted at the top of the front and rear windows are also depicted. The antenna plane, which includes the antenna element, is inclined from the horizontal plane in an actual car. Radiation patterns in the xy plane are discussed in this section, and the effect of

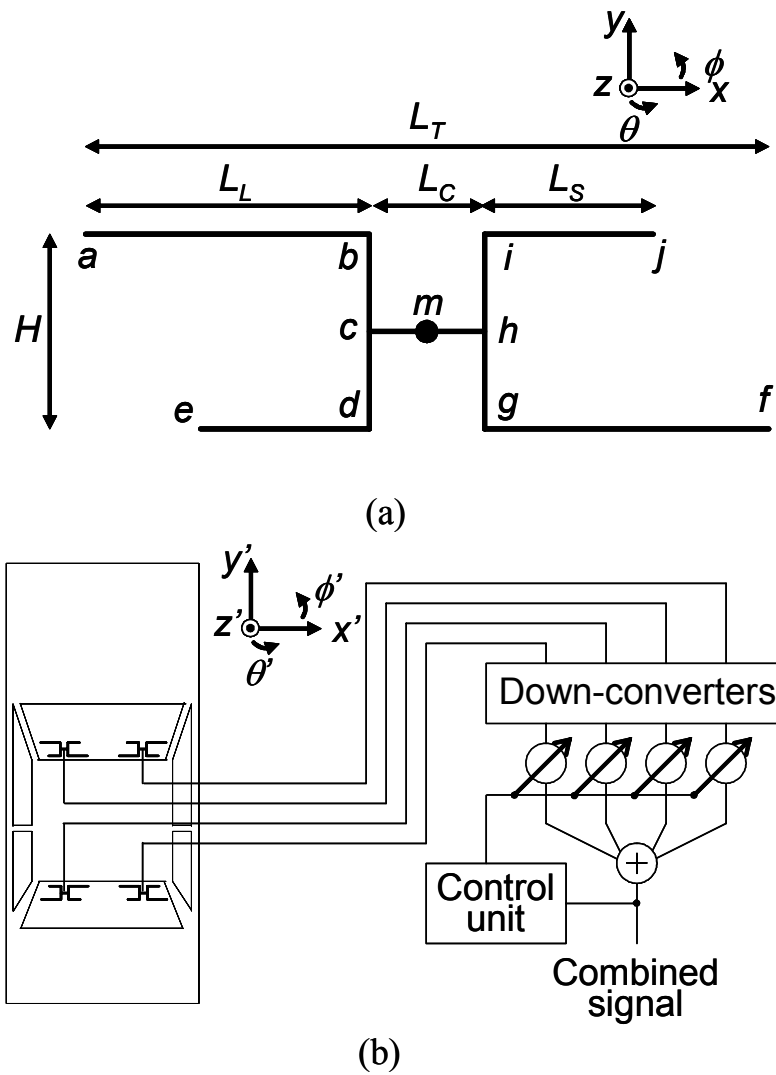


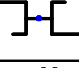
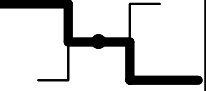

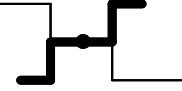


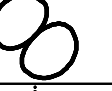
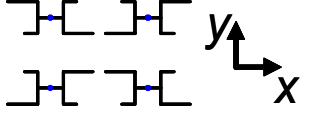
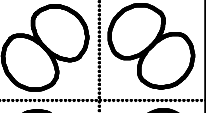
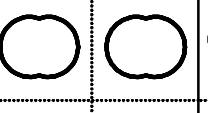
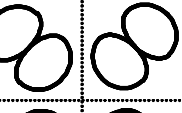



Fig. 6.1. Modified H shaped antenna and control system for combining received signals for automotive digital terrestrial reception. (a) Antenna element and (b) control system.

the angle of the antenna plane is also described.

A design concept of the coverage in the xy plane is summarized in Table 6.1. Mechanism of the antenna is described with Figure 6.1 (a) and Table 6.1. The antenna has three resonant modes. Each resonant mode is excited when a part of the antenna has the length of a half resonant wavelength. The frequency band for digital terrestrial services is divided into three bands. The wire $a-b-c-m-h-g-f$ is resonated at the low frequency, which is series resonance.

Parallel resonance occurs at the middle frequency. The two wires *a-b-c-d-e* and *f-g-h-i-j* are resonated. Series resonance occurs again at the high frequency, in which the wire *e-d-c-m-h-i-j* is resonated. The radiation pattern of a single element is rotated clockwise with increasing frequency. The minimum level of relative amplitude increases when the maximum radiation is directed toward the *x*-axis direction. The four antennas are symmetrically placed around the *x*-axis and *y*-axis directions in Table 6.1, which is assumed to be equivalent to installation at the top of the front and rear windows. The symmetrical arrangement allows coverage of 360 degrees.

Table 6.1. Concept covering 360 degrees in the *xy* plane using the four antennas across the frequency band for digital terrestrial services.

		Frequency		
		Low	Middle	High
Single element 	Current distribution			
	Radiation pattern			
Radiation patterns of four elements 				
				

6.3 Performance

Radiation properties of the antenna are calculated in free space using the commercial simulator “FEKO” based on the method of moment. The parameters of the calculation model are presented in Table 6.2.

Table 6.2. Parameters of the calculation model.

Total length L_T of antenna	257 mm
Length L_L of wires $a-b$ & $f-g$	114 mm
Length L_S of wires $d-e$ & $i-j$	79.5 mm
Length L_C of wire $c-m-h$	29 mm
Hight H of antenna	60 mm
Radius r of wires	0.5 mm

Figure 6.2 shows the resonant frequency for the three modes, versus the ratio of lengths of longer and shorter arms, when their combined length is kept constant. The parameters other than L_S , L_L and L_T were the same as those shown in Table 6.2. The 1st resonant frequency f_1 and the 3rd resonant frequency f_3 can be controlled by the ratio L_S/L_L , while maintaining little variation of the 2nd resonant frequency f_2 . f_1 increased from 430 MHz to 521 MHz when L_S/L_L was increased from 0.45 to 1, since the wire $a-b-c-m-h-g-f$ became shorter. At the same time, f_3 decreased from 762 MHz to 590 MHz since the wire $e-d-c-m-h-i-j$ became longer. f_2 and f_3 had the same value of 590 MHz at L_S/L_L of 0.836 and then disappeared with the further increase of L_S/L_L . The behavior of input impedance as a function of L_S/L_L is different from parallel resonance to series resonance. The real part of input impedance

steeply decreased in parallel resonance from 789 Ω to 102 Ω for f_2 when L_S/L_L was increased from 0.45 to 0.836 because the distances from the center of wire $a-b-c-d-e$ to the point c and from $f-g-h-i-j$ to the point h became shorter. On the other hand, the variation of the real part was relatively small in series resonance. The values of the real part were from 37 Ω to 49 Ω for f_1 and from 40 Ω to 102 Ω for f_3 . Understanding the behavior of input impedance is helpful for a design in terms of minimum reflection at the feed point.

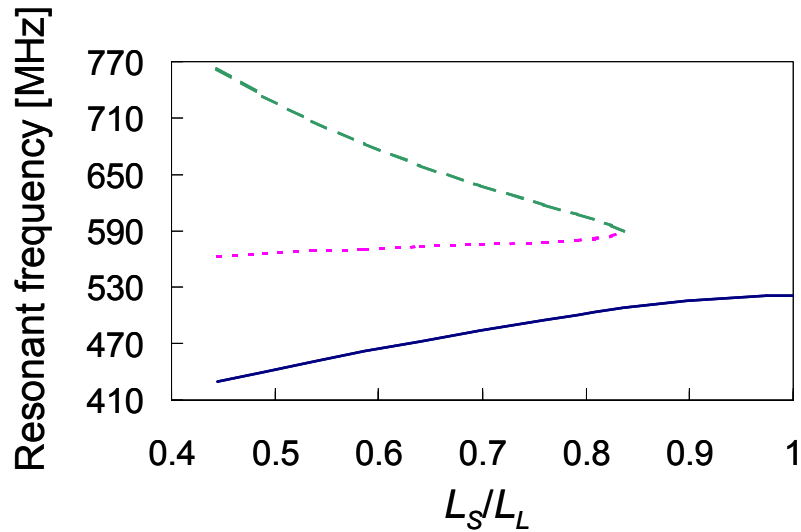


Fig. 6.2. Calculated resonant frequency with variation of the ratio of the lengths L_S/L_L . The length (L_S+L_L) is constant. (— : f_1 , : f_2 , - - - : f_3)

Figure 6.3 shows the resonant frequency for the three modes, versus the length L_C , when the lengths $(L_S+L_C+L_L)$ and (L_L-L_S) are kept constant. f_2 increased from 499 MHz to 641 MHz when L_C was increased from 0.02 L_T to 0.2 L_T since the two wires $a-b-c-d-e$ and $f-g-h-i-j$ became shorter. Meanwhile, f_1 and f_3 showed little variation. The variation of input impedance was large for parallel resonance and small for series resonance as with the previous case. The real part of input impedance increased in parallel resonance from 185 Ω

to 367Ω for f_2 when L_C increased. On the other hand, the values of real part in series resonance were from 39Ω to 80Ω for f_1 and from 46Ω to 110Ω for f_3 .

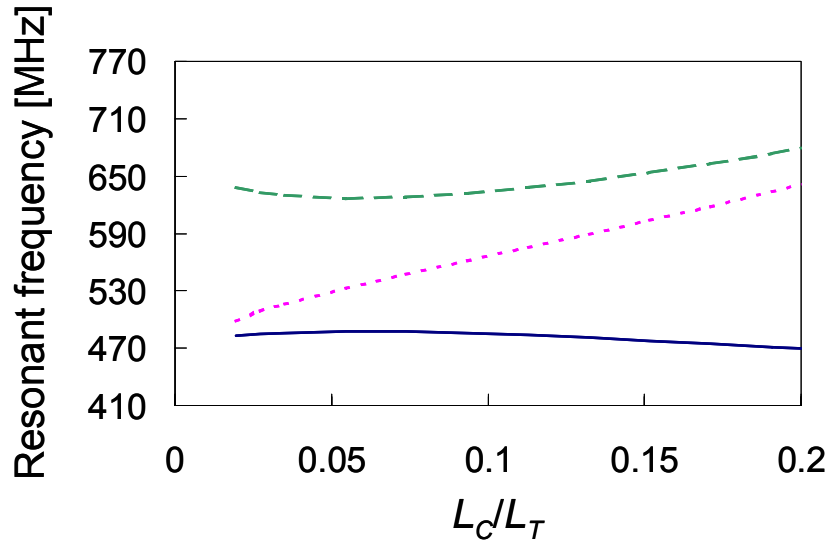


Fig. 6.3. Calculated resonant frequency with variation of the lengths L_C . The lengths $(L_S+L_C+L_L)$ and (L_L-L_S) are constant. (— : f_1 , : f_2 , - - - : f_3)

Current distributions are shown in Figure 6.4. Each position from the point a to e along the wire $a-b-c-d-e$ and from the point f to j along the wire $f-g-h-i-j$ corresponds to the horizontal axis from 0 mm to 253.5 mm. The position of the wires from the point c to m and h to m starts at 275 mm and ends at 289.5 mm. The three lines represent current distributions at three resonant frequencies f_1, f_2 and f_3 , which are 484 MHz, 576 MHz and 638 MHz for the calculation model with the parameters shown in Table 6.2. Voltage of 1 V is excited at the feed point m . Large current flowed along the wire $a-b-c-m-h-g-f$ and relatively small current flowed on the wires $c-d-e$ and $h-i-j$ at 484 MHz. Also, large current flowed along the wire $e-d-c-m-h-i-j$ and relatively small current flowed on the wires $a-b-c$ and $f-g-h$ at 638 MHz. Amplitude and phase had cosine and almost constant distributions along the wire

in both frequencies. Cosine distribution was observed in amplitude on the wires $a-b-c-d-e$ and $f-g-h-i-j$ at 576 MHz. Phase was almost constant, although there was a shift of 25 degrees at the points c and h . Amplitude was small on the wire $c-m-h$. This is one of the features of parallel resonance.

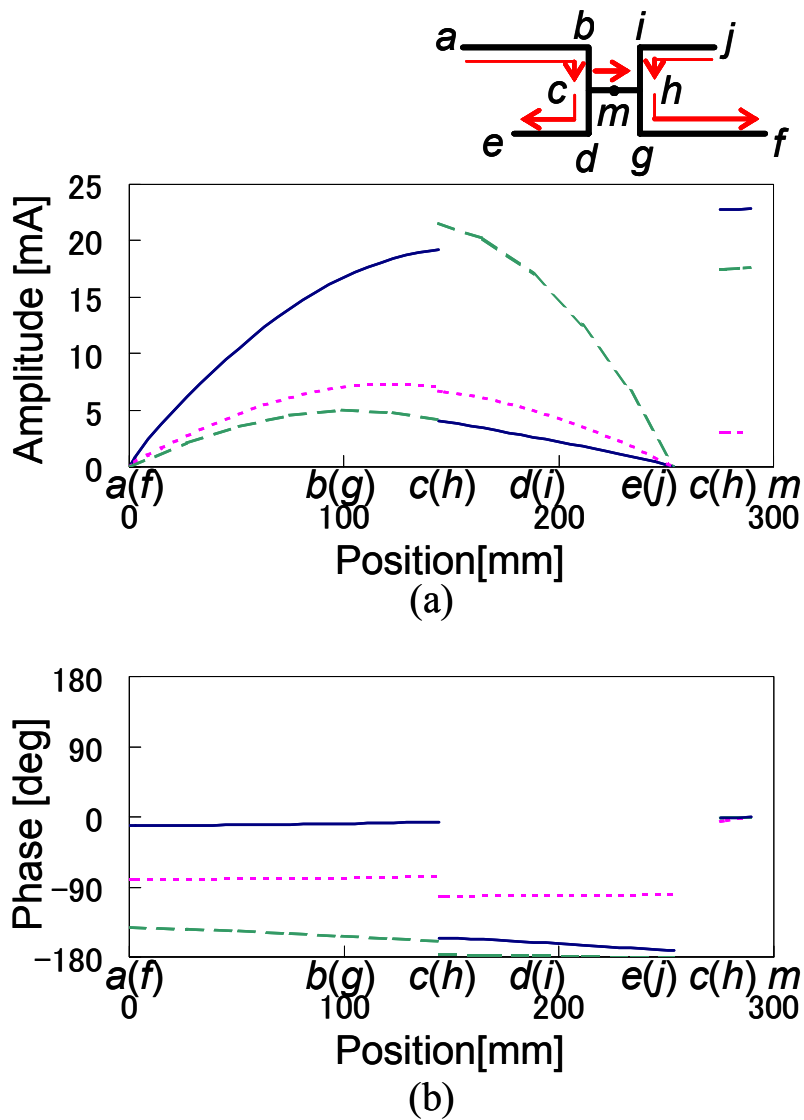


Fig. 6.4. Calculated current distributions of the modified H shaped antenna. (— : 484 MHz, : 576 MHz, - - - : 638 MHz) (a) Amplitude and (b) phase.

Figure 6.5 shows the radiation patterns in the xy plane at the three resonant frequencies. Reflection loss is included when the antenna is terminated with characteristic impedance of 110Ω . Inclined figure-8 radiation patterns were observed. The figure-8 radiation patterns seem to be rotated clockwise with increasing frequency.

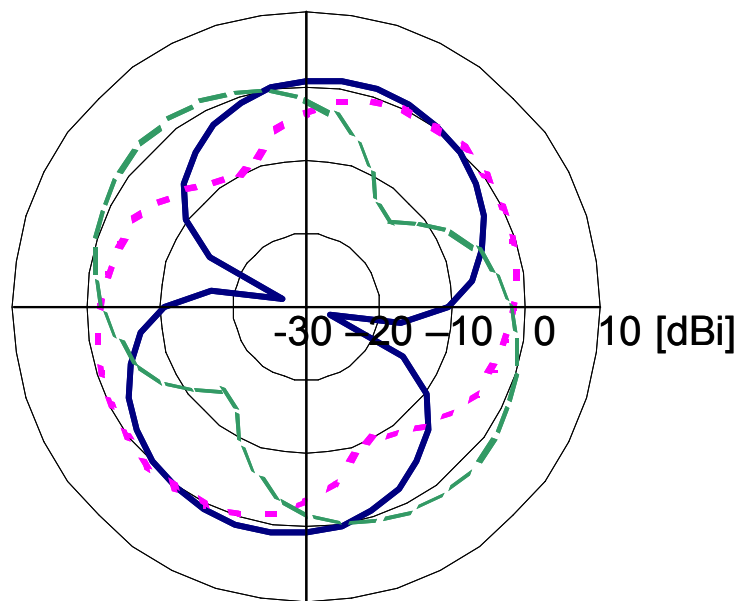
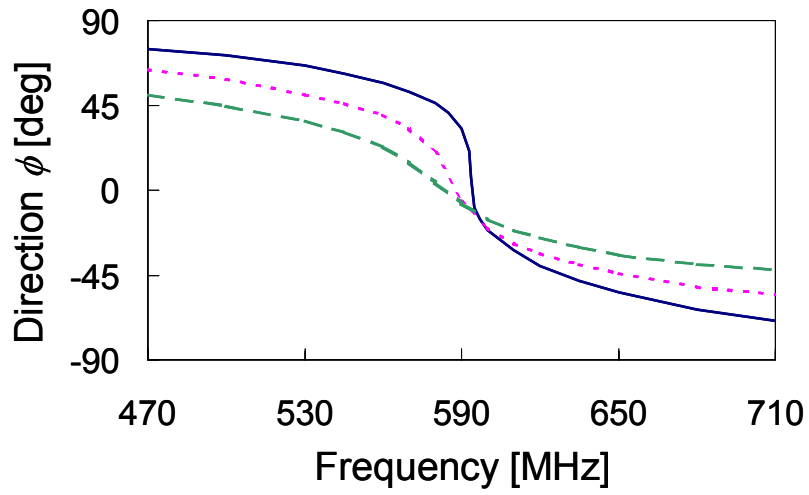
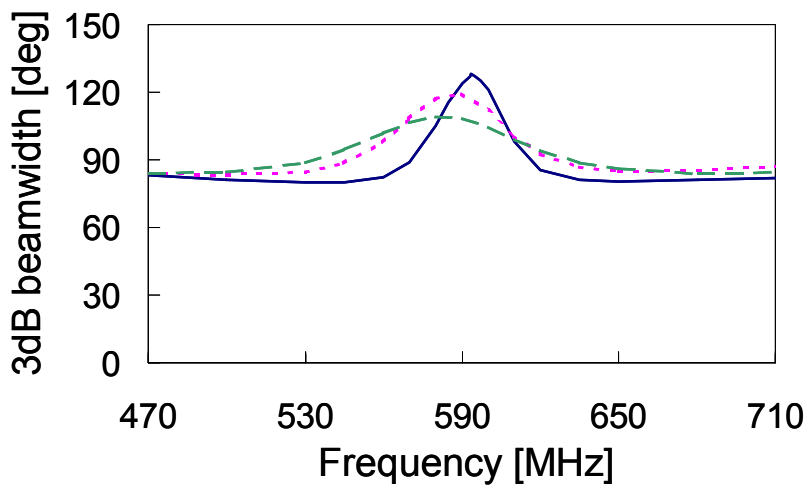


Fig. 6.5. Calculated radiation patterns of the modified H shaped antenna in the xy plane. (— : 484 MHz, : 576 MHz, - - - : 638 MHz)

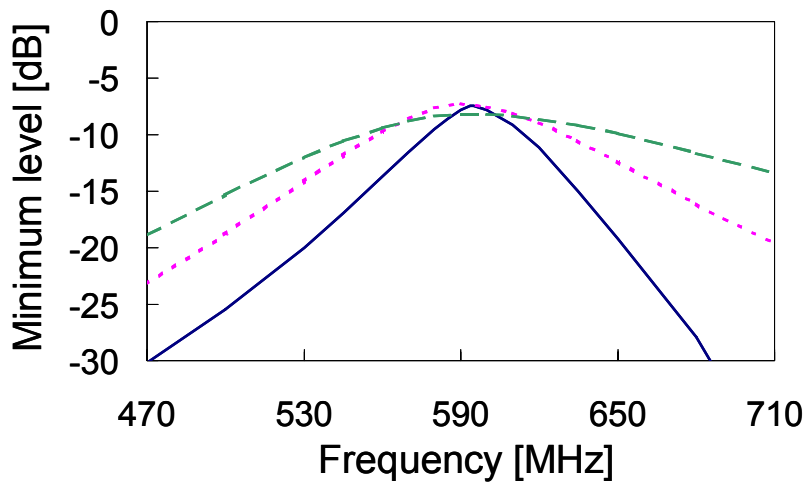
The radiation patterns in the xy plane were analyzed in detail. Figure 6.6 shows a summary of this analysis focusing on the direction ϕ of the maximum radiation, 3 dB beamwidth and the minimum level of relative amplitude as a function of frequency. The height H was varied with L_L , L_S and L_T while keeping the values of $(H+L_L+L_S)$ and (L_L-L_S) constant. Clockwise rotation was clearly observed. The direction ϕ of the maximum radiation varied from 75 degrees to -69 degrees from 470 MHz to 710 MHz in the case of $H = 60$ mm. The maximum radiation was directed toward the x -axis direction at 594 MHz,



(a)



(b)



(c)

Fig. 6.6. Calculated direction of the maximum radiation, 3dB beamwidth, and the minimum level of relative amplitude in the xy plane as a function of frequency. (— : $H = 60$ mm, : $H = 90$ mm, - - - : $H = 120$ mm) (a) Direction of maximum radiation, (b) 3 dB beamwidth, and (c) minimum level of relative amplitude.

which was higher than the parallel resonant frequency of 576 MHz. 3 dB beamwidth reached the widest value of 128 degrees at $\phi = 0$ degree. Moreover, the minimum level of relative amplitude reached the maximum value of -7.4 dB. The results suggest that the four symmetrically placed antennas as shown in Table 1 can avoid unacceptably weak gain across 360 degrees when each antenna has the same direction of the maximum radiation as well as the different direction. Radiation performance was slightly improved in terms of the coverage by the four antennas when the height H increased. The height H is usually limited by the installation area. The results also suggest that a height of $H = 60$ mm is acceptable. The combined pattern of the four antennas is discussed here. Directivity $D_{MRC}(\theta, \phi)$ combined with the MRC method is given by [6-4]

$$D_{MRC}(\theta, \phi) = \frac{1}{\sqrt{\sum_{n=1}^4 A_n^2(\theta_0, \phi_0)}} \sum_{n=1}^4 A_n(\theta_0, \phi_0) A_n(\theta, \phi) e^{j\psi_n} \quad (6.1)$$

where,

$$\psi_n = kx_n(\sin \theta \cos \phi - \sin \theta_0 \cos \phi_0) + ky_n(\sin \theta \sin \phi - \sin \theta_0 \sin \phi_0) \quad (6.2)$$

(θ_0, ϕ_0) is the direction of signal arrival. $A_n(\theta, \phi)$ and (x_n, y_n) are amplitude of received signal from the direction (θ, ϕ) and the position of the n th antenna. k is wave number. The peak plot is used to discuss the coverage. The peak plot $D_{PP}(\theta, \phi)$ is defined as the plotted pattern of the peak $D_{MRC}(\theta_0, \phi_0)$ of the combined pattern and described by equation (6.3).

$$D_{PP}(\theta, \phi) = D_{MRC}(\theta_0, \phi_0) \Big|_{\theta_0=\theta, \phi_0=\phi} = \sqrt{\sum_{n=1}^4 A_n^2(\theta, \phi)} \quad (6.3)$$

An omni-directional pattern of the peak plot in the ϕ plane indicates that the combined pattern steering beam has the same gain for any direction in the ϕ plane. The averaged gain G_{AVE} is given by

$$G_{AVE} = \frac{1}{2\pi} \int_0^{2\pi} |D_{PP}(\theta, \phi)|^2 d\phi \quad (6.4)$$

Figure 6.7 shows the minimum and averaged gain of the peak plot of the four antennas in free space. The minimum gain represented by a solid line is higher than -5.8 dBi across the frequency band from 470 MHz to 710 MHz, and shows the advantages of the proposed antennas over four dipole array, which has a deep null toward the x -axis direction. The peak plot is omni-directional at the two frequencies of 568 MHz and 636 MHz. The peak plot has the minimum gain toward the x -axis direction from 470 MHz to 568 MHz and from 636 MHz to 710 MHz, and toward the y -axis direction from 568 MHz to 636 MHz. On the other hand, the averaged gain of the peak plot was from 3.3 dBi to 4.5 dBi. The reflection loss of less than 1.2 dB was included. In the case of the ideal half wavelength dipole antenna, an averaged gain is -1.4 dBi. The averaged gain of the peak plot of the proposed antennas is almost the same with that of the dipole antennas considering the reflection loss and the number of antenna elements.

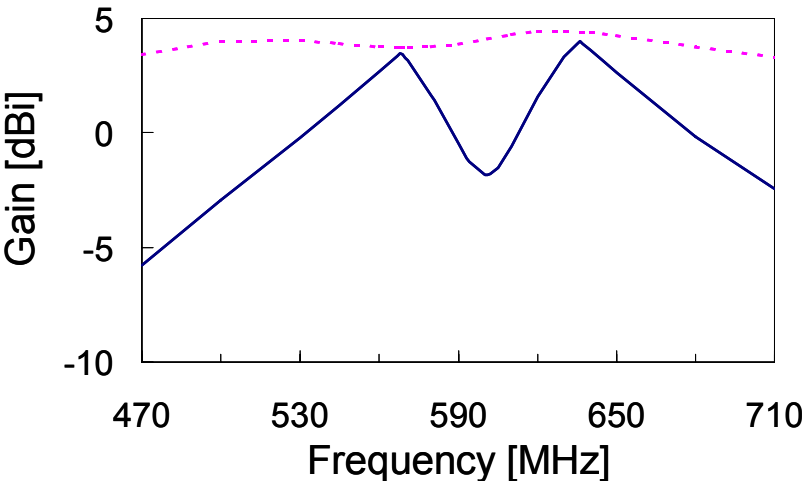


Fig. 6.7. Calculated averaged and minimum gain of the peak plot of the four antennas in free space. (— : Minimum gain, - - - : Averaged gain)

Radiation patterns of the antennas placed in the xy plane have been discussed so far. The effect of the angle of the antenna plane from the xy plane to radiation pattern is presented here. Figure 6.8 shows relative amplitude of radiation pattern of the antenna with variation of the rotation angle of the antenna plane from the xy plane at $\phi = 90$ degrees. The degradation of radiation pattern is caused toward the x -axis direction. Relative amplitude toward the x -axis direction goes down with increasing the angle from the horizontal plane since the polarization plane is varied together with the antenna plane. The same characteristic is given from 470 MHz to 710 MHz and represented by a solid line. The experimental car has an angle of approximately 30 degrees from the horizontal plane for both the front and rear windows. The degradation of radiation pattern is estimated to be -1.3 dB. On the other hand, there is little variation of radiation pattern toward the y -axis direction. The relative amplitudes toward the y -axis direction are represented from 470 MHz to 710 MHz with a step of 30 MHz. The values of the relative amplitudes represented by nine dotted lines are from 0 dB to 0.6 dB.

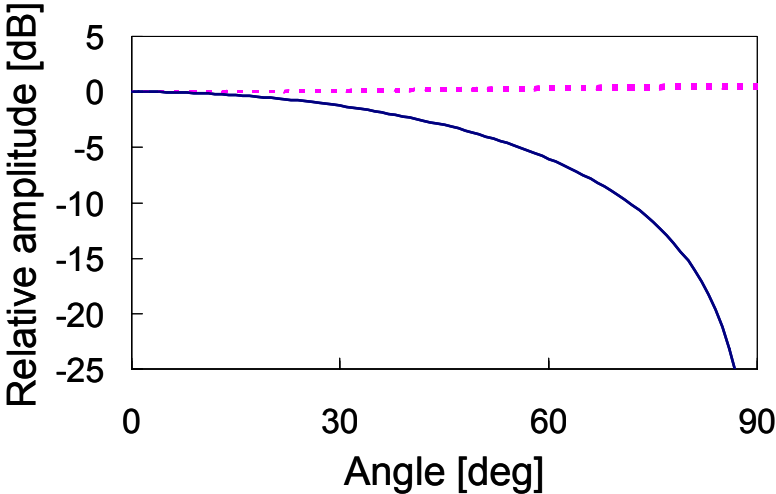
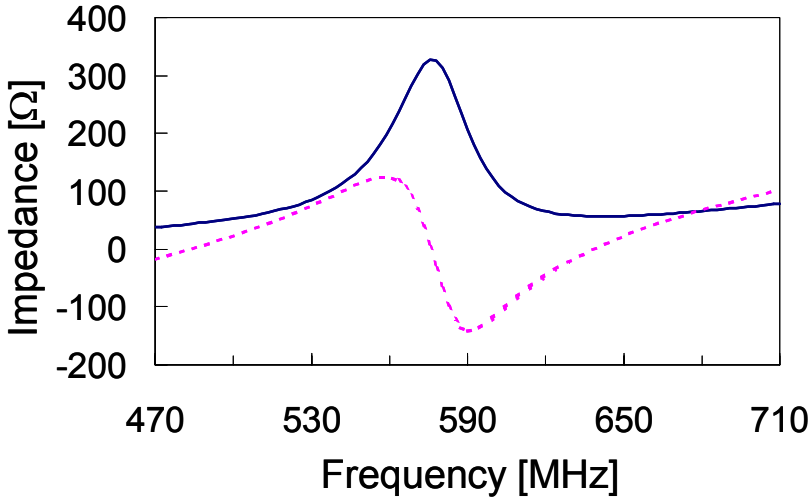
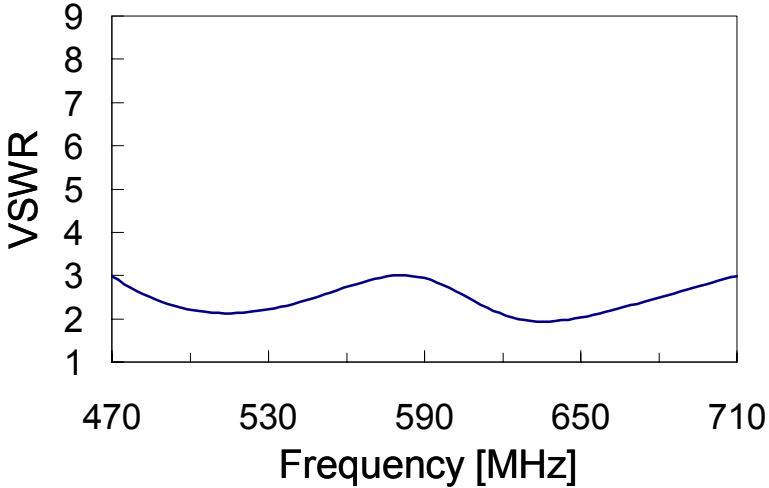


Fig. 6.8. Relative amplitude toward the x -axis and y -axis directions with variation of the rotation angle of the antenna plane from the xy plane. (— : x -axis direction, : y -axis direction)

Figure 6.9 (a) shows calculated input impedance. Three resonant modes were observed. The real part has a peak and the imaginary part goes down at 576 MHz. This indicates parallel resonance. The imaginary part goes up at 484 MHz and 638 MHz, respectively, which are series resonance. The real part has little variation at 484 MHz and 638 MHz due to the effect of parallel resonance at 576 MHz, although the real part generally goes up in series resonance. Calculated VSWR with respect to 110Ω is shown in Figure 6.9 (b). The



(a)



(b)

Fig. 6.9. Calculated input impedance and VSWR. (a) Input impedance (— : Real part, - - - : Imaginary part) and (b) VSWR with respect to 110Ω .

value of 110Ω was chosen to obtain the widest bandwidth. VSWR was less than 3 from 470 MHz to 710 MHz.

6.4 Prototype antennas

6.4.1 Single element

The wires shown in Figure 6.1 (a) were etched on a typical FR4 substrate having dielectric constant of 4.6 and the thickness of 0.8 mm. The width of the lines was 1 mm. The lengths L_L , L_S and L_C were experimentally adjusted to 102 mm, 67 mm and 30 mm, respectively, with constant value of $H = 60$ mm, since the value of H was specified for car installation. The prototype antenna has a LC balun and a parallel feed line between the LC balun and the feed

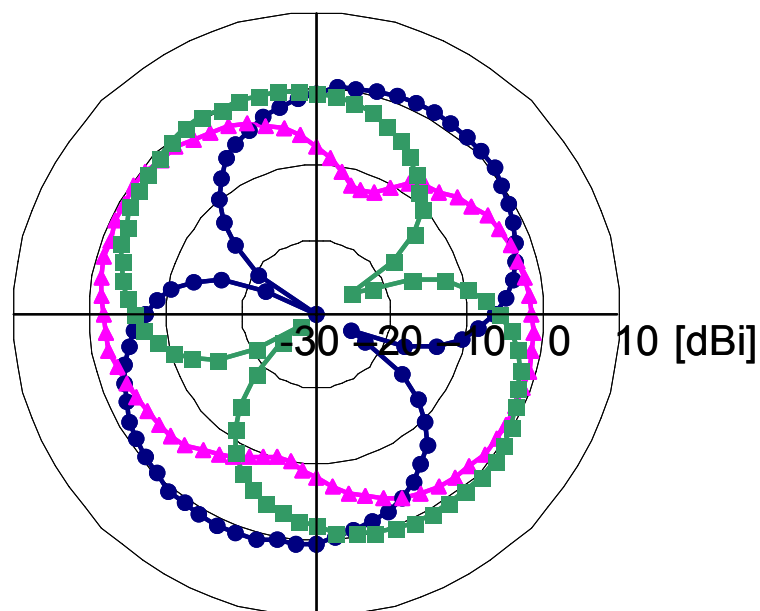


Fig. 6.10. Measured radiation patterns of a prototype antenna in the xy plane.
 (—●— : f_1 , —▲— : f_2 , —■— : f_3)

point m . The LC balun transforms impedance from 110Ω to 50Ω as well as balance-unbalance mode. The LC balun consists of a high pass filter (HPF), a low pass filter (LPF) and a T-junction. Both filters have the 5th order Butterworth function. 3 dB cutoff frequency is set at a lower frequency of 272 MHz for the HPF and a higher frequency of 1228 MHz for the LPF than the frequency band from 470 MHz to 710 MHz so that both filters may give flat amplitude and out of phase. Insertion loss of the LC balun was measured to be 0.3 dB across the frequency band. The parallel feed line has the length of 40 mm. The width of each line and the distance between the centers of the two lines were chosen to be 0.8 mm and 1.1 mm referring to [6-5], so that characteristic impedance would be 110Ω . Figure 6.10 shows the measured radiation patterns at the three frequencies. The figure-8 radiation patterns were rotated clockwise with increasing frequency as the calculation results predicted. VSWR was measured to be less than 3 from 470 MHz to 710 MHz.

6.4.2 Mounted antennas

After the validity of the performance of the single element, four prototype antennas were mounted at the top of the front and rear windows of the car as shown in Figure 6.1 (b). The distance between the edge of the metal roof and the nearest side of the prototype antennas was set at 20 mm. The spacings of antenna elements were, respectively, 600 mm in the x' -axis direction and 1600 mm in the y' -axis direction. Figure 6.11 (a), (b), (c) and (d) show typical measured radiation patterns of the four prototype antennas in the ϕ' plane at 530 MHz. Each prototype antenna had gain to the x' -axis direction as well as to the y' -axis direction because the four antennas in free space had inclined figure-8 radiation patterns. The peak plot combined with the radiation patterns in Figure 6.11 (a), (b), (c) and (d) is shown in Figure 6.11 (e). A near omni-directional pattern was achieved in the ϕ' plane. In terms of vertical plane, gain of the peak plot decreased with increasing the angle ϕ' , because radiation patterns

of the mounted prototype antennas were affected by the effect of the car body. The values of the minimum gain of the peak plot were -2.3 dBi for $\theta' = 70$ degrees, -3.7 dBi for $\theta' = 80$

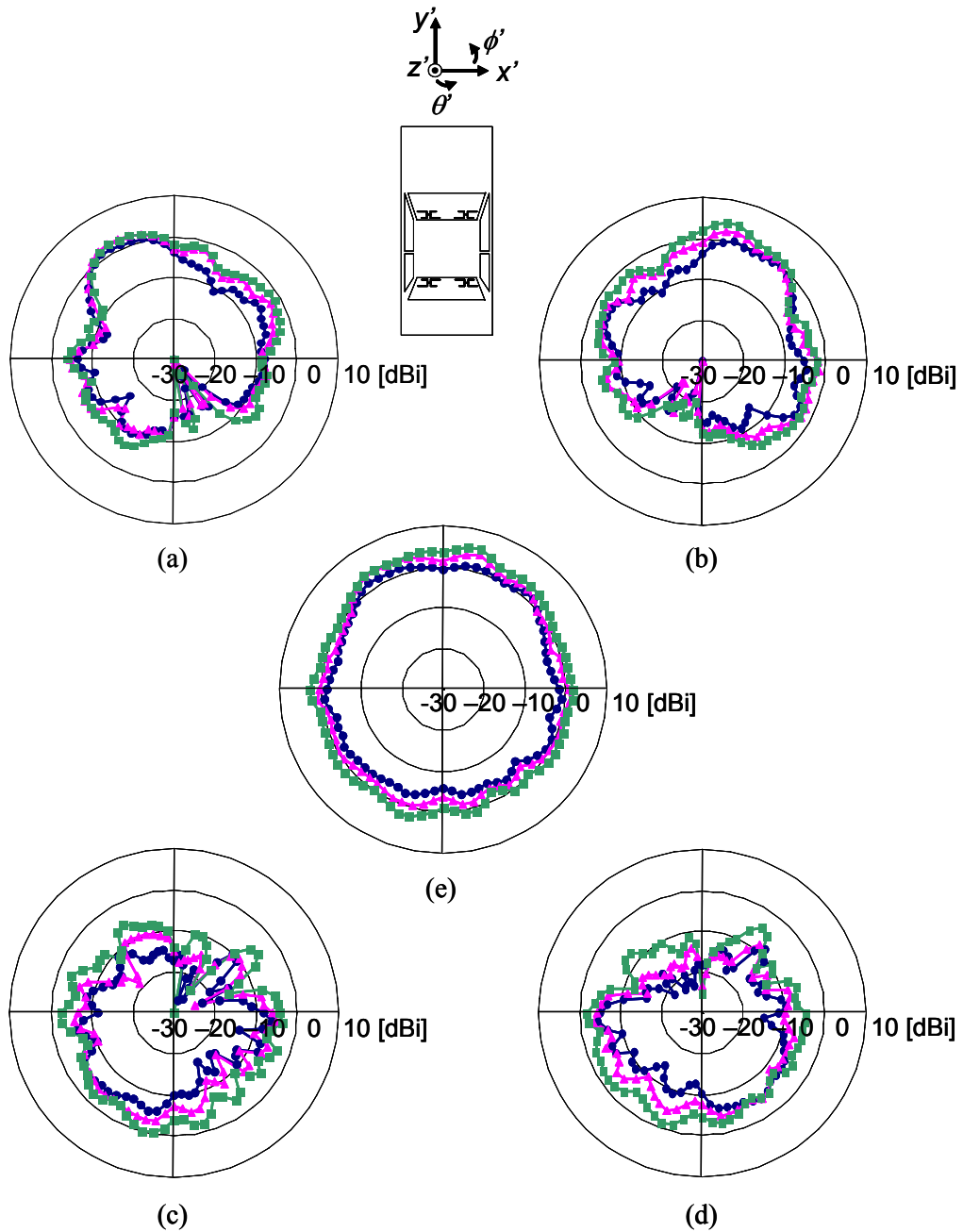


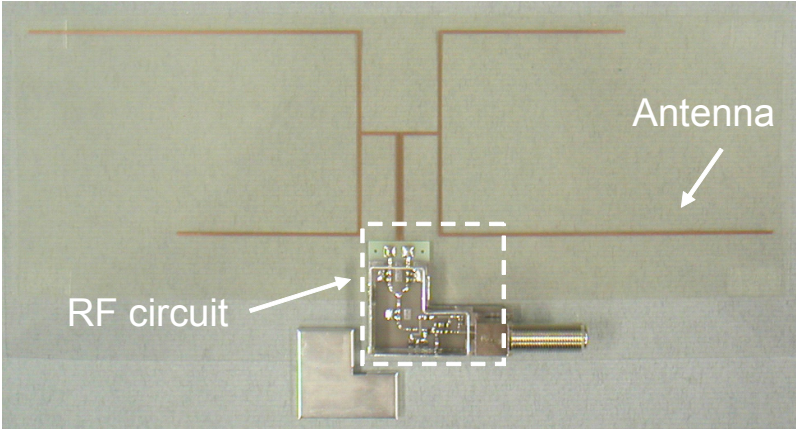
Fig. 6.11. Measured radiation patterns in the ϕ' plane at 530 MHz. Four prototype antennas were mounted at the top of the front and rear windows of a car. Peak plot of combined pattern based on the MRC method is also presented. (—●— : $\theta' = 70$ deg., —▲— : $\theta' = 80$ deg., —■— : $\theta' = 90$ deg.) (a) Front left, (b) front right, (c) rear left, (d) rear right, and (e) peak plot.

degrees, and -6 dBi for $\theta = 90$ degrees. The averaged gain calculated with the equation (6.4) also decreased from 1.8 dBi to -1.5 dBi. These values of the minimum and averaged gain are acceptable for the reception system. The peak plot of the four antennas in free space had the minimum gain of -0.2 dBi and an averaged gain of 4 dBi in the xy plane at the same frequency of 530 MHz as shown in Figure 6.7. Thus, the reductions of the minimum and averaged gain by the effect of the car body are estimated to be 5.8 dB and 5.5 dB in the horizontal plane. The measurement results indicate that the proposed antenna and concept improving the minimum gain can be applied for the car.

6.5 RF modules

Finally, a brief description of the antenna module is given. The antenna module shown in Figure 6.12 (a) consists of the modified H shaped antenna etched on a flexible substrate and an RF circuit having a balun, a filter and a Low Noise Amplifier (LNA). A relatively long RF cable is usually connected from the antenna module on the window to a receiver inside a car. The LNA contributes to improving noise figure of the RF subsystem because it reduces the effect of loss of the RF cable. The filter was put between the balun and the LNA in order to avoid saturation of the LNA. With regard to impedance matching, C/N is considered because of a receiving system. Impedance matching of the LNA for optimum noise is controlled by series and parallel reactance [6-6]. A series inductor was loaded into the LNA so that input impedance for optimum noise would be around 50Ω . The filter has characteristic impedance of 50Ω . Thus, impedance matching of the antenna module is achieved in terms of C/N since antenna impedance of 110Ω is transferred to 50Ω by the balun. The antenna module when mounted at the top of the front window is shown in Figure 6.12 (b). The antenna module was mounted in an area within 80 mm from the edge of the

metal roof.



(a)

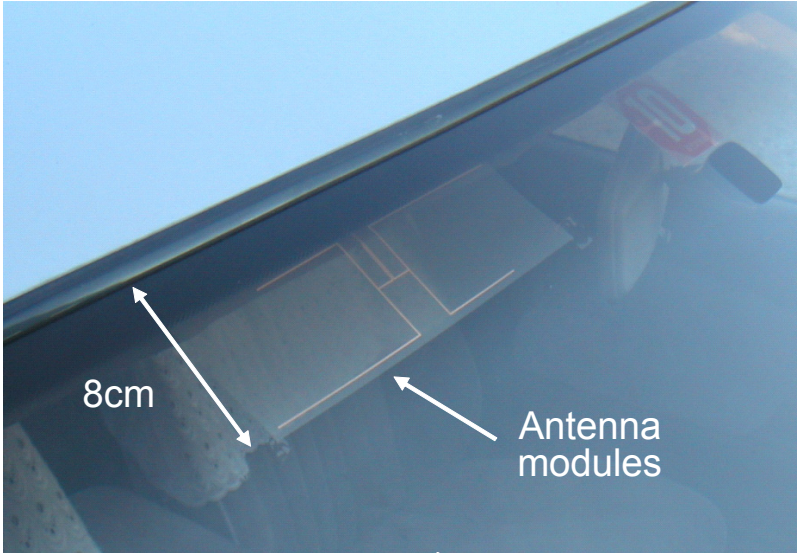


Fig. 6.12. Photographs of an antenna module. (a) Configuration of an antenna module and (b) mounted antenna module on the front window.

6.6 Conclusions

A modified H shaped antenna and a concept have been proposed for automotive digital terrestrial reception. Radiation patterns of the four symmetrically placed antennas compensate each other and cover 360 degrees. The coverage of the combined pattern of the four antennas was discussed with the peak plot, which was defined as the plotted pattern of the peak of the combined pattern. The calculation results showed that the minimum gain of the peak plot of the four antennas in free space was improved to be higher than -5.8 dBi across the frequency band from 470 MHz to 710 MHz. The effect of the angle of the antenna plane from the horizontal plane to radiation pattern has been described. The gain reduction was estimated to be -1.3 dB to the sides of the experimental car. After the validity of the analysis was confirmed by a single prototype antenna, the prototype antennas mounted on a car were measured at 530 MHz. A near omni-directional pattern of the peak plot was obtained. The minimum gain and averaged gain of the peak plot in the horizontal plane were -6 dBi and -1.5 dBi, respectively, which were acceptable values for the system. The measurement results indicated that the proposed antenna and concept improving the minimum gain were applied for the car. The proposed antennas will be utilized for automotive digital terrestrial reception.

References

- [6-1] H. Iizuka, T. Watanabe, K. Sato, and K. Nishikawa, "Modified H-shaped antenna for automotive digital terrestrial reception," *IEEE Trans. Antennas Propag.*, vol.53, no.8, pp.2542-2548, Aug. 2005.
- [6-2] H. Iizuka, T. Watanabe, K. Sato and K. Nishikawa, "Modified H shaped antenna for automotive digital terrestrial reception system", *Proc. 34th European microwave conf.*,

- pp.1253-1256, Amsterdam, Netherlands, Oct. 2004.
- [6-3] H. Iizuka, T. Watanabe, K. Sato and K. Nishikawa, “H shaped antenna for automotive digital terrestrial reception” *Proc. IEICE Gen. Conf.*, B-1-40, Tokushima, Sept., 2004.
- [6-4] W. L. Stutzman and G. A. Thiele, *Antenna theory and design*, John Wiley and Sons, 1981.
- [6-5] H. Jasik, *Antenna engineering handbook*, 1st ed., 1961.
- [6-6] L. Besser, “Stability considerations of low-noise transistor amplifiers with simultaneous noise and power match”, *IEEE MTT-S Int. Symp. Dig.*, pp.327-329, Palo Alto, CA, USA, May 1975.

Chapter 7. Digital TV antenna with thin structure

7.1 Introduction

Modified H-shaped antennas on the front and rear windows of sedans were proposed in the previous chapter. The antenna had a width of 60 mm. The development of antennas for digital TV services is still required for other types of vehicles. A thinner structure is suitable for narrower installation space near the edge of windows at the sides as well as the front and rear of vehicles. In this chapter, a folded dipole antenna with stubs is proposed [7-1]. The antenna has a thin structure with a width of 20 mm. The configuration and performance of the prototype antenna in free space are presented in Sections 7.2 and 7.3, respectively. This chapter is concluded in Section 7.4.

7.2 Proposal of stub-loaded folded dipole antenna

Figure 7.1 (a) shows a stub-loaded folded dipole antenna. The antenna has a pair of lines as stubs inside a folded dipole. The antenna has a width W of 20 mm and a length L of 240 mm. The width w_l of the lines is set at 1 mm. The frequency bandwidth can be controlled mainly by the lengths L for the lower frequencies and l_s for the higher frequencies. A prototype antenna with an RF circuit is shown in Figure 7.1 (b). The antenna was printed on polyethylene terephthalate (PET) film with a thickness of 0.125 mm. The RF circuit consists of a balun, a filter, and a low noise amplifier. It contributes to reducing the effect of cable loss between the antenna on the window and a receiver inside a vehicle.

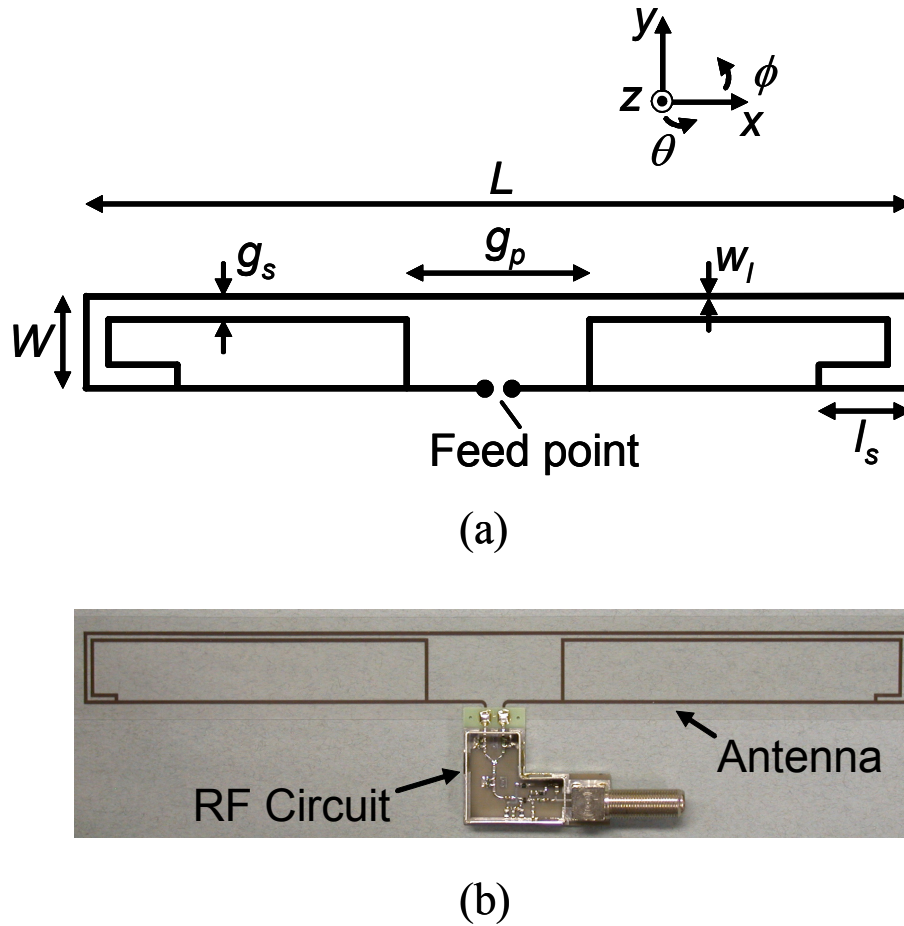


Fig. 7.1. Stub-loaded folded dipole antenna. (a) Configuration and (b) prototype. ($L = 240$ mm, $W = 20$ mm, $l_s = 9$ mm, $g_p = 40$ mm, $g_s = 2$ mm, $w_l = 1$ mm)

7.3 Performance

This section presents the measurement results of the prototype antenna through the LC balun. The LC balun transforms impedance from 200Ω to 50Ω . Figure 7.2 shows the measured VSWR of the stub loaded folded dipole antenna as a solid line. The VSWR is less than 2.6 over the frequency band from 470 MHz to 710 MHz. The measured results for a folded dipole antenna without stubs are represented as a dot-dashed line for comparison. The

comparison indicates that the stubs work in the higher frequency band. Numerical investigation was carried out by the commercial simulator “FEKO” [7-2] based on the method of moments. The calculation model was composed of wires with a radius of 0.25 mm. The lengths L and l_s were adjusted to 250 mm and 28 mm, respectively. Other parameters were the same as those of the prototype antenna. The calculated VSWR is represented by a dotted line when the antenna impedance is normalized by 200Ω . The calculated results agree with the measured results.

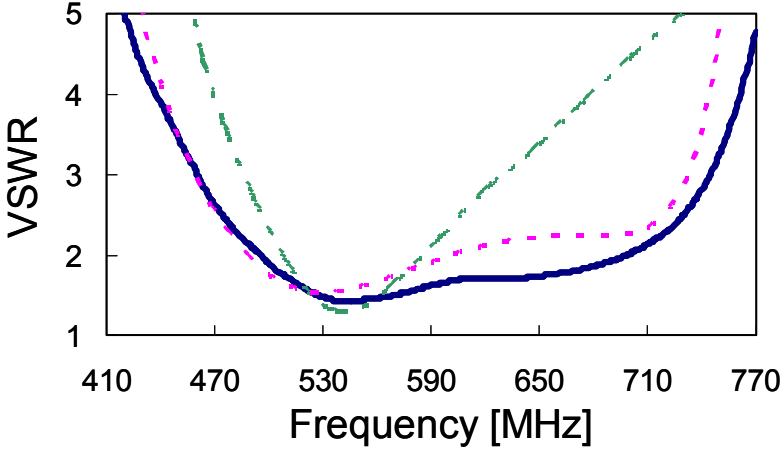


Fig. 7.2. Measured VSWR of folded dipole antennas with and without stubs. Calculated results for the stub loaded antenna are also presented. (—: stub loaded (Mea.), - - - : without stub (Mea.), - - - : stub loaded (Cal.))

The calculated current distributions at 470 MHz, 590 MHz, and 710 MHz are shown in Figure 7.3. The intensity of currents is normalized by the maximum value at each frequency. The length of the arrows represents the intensity of the currents in the range from -20 dB to 0 dB. It is observed that strong currents flow on the stubs in the higher frequency band, as

expected from the VSWR characteristics. On the other hand, the antenna works as a folded dipole antenna in the lower and middle frequency bands.

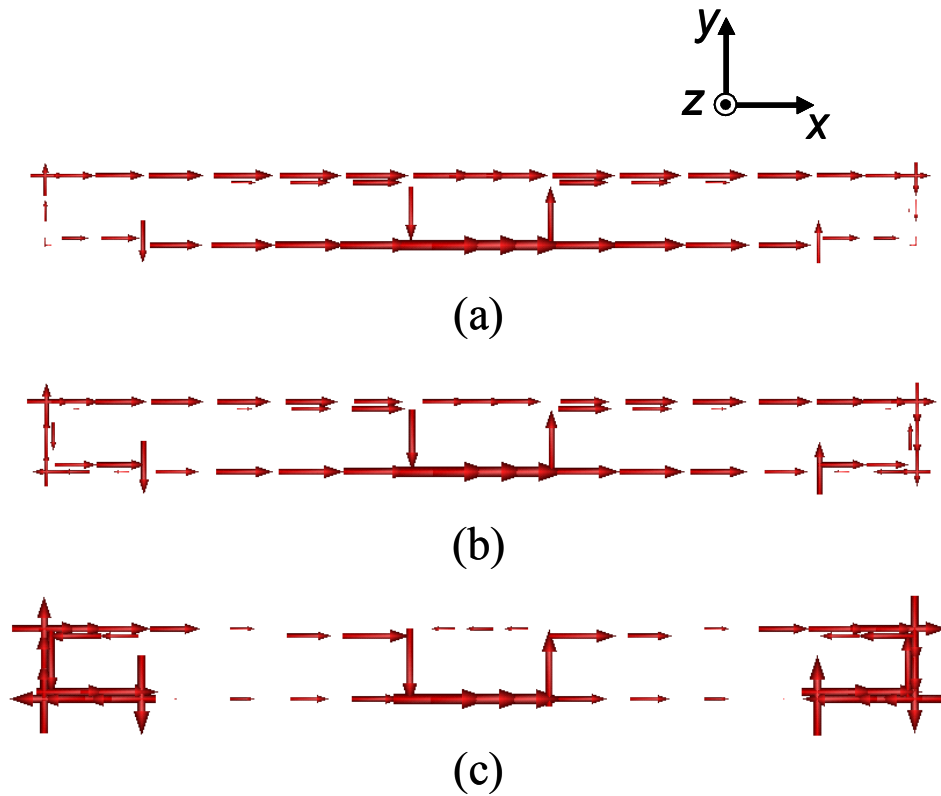


Fig. 7.3. Current distributions in the xy plane. (a) 470 MHz, (b) 590 MHz, and (c) 710 MHz. The length of the arrows represents the strength of the currents in the range from -20 dB to 0 dB.

Figure 7.4 shows the measured radiation patterns in the xz plane, which corresponds to the horizontal plane when the antenna is installed on a vertical window of a vehicle. Stable figure-of-eight radiation patterns were obtained from 470 MHz to 710 MHz.

The frequency characteristic of gain is shown in Fig. 7.5. The measured gain has a relatively flat characteristic from 0.6 dBi to 1.9 dBi in the frequency range from 470 MHz to 710 MHz. Loss of 0.3 dB for the LC balun was included.

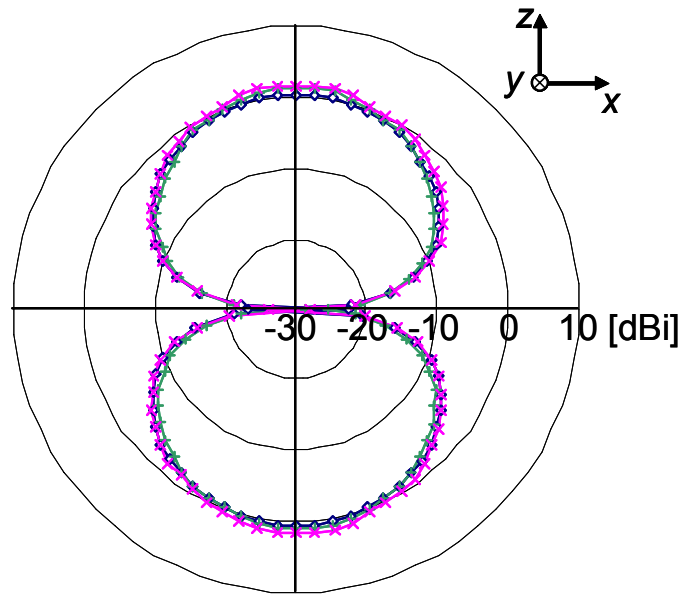


Fig. 7.4. Measured radiation patterns in the zx plane. (\diamond : 470 MHz, \times : 590 MHz, $+$: 710 MHz).

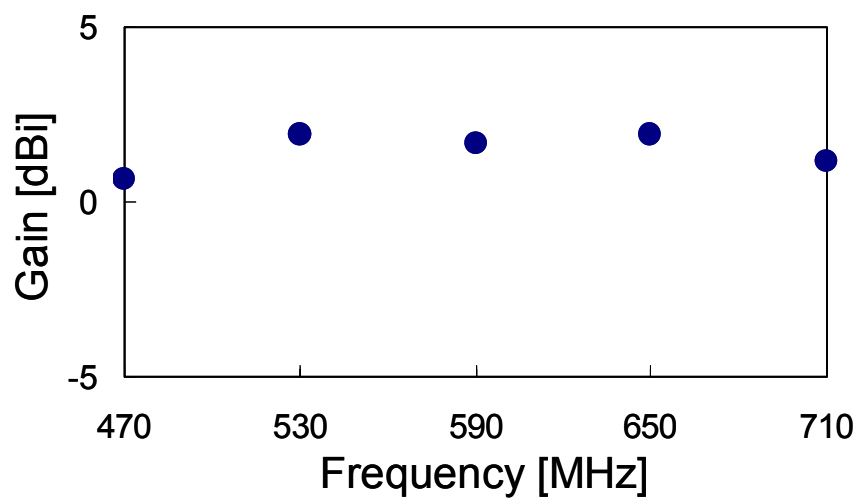


Fig. 7.5. Measured gain vs. frequency.

7.4 Conclusions

A stub-loaded folded dipole antenna has been proposed. Numerical analysis showed the stubs worked to cover the higher frequency band. It was confirmed experimentally that the antenna obtained a figure-of-eight radiation pattern and a relatively flat gain characteristic from 470 MHz to 710 MHz. The antenna, which has a thin structure of 20 mm by 240 mm, will be used for digital terrestrial TV reception on vehicles.

References

- [7-1] H. Iizuka, T. Watanabe, K. Sakakibara, and N. Kikuma, "Stub-loaded folded dipole antenna for digital terrestrial TV reception," *IEEE Antennas Wireless Propag. Lett.*, vol.5, pp.260-261, 2006.
- [7-2] FEKO user manual, suite 5.0, EM software & systems-S.A. (Pty) Ltd., Stellenbosch, South Africa, 2005.

Chapter 8. Digital TV antenna with wider bandwidth and thinner structure

8.1 Introduction

A stub-loaded folded dipole was proposed in the previous chapter. The antenna had a width of 20 mm and covered the frequency range from 470 MHz to 710 MHz. In this paper, a folded dipole having a wider bandwidth and thinner structure is proposed [8-1]. The antenna has a pair of stubs inside a folded dipole and a capacitor loaded on the folded dipole, without the use of thick lines. The antenna in free space covers the frequency range from 470 MHz to 950 MHz that is double the frequency bandwidth of the antenna described in the previous chapter. The antenna has a width of 15 mm. The configuration and performance of the antenna are described in Section 8.2 with results simulated by the method of moments. The effect of the stubs and capacitor is discussed, in comparison with dipoles, where a part of the wires and/or capacitor are removed. Measurement results of the antenna are presented in Section 8.3. The effect of the materials used in automotive body parts on antenna performance is mentioned. This chapter is then concluded in Section 8.4.

8.2 Proposal of capacitor- and stub-loaded folded dipole antenna

Figure 8.1 shows a capacitor- and stub-loaded folded dipole antenna for digital terrestrial TV reception. The antenna is composed of cylindrical wires and a lumped element capacitor. The antenna has a pair of stubs $a-g-h-i-j-b$ and $a'-g'-h'-i'-j'-b'$ inside the straight folded dipole $f-a-b-c-d-e-d'-c'-b'-a'-f$. The capacitor is loaded at the center e of the wire $d-d'$. The width W is set to 15 mm for installation into narrow spaces. The other parameters are given in Table 8.1. The design frequency of the antenna in free space is set at a bandwidth from 470 MHz to 950 MHz, which is double the bandwidth for digital terrestrial TV reception, considering the effect that the operating frequency goes down when the antenna is installed on

window glass or inside the spoiler.

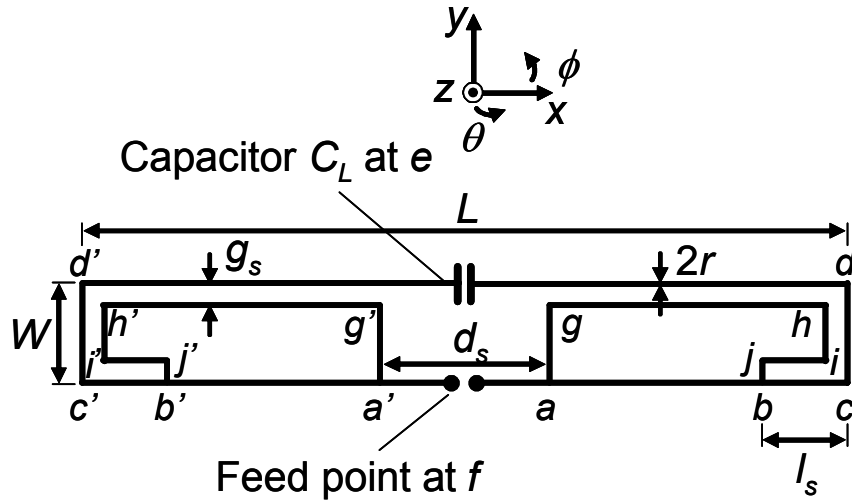


Fig. 8.1. Configuration of capacitor- and stub- loaded folded dipole antenna.

Table 8.1. Parameters of calculation model.

Length L of antenna	284 mm
Width W of antenna	15 mm
Dimension l_s of stubs	34 mm
Dimension d_s of stubs	40 mm
Dimension g_s of stubs	2 mm
Radius r of wires	0.25 mm
Capacitance of C_L	0.2 pF

8.3 Performance

The antenna of Fig. 8.1 in free space was numerically investigated by the commercial simulator “FEKO”, [8-2], which is based on the method of moments.

Calculated input impedance is shown in Fig. 8.2. The real and imaginary parts of input impedance are represented by the solid and dotted lines, respectively. Three resonant frequencies, where the imaginary part equals zero, are assigned as $f_1, f_2,$ and f_3 with increasing frequency. The resonances at $f_1 = 503$ MHz and $f_3 = 942$ MHz are series resonance, since the imaginary part goes up. While the resonance at $f_2 = 763$ MHz is antiresonance, since the imaginary part goes down.

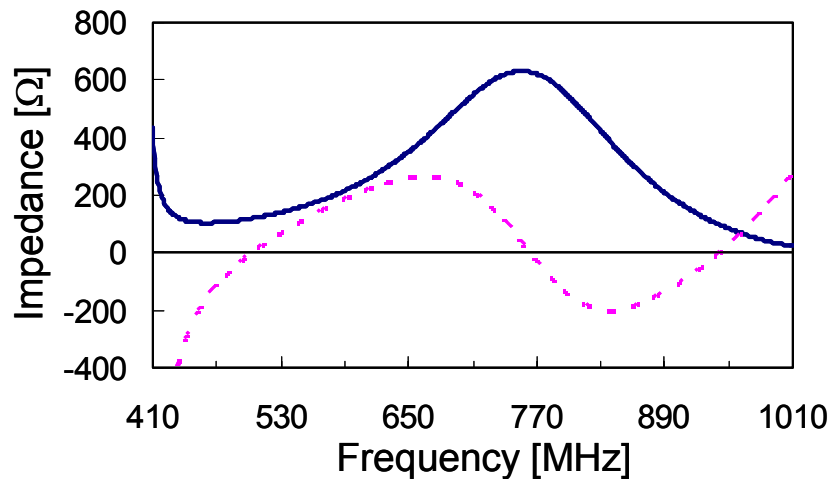


Fig. 8.2. Calculated input impedance of capacitor- and stub-loaded folded dipole antenna. (— : real, - - - : imaginary).

Figures 8.3 (a) and (b) show three resonant frequencies and input impedance with variation of capacitance of C_L . The circles, triangles, and squares represent the differences between $f_1, f_2,$ and f_3 . It can be seen in Fig. 8.3 (a) that the resonant frequency increases from 598 MHz to 811 MHz for f_2 and from 719 MHz to 998 MHz for f_3 with a decrease of C_L from

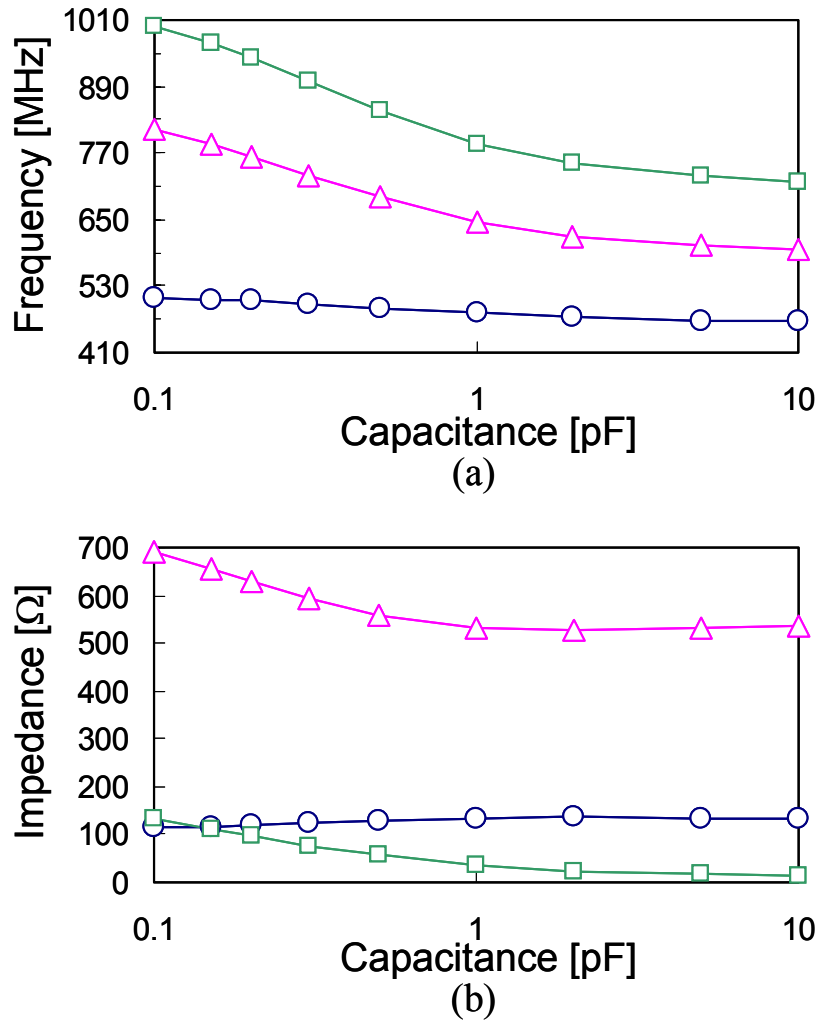







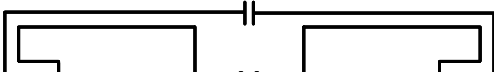
Fig. 8.3. Calculated three resonant frequencies and input impedance of capacitor- and stub-loaded folded dipole antenna with variation of capacitance of C_L . (a) Frequency vs. capacitance. (b) Impedance vs. capacitance. (\circ : f_1 , \triangle : f_2 , \square : f_3).

10 pF to 0.1 pF. The increase of the resonant frequencies corresponds to 213 MHz for f_2 and 279 MHz for f_3 . While the resonant frequency of f_1 increases by only 44 MHz from 466 MHz to 510 MHz, which is less than one sixth of the increase of f_3 . As shown in Fig. 8.3 (b), the real part of input impedance varies from 528 Ω to 691 Ω for f_2 and from 14 Ω to 132 Ω for f_3 , while it has a relatively small variation from 113 Ω to 135 Ω for f_1 . Thus, it can be

understood from Figs. 8.3 (a) and (b) that the bandwidth of the antenna can be widened by loading a capacitor. Input impedance with respect to 230Ω provides the maximum bandwidth. The increase of the real part for f_3 contributes to the wider bandwidth. But the increase of the real part for f_2 should be taken into account when the capacitance of C_L is selected.

The proposed method of bandwidth enhancement includes two aspects, stubs and a capacitor. The effects of the stubs and capacitor are analyzed in detail as follows. The antenna shown in Fig. 8.1 is compared with folded dipoles, where a part of the wires and/or capacitor are removed, as shown in Table 8.2. Their three resonant frequencies and input impedance are summarized in Figs. 8.4 (a) and (b), respectively.

Table 8.2. Configurations of six types of folded dipole antennas. Wires and/or capacitor are removed from folded dipole antenna of Fig. 8.1.

No.	Configuration
I	
II	
III	
IV	
V	
VI	

Antenna I, where both a pair of stubs and capacitor are removed, is a straight folded dipole, and has resonant frequencies of $f_1 = 481$ MHz and $f_3 = 1019$ MHz. The ratio of f_3 / f_1 is 2.12. In terms of a folded dipole that has parallel arms, antenna IV can be seen as a folded dipole having four bends of 90 degrees on its arms. These bends lead to a smaller ratio f_3 / f_1 of 1.67 (710 MHz / 425 MHz). With regard to impedance, antenna IV has a high impedance of 1483Ω for f_2 , due to antiresonance. When wires $a-b$ and $a'-b'$ are connected to antenna

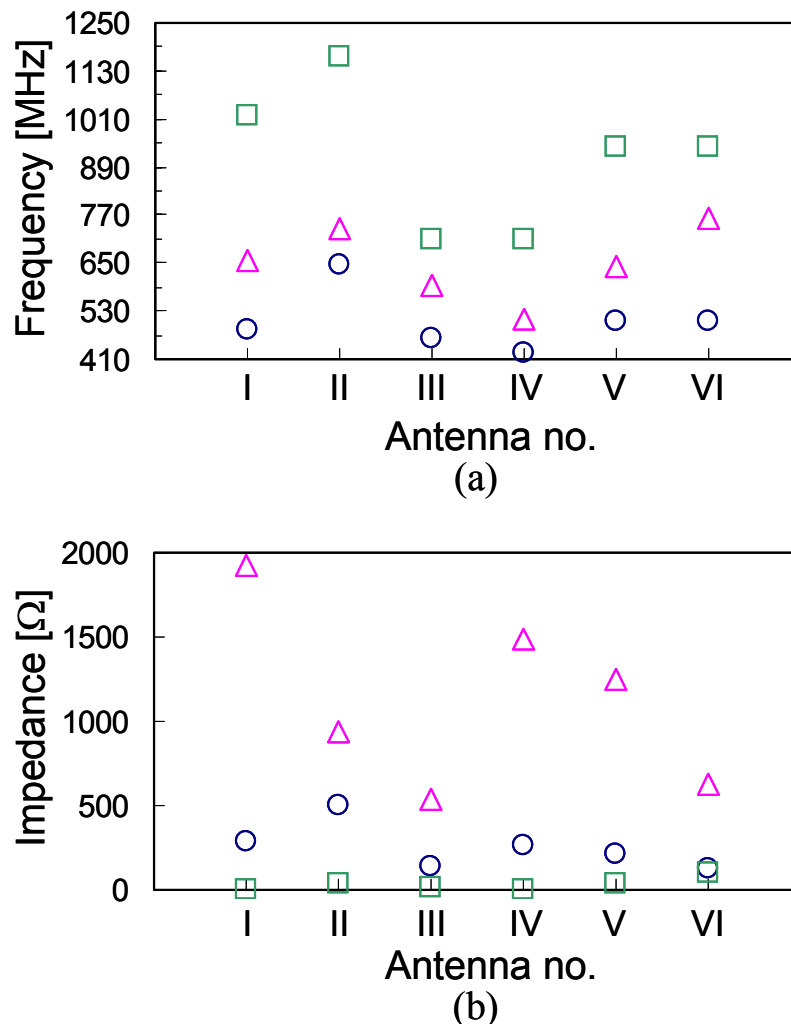


Fig. 8.4. Calculated three resonant frequencies and input impedance of six types of folded dipole antennas in Table II. (a) Frequency and (b) impedance. (○: f_1 , △: f_2 , □: f_3).

IV, which is antenna III, the impedance for f_2 is reduced to 541 Ω . This allows a wideband characteristic that has continuous resonances of f_1 , f_2 , and f_3 . Antenna III has an f_1 of 463 MHz and an f_3 of 711 MHz, which are close to the values of antenna IV. On the other hand, it can be seen from the comparison of antennas III and VI that loading a capacitor into a folded dipole with a pair of stubs leads to an increase of 231 MHz from 711 MHz to 942 MHz for f_3 , and a smaller variation of 40 MHz from 463 MHz to 503 MHz for f_1 , as mentioned before. While loading a capacitor into a folded dipole without stub increases both frequencies by 166 MHz from 481 MHz to 647 MHz for f_1 , and 148 MHz from 1019 MHz to 1167 MHz for f_3 , comparing antennas I and II. The comparison of antennas V and VI indicates that the resonant frequencies of f_1 and f_3 for the proposed antenna of Fig. 8.1 are mainly specified by the dimensions of a folded dipole having four bends $f-a-g-h-i-j-b-c-d-e-d'-c'-b'-j'-i'-h'-g'-a'-f$. This is because antennas V and VI have very close frequencies for f_1 (506 MHz and 503 MHz, respectively), and the same frequency f_3 of 942 MHz.

The antenna of Fig. 8.1 can be understood as follows from the comparison of dipoles so far. When a folded dipole has four bends of 90 degrees on its arms, the ratio f_3 / f_1 becomes smaller. The connecting wires $a-b$ and $a'-b'$ avoids unacceptably high impedance at antiresonance. Loading a capacitor increases f_3 and keeps changes in f_1 small in the case of the folded dipole with wires $a-b$ and $a'-b'$. f_1 and f_3 are mainly specified by the folded dipole having four bends. In terms of performance, it can be said that a folded dipole having four bends has a pair of stubs $a-b$ and $a'-b'$ and a capacitor, although the straight folded dipole $f-a-b-c-d-e-d'-c'-b'-a'-f$ and a pair of stubs $a-g-h-i-j-b$ and $a'-g'-h'-i'-j'-b'$ were used for the description of the antenna of Fig. 8.1 in terms of its structure.

The current distributions of the antenna of Fig. 8.1 are next analyzed. Current distributions along the x axis at $f_1 = 503$ MHz are shown in Figs. 8.5 (a)-(d). A voltage of 1

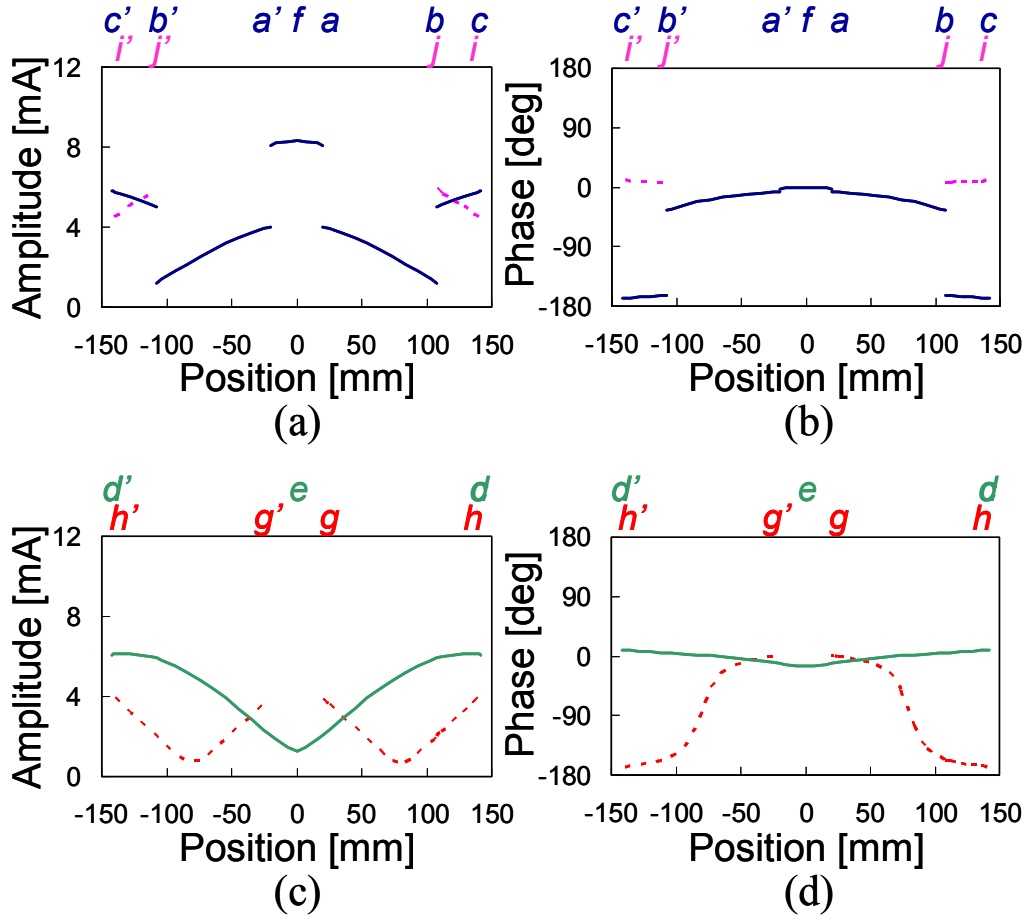


Fig. 8.5. Calculated current distributions of capacitor and stubs loaded folded dipole antenna at $f_1 = 503$ MHz. (a) Amplitude and (b) phase of currents $c'-b'-a'-f-a-b-c$ (solid line), $i'-j'$ (dotted line), and $j-i$ (dotted line). (c) Amplitude and (d) phase of currents $d'-e-d$ (solid line), $h'-g'$ (dotted line), and $g-h$ (dotted line).

V was applied at the feed point. The current of the wire from point p to point q is represented by I_{q-p} here. Figures 8.5 (a) and (b) show the amplitude and phase of current $I_{c-b-a-f-a-b-c}$ as a solid line and currents $I_{j'-i'}$ and I_{i-j} as dotted lines. In addition, Figs. 8.5 (c) and (d) show the amplitude and phase of current I_{d-e-d} as a solid line and currents $I_{g'-h'}$ and I_{h-g} as dotted lines. The focus here is the current distribution on the wires $f-a-g-h-i-j-b-c-d-e-d'-c'-b'-j'-i'-h'-g'-a'-f$ in the folded dipole having four bends. The current along the wire of the folded dipole has a standing wave with one wavelength. In

terms of the resonance of the folded dipole, the folded dipole with the current is resonated at a half wavelength. There are phase changes at + 80 mm between wire $g-h$ and at - 80 mm between wire $h'-g'$, where the amplitude reaches the minimum value of 0.7 mA. However, an ordinal straight folded dipole such as antenna I in Table II, has phase changes at both terminals. This is because the capacitor C_L makes the wire equivalently longer. The currents are also induced on wires $a-b$ and $b'-a'$. The length of the wires $a-b$ and $b'-a'$ (88 mm) is close to the length of around 73 mm from a and a' to the phase change positions between wires $g-h$ and $h'-g'$. Thus, the currents I_{j-b} and $I_{j'-b'}$ mainly come from the currents I_{b-c} and $I_{b'-c'}$ rather than I_{b-a} and $I_{b'-a'}$ at junctions b and b' . This can be seen in Fig. 8.5 (a), where the currents I_{b-a} and $I_{b'-a'}$ have a value of 1.2 mA at ± 108 mm, and the currents I_{b-c} and $I_{b'-c'}$, and I_{j-i} and $I_{j'-i'}$ have values of 5.1 mA and 5.9 mA at ± 108 mm, respectively, although the currents I_{j-b} and $I_{j'-b'}$ in the y direction are not presented. With regard to junctions a and a' , currents I_{a-f} and $I_{a'-f'}$ are equally divided into I_{b-a} and I_{g-a} , and $I_{b'-a'}$ and $I_{g'-a'}$. The currents have values of 8.1 mA for I_{a-f} and $I_{a'-f'}$, and 4 mA for I_{b-a} and $I_{b'-a'}$ at junctions a and a' . While the currents have the value of 3.9 mA at g and g' , although the currents I_{g-a} and $I_{g'-a'}$ in the y direction are not presented. It can be said from this analysis that the antenna mainly works as a folded dipole having four bends $f-a-g-h-i-j-b-c-d-e-d'-c'-b'-j'-i'-h'-g'-a'-f$ and a straight dipole $b'-a'-f-a-b$ at $f_1 = 503$ MHz.

The current distributions at $f_2 = 763$ MHz are shown in Figs. 8.6 (a)-(d). The formats of Figs. 8.6 (a)-(d) are the same as those of Figs. 8.5 (a)-(d) except for the range of amplitude from 0 to 3 mA in Figs. 8.6 (a) and (c). The amplitude of currents at $f_2 = 763$ MHz is smaller than that at $f_1 = 503$ MHz due to antiresonance. It can be seen in Fig. 8.6 (a) that the currents I_{a-b} and $I_{a'-b'}$ vary from 1 mA to 1.3 mA. On the other hand, the currents I_{j-i} and I_{h-g} , and $I_{j'-i'}$ and $I_{h'-g'}$ are within a variation range from 0.6 mA to 1 mA as shown in Figs. 8.6 (a) and (c). The current distributions indicate that the currents I_{a-b} and $I_{a'-b'}$ are higher than the currents

$I_{b-j-i-h-g-a}$ and $I_{b'-j'-i'-h'-g'-a'}$, and avoid the unacceptably high impedance of antenna V, as seen from the comparison of antennas V and VI. It can be said from this analysis that the antenna mainly works as a straight folded dipole $f-a-b-c-d-e-d'-c'-b'-a'-f$ rather than a folded dipole having four bends $f-a-g-h-i-j-b-c-d-e-d'-c'-b'-j'-i'-h'-g'-a'-f$ at $f_2 = 763$ MHz.

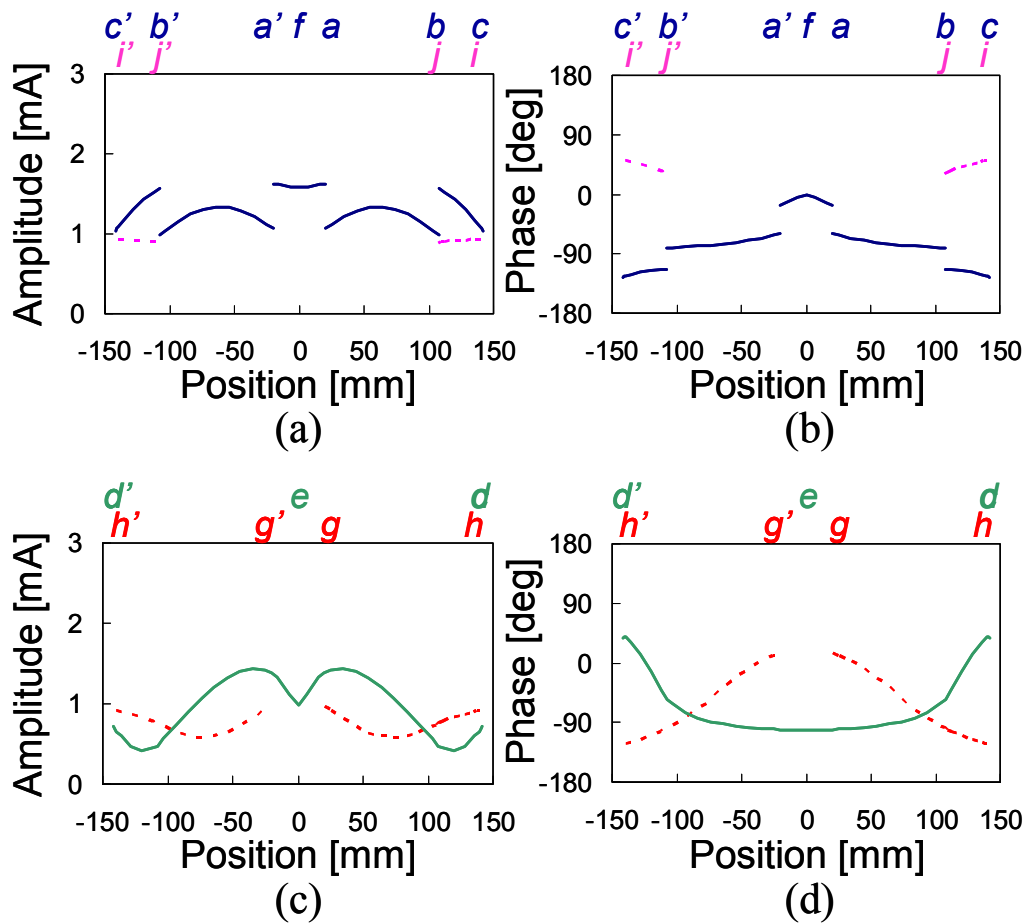


Fig. 8.6. Calculated current distributions of capacitor- and stub-loaded folded dipole antenna at $f_2 = 763$ MHz. (a) Amplitude and (b) phase of currents $c'-b'-a'-f-a-b-c$ (solid line), $i'-j'$ (dotted line), and $j-i$ (dotted line). (c) Amplitude and (d) phase of currents $d'-e-d$ (solid line), $h'-g'$ (dotted line), and $g-h$ (dotted line).

The current distributions at $f_3 = 942$ MHz are shown in Figs. 8.7 (a)-(d). The formats of Figs. 8.7 (a)-(d) are the same as those of Figs. 8.5 (a)-(d). The folded dipole having four bends $f-a-g-h-i-j-b-c-d-e-d'-c'-b'-j'-i'-h'-g'-a'-f$ has a standing wave with two wavelengths, and is resonated at one wavelength. It can be seen in Fig. 8.7 (c) that the currents have the minimum values of 0.6 mA at ± 120 mm on wires $e-d$ and $e'-d'$, and 0.9 mA at ± 94 mm on wires $g-h$ and $g'-h'$ with phase changes. The currents I_{a-b} and $I_{a'-b'}$ are smaller than those of the folded dipole having four bends at $f_3 = 942$ MHz, rather than $f_1 = 503$ MHz. Thus, it can

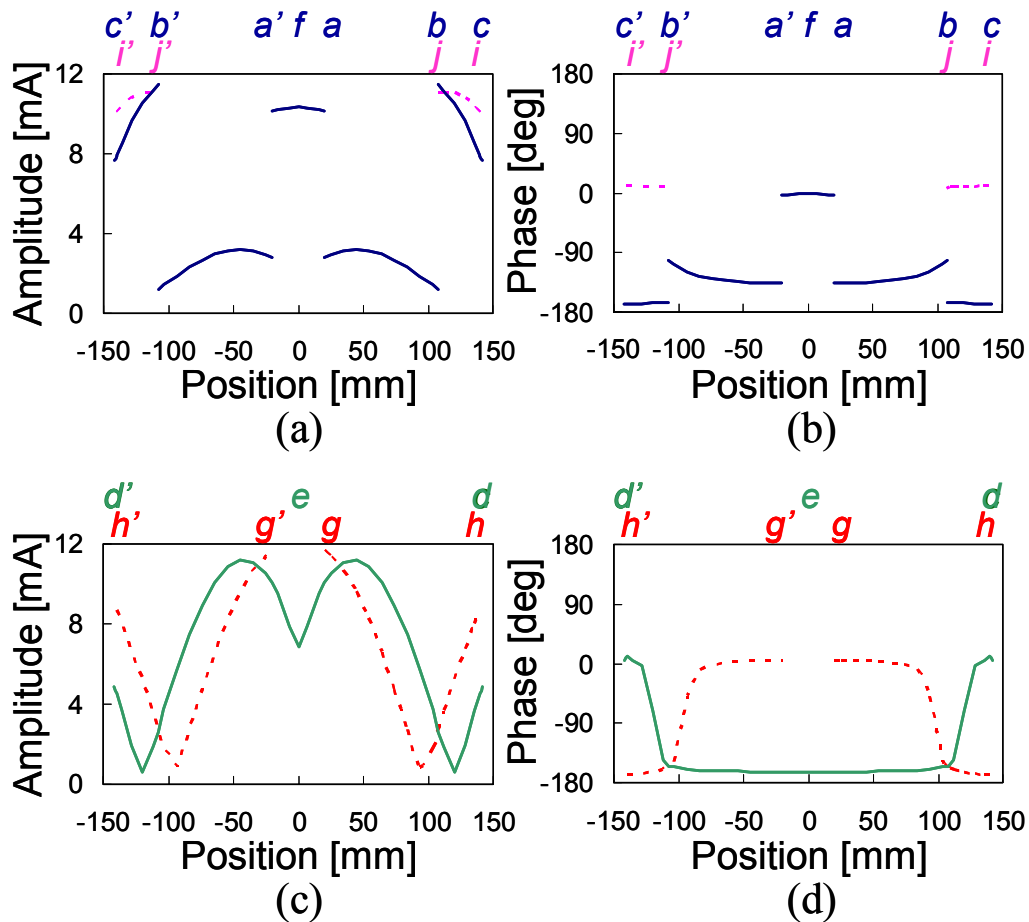


Fig. 8.7. Calculated current distributions of capacitor- and stub-loaded folded dipole antenna at $f_3 = 942$ MHz. (a) Amplitude and (b) phase of currents $c'-b'-a'-f-a-b-c$ (solid line), $i'-j'$ (dotted line), and $j-i$ (dotted line). (c) Amplitude and (d) phase of currents $d'-e-d$ (solid line), $h'-g'$ (dotted line), and $g-h$ (dotted line).

be said that the antenna mainly works as a folded dipole having four bends $f-a-g-h-i-j-b-c-d-e-d'-c'-b'-j'-i'-h'-g'-a'-f$ at $f_3 = 942$ MHz.

In the case of the width W being much smaller than a free space wavelength, no phase difference of the paths is assumed in the far field radiated from the currents in Figs. 8.5, 8.6, and 8.7. Here, the radiation source becomes the summation of the currents. Figures 8.8 (a) and (b) show the amplitude and phase of the summation of the currents along the x axis. The solid, dotted, and dot-dashed lines represent the summation of the currents at 503 MHz, 763 MHz, and 942 MHz, respectively. It can be seen in Fig. 8.8 (a) that the amplitude has one peak at 503 MHz, and two peaks at 763 MHz and 942 MHz, where the positions of the peaks move outward from the feed point with increasing frequency. As shown in Fig. 8.8 (b), the phase has a flat distribution at 503 MHz. Although the difference of phases of positions between the maximum amplitude and the feed point increases with increases in frequency, the phases have the same values with a nearly flat distribution around the positions of the two maximum amplitudes at 763 MHz and 942 MHz. Thus, the antenna of Fig. 8.1 is expected to have stable figure-of-eight radiation patterns in the xy and zx planes in the frequency range from 470 MHz to 950 MHz.

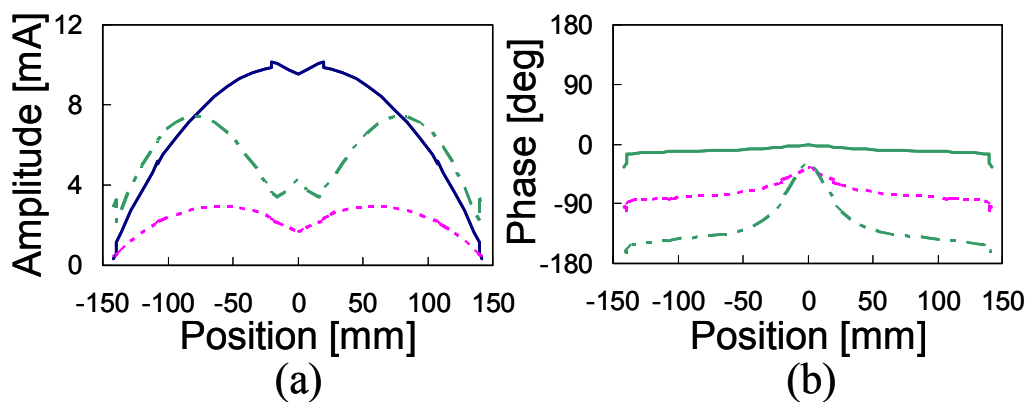


Fig. 8.8. Summation of currents along the x axis. (—: $f_1 = 503$ MHz, - - - : $f_2 = 763$ MHz, - · - · : $f_3 = 942$ MHz.) (a) Amplitude and (b) phase.

8.4 Prototype antenna

The antenna in free space was experimentally investigated in a frequency range from 470 MHz to 950 MHz to verify the numerical investigation presented in Section 8.3. The effect of the materials of automotive body parts on resonant frequency is also discussed below in terms of the digital terrestrial TV band.

Figure 8.9 shows a prototype antenna printed on PET film with a thickness of 0.125 mm. The cylindrical wires and lumped element capacitor of Fig. 8.1 were implemented with lines and a slit on the line for ease of fabrication. The lines have a width of 1 mm. The slit has a length l_{sl} of 4 mm along the x axis, and a width w_{sl} of 0.06 mm. The parameters of L and l_s were experimentally adjusted to 280 mm and 18 mm, maintaining an antenna width W of 15 mm. Other parameters are the same as those presented in Table 8.1. Thus, the prototype antenna has dimensions of 15 mm by 280 mm with a line width of 1 mm.

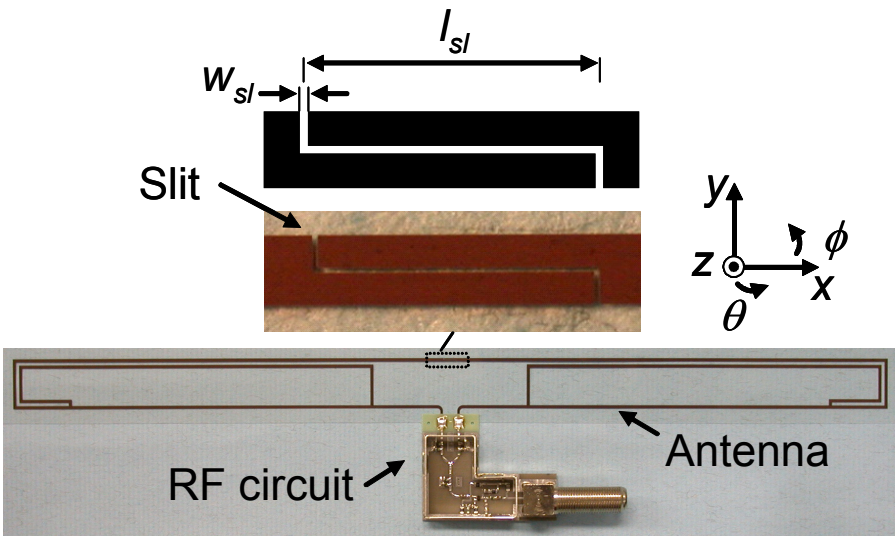


Fig. 8.9. Prototype antenna.

The RF circuit connected at the feed point of the antenna consists of a balun, a filter, and a low noise amplifier (LNA). The LNA contributes to improving the noise figure of the RF subsystem, reducing the effect of loss from the RF cables between an antenna on a window glass or inside the spoiler, and a receiver inside the vehicle. The LNA has a series inductor so that the input impedance for the minimum noise may be adjusted to around 50Ω . The filter was inserted between the LNA and balun to avoid saturation of the LNA. The balun consists of a high pass filter, low pass filter, and T junction, and both filters have a 5th order Butterworth function to cover the frequency range from 470 MHz to 710 MHz. The balun transforms impedance from 230Ω for the balanced port to 50Ω for the unbalance port. In terms of C/N, impedance matching can be achieved in the prototype antenna with the RF circuit.

A balun having a wider bandwidth characteristic was built to enable measurement of the antenna. Figure 8.10 shows a diagram of the balun. The balun has the same impedance of Z_b

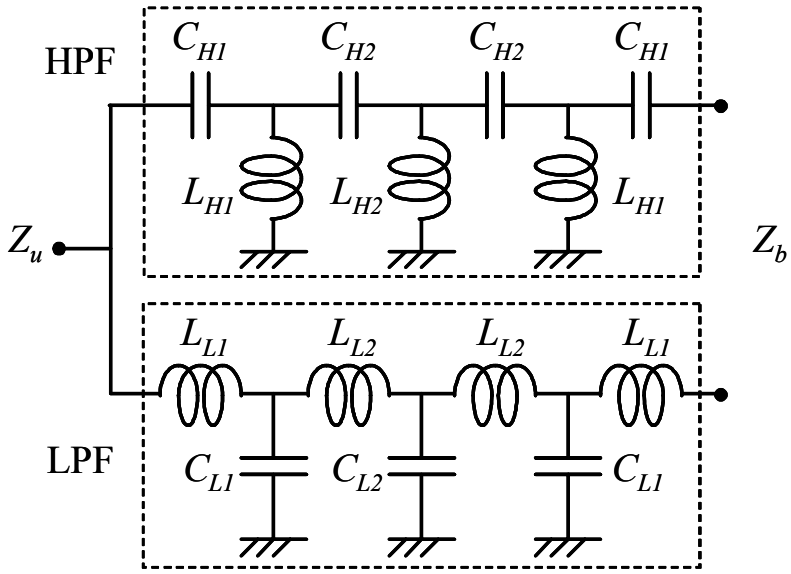


Fig. 8.10. Diagram of balun for measurement from 470 MHz to 950 MHz.

= 230Ω and $Z_u = 50 \Omega$, but a 7th order Butterworth function to cover a wider bandwidth from 470 MHz to 950 MHz. The balun has parameters of $C_{H1} = 15$ pF, $C_{H2} = 3$ pF, $L_{H1} = 56$ nH, $L_{H2} = 33$ nH, $C_{L1} = 1$ pF, $C_{L2} = 1.5$ pF, $L_{L1} = 3.9$ nH, and $L_{L2} = 15$ nH.

Figure 8.11 shows the measured transmission coefficient of the balun. The balun has loss from 0.3 dB to 0.6 dB in the frequency range from 470 MHz to 950 MHz. In this measurement, the device under test (DUT) was composed of two baluns with connected balanced ports. The transmission coefficient of the DUT was measured between the unbalanced ports. The transmission coefficient divided by two provides that of a single balun in Fig. 8.11.

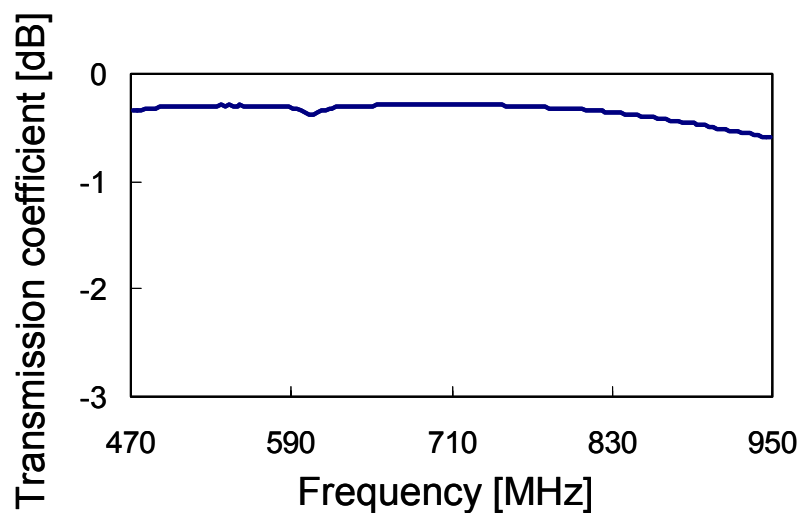


Fig. 8.11. Measured transmission coefficient of balun.

The Voltage Standing Wave Ratio (VSWR) is presented in Fig. 8.12. The measurement and calculation results are represented by the solid and dotted lines, respectively. The measured VSWR of the antenna through the balun is less than 2.6 from 470 MHz to 950 MHz, while the calculated VSWR of the antenna with respect to 230Ω is less than 2.8. The measurement result agrees with the calculation result.

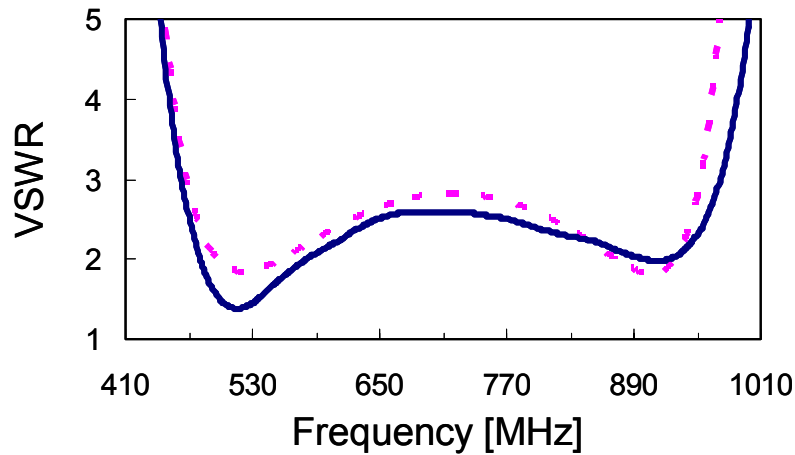


Fig. 8.12. VSWR of capacitor- and stub-loaded folded dipole antennas.
(—: mea., - - - : cal.)

Figures 8.13 (a)-(j) show normalized radiation patterns from 470 MHz to 950 MHz with a step of 120 MHz. The xy planes are presented in Figs. 8.13 (a), (c), (e), (g), and (i), while the zx planes in Figs. 8.13 (b), (d), (f), (h), and (j). The xy and zx planes correspond to the horizontal plane when the antenna is installed inside a horizontal spoiler or on a vertical window of a vehicle. The measurement and calculation results are represented by the dots and lines, respectively. It can be seen in Figs. 8.13 (a)-(j) that the antenna has stable figure-of-eight radiation patterns in both xy and zx planes from 470 MHz to 950 MHz. The measurement results agree with the calculation results. A little difference is seen in the radiation patterns at 950 MHz in Figs. 8.13 (i) and (j). This may be caused by a characteristic of the balun, since loss of the balun slightly degraded in the higher frequency band, where the balun loss of 0.6 dB at 950 MHz includes not only the consumption of the resistance components of the LC elements and reflection loss caused by impedance mismatching, but also the amplitude difference of the induced voltages at the balanced ports connected to the feed point of the antenna.

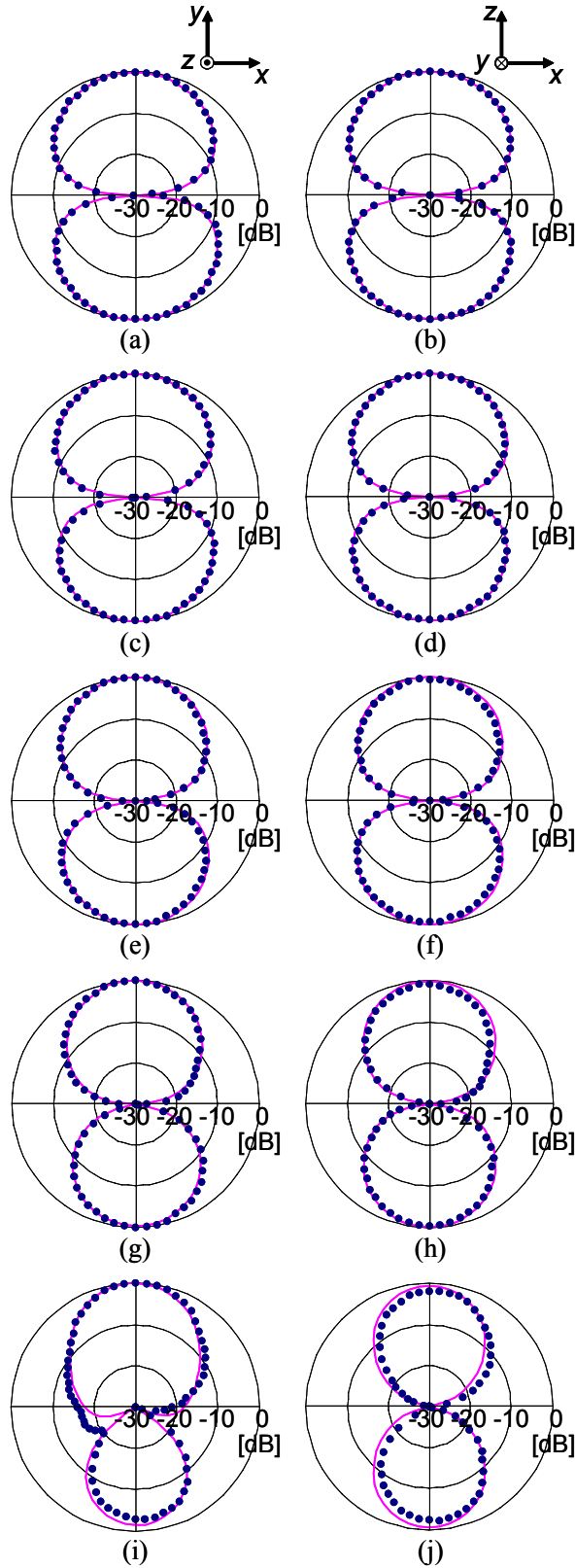


Fig. 8.13. Normalized radiation patterns of capacitor- and stub-loaded folded dipole antennas. (●: mea., —: cal.) (a) 470 MHz, xy -pl. (b) 470 MHz, zx -pl. (c) 530 MHz, xy -pl. (d) 530 MHz, zx -pl. (e) 710 MHz, xy -pl. (f) 710 MHz, zx -pl. (g) 830 MHz, xy -pl. (h) 830 MHz, zx -pl. (i) 950 MHz, xy -pl. (j) 950 MHz, zx -pl.

Figure 8.14 shows the frequency characteristic of the measured gain. The measured gain goes up slightly as the frequency increases. The measured gain varies from 0.7 dBi to 2.5 dBi in the frequency range from 470 MHz to 950 MHz. Loss of the balun is included.

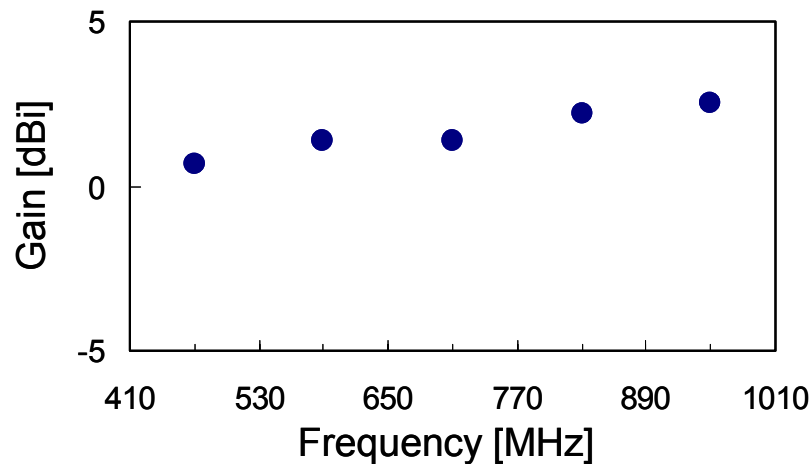


Fig. 8.14. Measured gain of prototype antenna.

The effects of the materials of automotive body parts on shifts in operating frequency are finally investigated. The prototype antenna was attached to two typical flat plates with dimensions of 300 mm by 300 mm. One was glass with a thickness of 4 mm to represent a window. The other was thermoplastic Acrylonitrile Butadiene Styrene (ABS) with a thickness of 3 mm to represent a spoiler. Figure 8.15 shows the measured VSWR for both cases. The measured VSWR remains less than 2.7 from 470 MHz to 710 MHz in both cases, although the operating frequency goes down. It can be said that the proposed antenna has a sufficiently wide bandwidth for digital terrestrial TV reception, even when the operating frequency goes down due to the effects of typical materials used in automotive body parts.

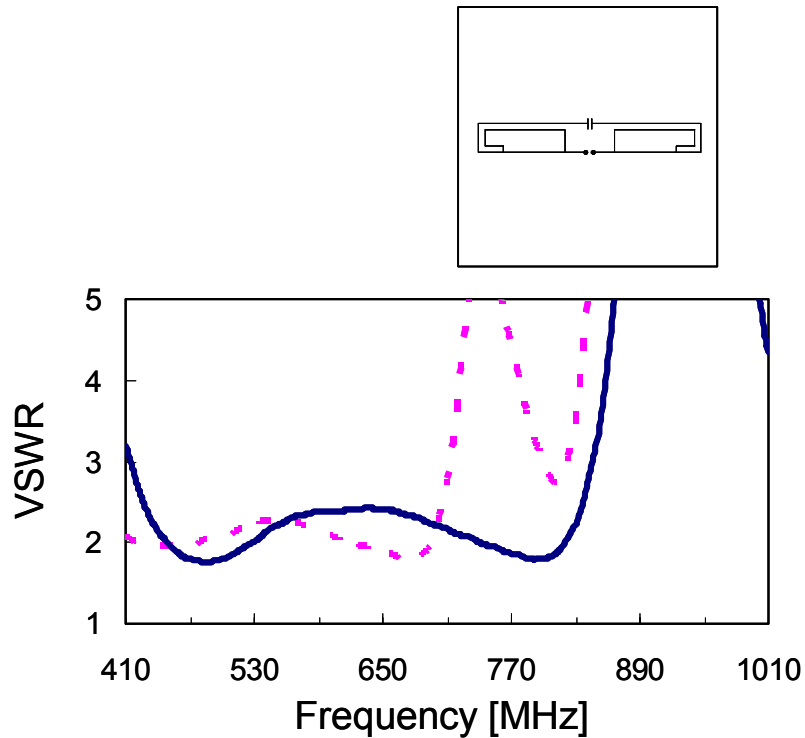


Fig. 8.15. Measured VSWR of prototype antennas attached to materials having dimensions of 300 mm by 300 mm. (—: thermoplastic ABS used for spoiler, - - - : glass used for window).

8.5 Conclusions

A stub- and capacitor-loaded folded dipole antenna has been proposed for digital terrestrial TV reception. A numerical investigation clarified the effects of the stub and capacitor on bandwidth enhancement. The prototype antenna in free space showed a VSWR of less than 2.6 and gain from 0.7 dBi to 2.5 dBi in a frequency range from 470 MHz to 950 MHz. The VSWR remained less than 2.7 in the digital terrestrial TV band from 470 MHz to 710 MHz even when the antenna was attached to typical materials used in vehicles.

The proposed antenna that has the advantages of a thin structure of 15 mm by 280 mm, sufficiently wide bandwidth, and ease of fabrication, will be used for digital terrestrial TV reception on vehicles.

References

- [8-1] H. Iizuka, K. Sakakibara, and N. Kikuma, "Capacitor- and stub-loaded folded dipole antenna for digital terrestrial TV reception," *IEEE Trans. Antennas Propag.*, in review process (Conditionally accepted).
- [8-2] *FEKO user manual, suite 5.0*, EM software & systems-S.A. (Pty) Ltd., Stellenbosch, South Africa, 2005.

Chapter 9. Conclusions

In this doctoral dissertation, automotive antenna design techniques were investigated analytically, numerically, and experimentally, particularly, in the highest and nearly the lowest edges of the frequency bands assigned for automotive wireless systems. Considering the impact on industry, millimeter-wave radar system and digital terrestrial TV reception system in UHF band were focused on.

A new configuration of millimeter-wave microstrip antenna has been proposed. Two types of antennas were developed. A fan beam antenna showed an aperture efficiency of 53 % with a gain of 22.5 dBi at 76.5 GHz. A pencil beam antenna using a two-stage feed circuit showed an aperture efficiency of 39 % with a gain of 32.2 dBi at 76.5 GHz. The developed antennas have higher efficiencies compared with those of conventional microstrip antennas. The antenna will be used near future as the number of installation of radar systems increases.

A new transition from waveguide to microstrip line has been proposed. The transition has a simple structure, and does not need a conventional metal short block nor additional substrate. The transition showed a measured transmission loss of 0.4 dB. A wideband design methodology has also been proposed. The bandwidth increased by 1.2 times, using optimum dimensions of rectangular patch element in waveguide. A transition working as a divider showed a measured insertion loss of 0.5 dB. The proposed transition will be used with microstrip antennas since it contributes to low cost connection between microstrip antennas and a sensor head.

A technique of omnidirectional pattern synthesis has been proposed for digital TV reception. The calculation results showed that the minimum gain of the peak plot of the four H shaped antennas in free space was improved to be higher than -5.8 dBi across the frequency band from 470 MHz to 710 MHz. Four prototype antennas mounted at the front and rear

windows gave a near omnidirectional pattern of the peak plot at 530 MHz. The antennas will be used for sedans.

Thin structured antennas were developed. A stub-loaded folded dipole having 20 mm by 240 mm had a VSWR less than 2.6 from 470 MHz to 710 MHz. Loading a capacitor as well as stubs into a folded dipole leads to a wider bandwidth, where the VSWR is less than 2.6 from 470 MHz to 950 MHz. The antennas will be used for vehicles that have narrow installation spaces.

This doctoral dissertation described key technologies of novel automotive antennas in the millimeter-wave and UHF bands. The investigations of the two frequency bands would provide useful design insights of automotive antennas in wide frequency range. I believe that the investigations in this dissertation contribute to the advancements for automotive antenna design techniques in both academic and industrial points of view.

Acknowledgement

I would like to express my utmost gratitude to my supervisor, Professor Nobuyoshi Kikuma at Nagoya Institute of Technology for their patience, advice, and continuous support through this study. I have learned a lot in his laboratory where researches have been actively carried out. I would like to thank Associate Professor Kunio Sakakibara at Nagoya Institute of Technology for fruitful discussion on millimeter-wave antennas and circuits. I would like to thank Professor Peter S Hall at the University of Birmingham for his advices through another project of left-handed antennas, and Professor Misao Haneishi and Professor Takaaki Hasegawa at Saitama University for their advices during fundamental study of antennas.

Also, I would like to thank my bosses in Toyota Central Research & Development Labs., Inc., Dr. Kunitoshi Nishikawa, a director, Dr. Kazuo Sato, a head of section, and Mr. Toshiaki Watanabe, a team leader, for fruitful discussions and providing the opportunity of this study. Through the development of the two systems, I would like to thank Dr. Kazuyoshi Asano for discussion on radar systems and Dr. Nobuo Itoh for discussion on digital TV reception systems. I would like to thank Dr. Shin-ichiro. Matsuzawa, Mr. Shinya Sugiura, and other colleagues in Toyota Central Research & development Labs., Inc., and Assistant Professor Hiroshi Hirayama, Mr. Tsuneo Umemura, and students in Nagoya Institute of Technology for their advices and supports.

I would like to express my warmest gratitude to my father, Shigeo, and mother, Yoshiko, and brother, Hiroshi, for bringing up me with educational environments. Finally, I would like to greatly thank my wife, Mutsumi, for her understanding, encouragement and support, and son, Haru, for refreshing me.

List of publications

1. Journals

1.1 Journals arising from this dissertation (4 papers and 1 letter)

- [1-1] H. Iizuka, K. Sakakibara, and N. Kikuma, "Millimeter-wave transition from waveguide to two microstrip lines using rectangular patch element," *IEEE Trans. Microwave Theory Tech.*, vol.55, no.5, pp. 899-905, May. 2007.
- [1-2] H. Iizuka, T. Watanabe, K. Sakakibara, and N. Kikuma, "Stub-loaded folded dipole antenna for digital terrestrial TV reception," *IEEE Antennas Wireless Propag. Lett.*, vol.5, pp.260-261, 2006.
- [1-3] H. Iizuka, T. Watanabe, K. Sato, and K. Nishikawa, "Modified H-shaped antenna for automotive digital terrestrial reception," *IEEE Trans. Antennas Propag.*, vol.53, no.8, pp.2542-2548, Aug. 2005.
- [1-4] H. Iizuka, T. Watanabe, K. Sato, and K. Nishikawa, "Millimeter-wave microstrip array antenna for automotive radars," *IEICE Trans. Commun.*, vol.E86-B, no.9, pp.2728-2738, Sept. 2003.
- [1-5] H. Iizuka, T. Watanabe, K. Sato, and K. Nishikawa, "Millimeter-wave microstrip line to waveguide transition fabricated on a single layer dielectric substrate," *IEICE Trans. Commun.*, vol.E85-B, no.6, pp.1169-1177, Jun. 2002.

1.2 Other journals (2 papers & 2 letters)

- [1-6] H. Iizuka and P. S. Hall, "Left-handed dipole antennas and their implementations," *IEEE Trans. Antennas Propag.*, vol.55, no.5, pp. 1246-1253, May. 2007.
- [1-7] H. Iizuka, P. S. Hall, and A. L. Borja, "Dipole antenna with left-handed loading," *IEEE Antennas Wireless Propag. Lett.*, vol.5, pp.483-485, 2006.
- [1-8] S. Sugiura and H. Iizuka, "Reactively steered ring antenna array for automotive application," *IEEE Trans. Antennas Propag.*, vol.55, no.7, Jul. 2007, (Accepted).

- [1-9] A. L. Borja, P. S. Hall, Q. Liu, and H. Iizuka, "Omnidirectional loop antenna with left-handed loading," *IEEE Antennas Wireless Propag. Lett.*, vol.6, 2007, (Accepted).

1.3 Journal in review process (1 paper)

- [1-10] H. Iizuka, K. Sakakibara, and N. Kikuma, "Capacitor- and stub-loaded folded dipole antenna for digital terrestrial TV reception," *IEEE Trans. Antennas Propag.*, (Conditionally accepted).

2. International conferences

2.1 International conferences arising from this dissertation (3)

- [2-1] H. Iizuka, T. Watanabe, K. Sato and K. Nishikawa, "Modified H shaped antenna for automotive digital terrestrial reception system", *Proc. 34th Euro. Microwave Conf.*, Amsterdam, Holland, Oct. 2004.
- [2-2] H. Iizuka, T. Watanabe, K. Sato and K. Nishikawa, "Study of modified H shaped antenna for digital terrestrial reception system", *Int. Symp. Ant. Propag. 2004*, Sendai, Japan, Aug. 2004.
- [2-3] H. Iizuka, T. Watanabe, K. Sato and K. Nishikawa, "Millimeter-wave microstrip array antenna for automotive radar systems", *Int. Symp. Ant. Propag. 2000*, pp.456-468, Fukuoka, Japan, Aug. 2000.

2.2 Other international conferences (5)

- [2-4] H. Iizuka and P. S. Hall, "Orthogonally polarised dipole antenna using left handed transmission lines" *Proc. 36th Euro. Microwave Conf.*, pp.1048-1051, Manchester, UK, Sept. 2006.
- [2-5] H. Iizuka and P. S. Hall, "Omnidirectional left-handed loop antenna," *IEEE Antennas Propag. Soc. Int. Symp. Dig.*, vol.1, pp.27-30, Alberquaky, NM, Jul. 2006.
- [2-6] H. Iizuka and P. S. Hall, "A left-handed dipole concept," *Proc. Int. Workshop on*

Antenna Tech., pp.396-399, White plains, NY, Mar. 2006.

- [2-7] H. Iizuka and M. Haneishi, "Dual-polarized array antenna composed of triplate-type tapered slot antennas" *IEEE Antennas Propag. Soc. Int. Symp. Dig.*, vol. 3, pp. 1413-1416, Waltham, MA, Jun. 1998.
- [2-8] H. Iizuka and M. Haneishi, "Radiation properties of triplate-type tapered slot antennas," *IEEE Antennas Propag. Soc. Int. Symp. Dig.*, vol. 3, pp. 1916-1919, Baltimore, MD, Jul. 1996.

3. Domestic conferences

3.1 Domestic conferences arising from this dissertation (4)

- [3-1] H. Iizuka, T. Watanabe, K. Sato and K. Nishikawa, "H shaped antenna for automotive digital terrestrial reception" *Proc. IEICE Gen. Conf.*, B-1-40, Tokushima, Sept. 2004.
- [3-2] H. Iizuka, K. Sakakibara, T. Watanabe, K. Sato and K. Nishikawa, "Antennas for automotive millimeter-wave radar systems" *Proc. IEICE Gen. Conf.*, SB-1-7, Kusatsu, Mar. 2001.
- [3-3] H. Iizuka, T. Watanabe, K. Sato and K. Nishikawa, "76GHz-band microstrip array antenna for automotive radar systems" *Proc. IEICE Soci. Conf.*, B-1-156, Nagoya, Sept. 2000.
- [3-4] H. Iizuka, T. Watanabe, K. Sato and K. Nishikawa, "Microstrip line to waveguide transition in millimeter-wave band" *Proc. IEICE Gen. Conf.*, B-1-135, Hiroshima, Mar. 2000.

3.2 Other domestic conferences (8)

- [3-5] H. Iizuka and P. S. Hall, "Left-handed dipole and loop antennas," *Proc. IEICE Gen. Conf.*, BS-1-8, Nagoya, Mar. 2007.
- [3-6] H. Iizuka and P. S. Hall, "A concept for left-handed dipole antennas," *Proc. IEICE Gen.*

- Conf.*, B-1-150, Tokyo, Mar. 2006.
- [3-7] H. Iizuka and M. Haneishi, "A consideration on dual polarized array antenna composed of triplate-type tapered slot antenna elements," *Proc. IEICE Soci. Conf.*, B-106, Sep. 1996.
- [3-8] H. Iizuka and M. Haneishi, "A consideration on radiation properties of triplate-type tapered slot antenna," *Proc. IEICE Gen. Conf.*, B-59, Mar. 1996.
- [3-9] H. Iizuka and M. Haneishi, "Triplate-type tapered slot antenna and its radiation properties," *IEICE Tech. Rep.*, AP95-79, pp.23-26, Nov. 1995.
- [3-10] H. Iizuka and M. Haneishi, "A consideration on radiation properties of tapered slot array antenna," *Proc. IEICE Soci. Conf.*, B-41, Sep. 1995.
- [3-11] H. Iizuka and M. Haneishi, "Radiation properties of tapered slot antenna," *IEICE Tech. Rep.*, AP95-3, pp.15-20, Apr. 1995.
- [3-12] H. Iizuka and M. Haneishi, "A consideration on radiation properties of notch antenna fed by microstrip line," *Proc. IEICE Gen. Conf.*, B-97, Mar. 1995.